Summer 2008

Probing spin, charge and lattice coupling in manganites

Zhiqiang Chen
New Jersey Institute of Technology

ABSTRACT

PROBING SPIN, CHARGE AND LATTICE COUPLING IN MANGANITES

by
Zhiqiang Chen

Complex oxides such as the manganites exhibit an intimate coupling of the electron spin, charge and lattice degrees of freedom. The characteristic feature of these materials is the existence of a ground state topology with many closely lying minima. The system can be switched from one minimum to another by the application of external parameters such as strain, temperature, magnetic fields, or electrical fields. These materials thus exhibit large responses to these external parameters and can be used as novel sensors in data storage and other applications. Understanding the couplings will have an impact on the fundamental science of highly correlated materials as well as in applications to industry.

This work focuses on applying pressure to probe the properties of Colossal Magnetoresistance Manganites, self-doped La_XMnO_3 (X=0.85, 0.75) and chemically doped $La_{0.67}Ca_{0.33}MnO_3$. For all of them, obvious pressure effects on electronic transport and structure have been investigated; especially, critical pressures were found between ~3.4 GPa to ~4.0GPa. Below P*, pressures increase the metal-insulator transition temperature and electrical conductivity while both of them decrease with increasing pressures above P*. In particular, the bandwidth increase drives the increase of T_{MI} for pressures below P*. The reduction of T_{MI} at higher pressures is found to result from the Jahn-Teller distortions of the MnO_6 octahedra and the localization of 3d electrons. The general trend is expected to be a characteristic feature of Colossal Magnetoresistance manganites.

PROBING SPIN, CHARGE AND LATTICE COUPLING IN MANGANITES

by
Zhiqiang Chen

A Dissertation
Submitted to the Faculty of
New Jersey Institute of Technology
in Partial Fulfillment of the Requirements for the Degree of
Doctor of Philosophy in Materials Science and Engineering

Interdisciplinary Program in Materials Science and Engineering

August 2008

APPROVAL PAGE

PROBING SPIN, CHARGE AND LATTICE COUPLING IN MANGANITES

Zhiqiang Chen

Dr. Trevor A. Tyson, Dissertation Advisor — Date
Professor of Physics Department, NJIT
Director of Materials Science and Engineering Program

Dr. Nuggehalli M. Ravindra, Committee Member — Date
Professor of Physics Department, NJIT
Director of the Joint NJIT-Rutgers (Newark) Applied Physics Program

---

Dr. Ken Ahn, Committee Member — Date
Assistant Professor of Physics Department, NJIT

Dr. Tao Zhou, Committee Member — Date
Assistant Professor of Physics Department, NJIT

Dr. Mark Croft, Committee Member — Date
Professor of Department of Physics and Astronomy, Rutgers

BIOGRAPHICAL SKETCH

Author: Zhiqiang Chen

Degree: Doctor of Philosophy

Date: August 2008

Undergraduate and Graduate Education:

- Doctor of Philosophy in Materials Science and Engineering,
  New Jersey Institute of Technology, Newark, NJ, 2008
- Master of Science in Condensed Matter Physics,
  Nanjing University, Nanjing, Jiangsu, P. R. China, 2002
- Bachelor of Science in Materials Science and Engineering,
  Nanjing University, Nanjing, Jiangsu, P. R. China, 1999

Major: Materials Science and Engineering

Presentations and Publications:

Z. Chen, T. A. Tyson, K. H. Ahn, Z. Zhong and J. Hu,
"Origin of the Non-Linear Pressure Effects in Perovskite Manganites: Buckling of Mn-O-Mn Bonds and Jahn-Teller Distortion of the MnO_6 Octahedra Induced by Pressure", submitted to Applied Physics Letters, August 2008.

Z. Chen, T. A. Tyson, S. Kim and S.-W. Cheong,
"High Pressure Effects on the Crystal Structure of Hexagonal RMnO3", manuscript to be submitted (2008).

Z. Chen, T. A. Tyson, K. H. Ahn, Z. Zhong and J. Hu,
"High pressure studies of the structure and transport of La_xMnO_3", manuscript in preparation (2008).

T. A. Tyson, Z. Chen, Q. Jie, Q. Li and J. J. Tu,
"The Origin of Thermoelectricity in $Ca_3Co_4O_9$", submitted to Physical Review Letters (2007).

C. Cui, T. A. Tyson, Z. Chen, and Z. Zhong,
"Transport and structural study of pressure-induced magnetic states in $Nd_{0.55}Sr_{0.45}MnO_3$ and $Nd_{0.5}Sr_{0.5}MnO_3$", Physical Review B, 68, 214417, (2003).

Z. Chen, T. A. Tyson, K. H. Ahn, Z. Zhong and J. Hu,
"Origin of the Non-Linear Pressure Effects in Perovskite Manganites", American Physics Society Meeting, March 2008, New Orleans, FL. Presentation.

Z. Chen, T. A. Tyson S. Kim and S. -W. Cheong,
"Effect of Pressure on the Atomic and Electronic Structure of Hexagonal YMnO3", American Physics Society Meeting, March 2008, New Orleans, FL. Poster Session.

Z. Chen, T. A. Tyson, and Z. Zhong,
"High Pressure Effects on Structure and Transport of Self-doped Manganite $La_{0.85}MnO_3$", American Physics Society Meeting, March 2007, Denver, CO. Presentation.

Z. Chen, T. A. Tyson, and Z. Zhong,
"Structure and Transport Studies of $La_{0.9}MnO_3$ under Pressure", American Physics Society Meeting, March 2006, Baltimore, MD. Presentation.

Z. Chen, and T. A. Tyson,
"High Pressure Structure and Transport Studies of La_xMnO_3", American Physics Society Meeting, March 2005, Los Angeles, CA. Presentation.

To my beloved family

献给我最亲爱的家人，父母是我生命的源泉。
特别献给我的妻子，她的鼓励与支持给予我无限的动力。

ACKNOWLEDGMENT

I would like to express my deepest gratitude to Prof. Trevor A. Tyson, my academic advisor, not only for his extensive knowledge, insight, and intuition in the physics field, but also his financial support and his personal advice. Special thanks are given to Prof. Nuggehalli M. Ravindra, Prof. Mark Croft, Prof. Ken Ahn and Prof. Tao Zhou for actively participating in my committee.

The author appreciates the significant assistance from Dr. Jingzhu Hu, Dr. Zhong Zhong, Dr. John Kirkman, Dr. Zhenxian Liu and Dr. James Ablett at National Synchrotron Light Source (NSLS) for x-ray diffraction and x-ray absorption measurements; Prof. William A. Bassett at Cornell University for help in high-pressure XAFS measurements; Dr. Congwu Cui and Peng Gao, for assistance in high pressure techniques and sample preparations.

This research was funded by National Science Foundation Grant DMR-0512196.

The high pressure x-ray diffraction measurements were conducted at beamline X17B1 and X17C, NSLS, Brookhaven National Laboratory (BNL), which is funded by the U.S. Department of Energy.

My family deserves my greatest appreciation. My parents have always given me support no matter how far away they are. My parents-in-law have always supported me especially during their visits. Special thanks are given to my dear wife, Yuanrui. She is always the first audience for my presentations. Without her fully support, I could not have finished my research work. This dissertation is inspired by the everlasting love of my family.

TABLE OF CONTENTS

TABLE OF CONTENTS
(Continued)

Chapter **Page**

TABLE OF CONTENTS
(Continued)

Chapter **Page**

TABLE OF CONTENTS
(Continued)

Chapter **Page**

LIST OF TABLES

Table **Page**

LIST OF FIGURES

Figure **Page**

LIST OF FIGURES
(Continued)

Figure **Page**

LIST OF FIGURES
(Continued)

Figure **Page**

LIST OF FIGURES
(Continued)

Figure **Page**

LIST OF FIGURES
(Continued)

Figure **Page**

CHAPTER 1

FUNDAMENTAL OF COLOSSAL MAGNETORESISTANCE

1.1 History and Background

Magnetoresistance (MR) effect was first discovered by William Thomson in 1856 in magnetic metals such as iron and nickel, but he was unable to lower the resistance by more than 5%. This offset was named ordinary magnetoresistance (OMR). Two decades ago, a lager magnetoresistance effect (in the order of 10%) named giant magnetoresistance (GMR) was found in Fe/Cr multilayer by Albert Fert[1] *et al.* and Peter Grüberg[2] *et al.* independently, who were awarded the 2007 Noble Prize. This system had been exploited commercially in the hard disk technology and magnetic sensors. In 1950, another much higher magnetoresistance effect in $La_{1-x}Ca_xMnO_3$ and $La_{0.8}CaMnO_3$ had been investigated by Van Santen and Jonker[3]. In 1994, the discovery (Jin, Tiefel[4] *et al.*) of colossal magnetoresistance (CMR) effect in the mixed-valence manganite thin films attracted renewed attention due to the extremely high negative MR (even more than 100%). The growth of interest in its properties stems mainly from the prospect of creating mixed-valence manganite devices whose MR performance exceeds GMR devices.

The understanding and application of CMR offers tremendous opportunities for the development of new technologies such as read/write head for high capacity magnetic storages, spintronics and magnetic sensors. CMR materials, especially 3d transition-metal oxides, possess larger room-temperature magnetoresistivity associated with a metal-insulator transition in a narrow temperature range. Several commercial patents have

been made, such as magnetic random access memory[5] and magnetic sensor[6, 7]. In Figure 1.1, a magnetic random access memory (MRAM) device[8], which uses magnetism to store information without moving parts, has become available commercially from Freescale. The current-induced reorientation of the magnetization of a magnet results in a spin transfer toque, which is essential for the second generation of MRAM, such as magnetic semiconductor GaMnAs.

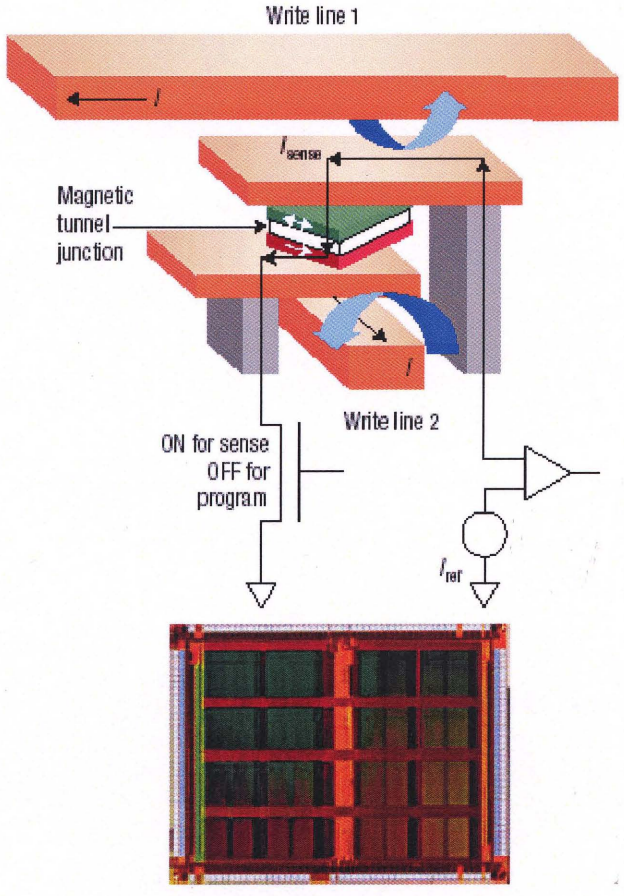

Figure 1.1 Schematic diagram of MRAM produced by Freescale[8].

The CMR effect is based on the manganite perovskites $T_{1-x}D_xMnO_3$, where T is a trivalent transition-metal cation (T = La, Pr, Nd, Sm, etc.) and D is a divalent alkaline-earth cation (D = Ca, Sr, Ba, etc.). The CMR manganites have been attracting intense interest

from both experimentalists and theoreticians, due to their diversities of physical phenomena, such as ferromagnetic (FM) to paramagnetic (PM), metal-insulator transition (MIT), charge ordering (CO), orbital ordering (OO), double exchange (DE), super exchange (SE), and Jahn-Teller distortion (JTD). In condensed matter physics, the origin of CMR effect in the perovskite structure is due to the competition of the interactions among charges, spins, and atomic correlations. The detailed studies of these interactions in this highly correlated system will also improve our understanding other complex oxides such as transition metal oxides and high Tc superconductors.

1.2 Concepts of Magnetoresistance

Magnetoresistance (MR) is a property of the material that leads to change in its electrical resistivity when an external magnetic field applied on it. It is generally defined as:

$$MR(T) = \frac{\rho(H,T) - \rho(0,T)}{\rho(0,T)} \times 100\% \qquad \textbf{(1.1)}$$

Where ρ(H, T) and ρ(0,T) are the resistivity with and without magnetic field at given temperature T. Early measurements (about one and an half centuries ago) yield MR values of ~5%.

Giant magnetoresistance (GMR) is a quantum mechanical effect, observed in thin films with alternating ferromagnetic and nonmagnetic layers. Two decades ago the GMR effect was discovered with MR in the order of 10%. It has been widely used in the read/write heads of hard disk drivers and magnetoresistance random access memory and other high density storage devices[9]. Generally, GMR was categorized into three subtypes: Multilayer GMR, Spin-valve GMR and Granular GMR.

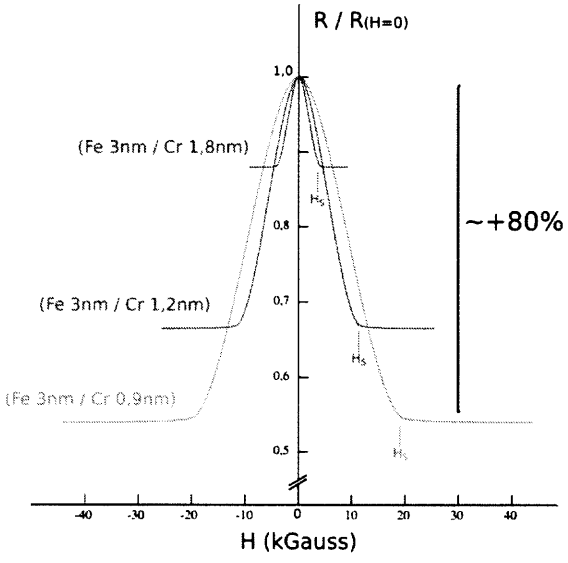

Figure 1.2 The magnetoresistance of Fe/Cr multilayer at 4.2K[1].

In Multilayer GMR, two or more ferromagnetic layers are separated by a very thin (~1nm) non-ferromagnetic spacer (e.g. Fe/Cr/Fe)[1]. At that thickness the RKKY coupling[10-13] between adjacent ferromagnetic layers becomes antiferromagnetic, which makes the magnetizations of the adjacent layers to align in anti-parallel. Even under low magnetic fields, the electrical transportation statue can transform from higher resistance with anti-parallel spins to lower level with parallel spins and the difference of resistance can reach more than 10% at room temperature (Figure 1.2). RKKY interaction is an indirect exchange coupling between nuclear spins via conduction electrons, originally proposed by Ruderman and Kittel *et al.* in 1954. Later this effect was used to explain the spin coupling of inner d or f shell in transition metal atoms by means of an interaction through conduction electrons.

In spin-valve GMR, two ferromagnetic layers are separated by a thin (~3nm) non-ferromagnetic spacer, but without RKKY coupling. The magnetization of two adjacent FM electrodes can be switched independently with different coercive fields.

Therefore, parallel and anti-parallel alignments correspond to the lower and higher resistance states normally. This device is also called a spin valve[14], which has been used commercially in hard drive technology.

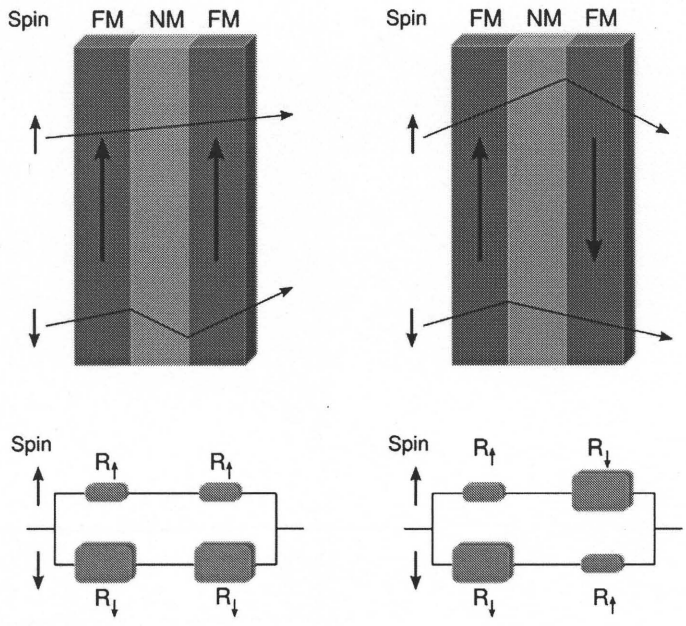

Figure 1.3 Spin-valve GMR.

Figure 1.3 shows the scheme of spin-valve GMR. $R_\uparrow$ and $R_\downarrow$ represent electrons resistance for spin-up and spin-down respectively. The size of green boxes presents the value of resistance, which means that an anti-parallel spin orientation between FM layers and electrons can result in more electron scattering and higher resistance. The magnetoresistance of spin-valve GMR can be defined as,

$$MR = \frac{R_H - R_0}{R_0} = -\frac{(R_\uparrow - R_\downarrow)^2}{(R_\uparrow + R_\downarrow)^2} \qquad \textbf{(1.2)}$$

In which, $R_H=2R_\uparrow R_\downarrow/(R_\uparrow + R_\downarrow)$ and $R_0=1/2(R_\uparrow + R_\downarrow)$ are resistance with and without external magnetic field.

Granular GMR is an effect that occurs in solid precipitates of a magnetic material in a non-magnetic matrix, but it has lower GMR ratios around 10%. In practice, granular GMR effects have been observed in several magnetic/non-magnetic alloys such as Cu/Co[15, 16] and Co_xAg_{1-x}[17].

CMR effects, in mostly manganese-based perovskite oxides, attracted the renewed interest due to its extremely high MR ratio of near 100% (Figure 1.4)[4]. This tremendously encourages experimentalists and theoreticians to understand the mechanisms involved. For this strongly correlated electron system, spins, charges, orbital and atomic couplings should play important roles simultaneously, where classical simplifications that neglect some interactions to study others separately are not valid.

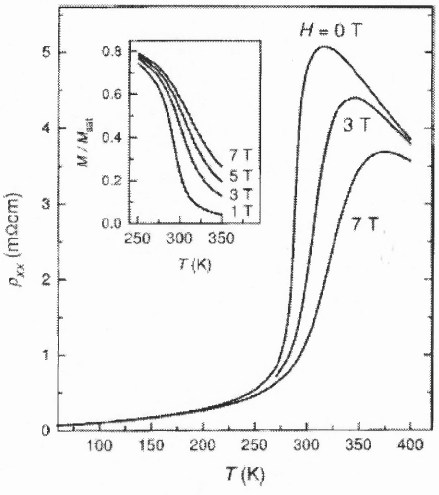

Figure 1.4 The temperature dependence of $\rho_{\chi\chi}(H, T)$ of $La_{2/3}(Pb,Ca)_{1/3}MnO_3$ single crystal at various fields H. The insert shows $M_H(T)$ in the transition region[18].

In this thesis we focus on high pressure effects of CMR polycrystalline materials, by experiments in the extreme conditions and interpretations with modern theories. More details about pressure effects on single crystals and thin films are on-going by our group and can also be found in other groups work.

1.3 Crystalline Structures of CMR Materials

The cubic-like CMR perovskite manganite $RE_{1-x}A_xMnO_3$ has a parent compound $REMnO_3$ (RE=La, Pr, Nd *et al.*), trivalent rare-earth ions, which can be substituted by the divalent alkaline-earth (A=Ca, Ba, Sr *et al.*) or even by a vacancy (self-dope manganites (e. g. La_xMnO_3)).

$LaMnO_3$ is a typical parent compound with an ideal cubic crystalline structure as the perovskite mineral $CaTiO_3$ (Figure 1.5). However, due to the size mismatch between La ions and Mn ions, the structure is distorted into orthorhombic, rhombohedra, or even monoclinic unit cells. A measurement of the mismatch from distorted cubic cell is given by the Goldschmidt[19] tolerance factor.

$$f = \frac{(< r_A > + r_O)}{\sqrt{2}(r_{Mn} + r_O)} \qquad \textbf{(1.3)}$$

Where $<r_A>$ is the average ion size at R-site occupant, r_{Mn} and r_O are the ion sizes for Mn and O. The sums of radius of neighboring ions correspond to the bond distances. The perovskite structure is stable for $0.89<t<1.02$, therefore f=1 is the perfect cubic closely packed structure.

Table 1.1 Structural Parameters of Stoichiometric Sample $LaMnO_3$ at Ambient Temperature and Pressure[20].

	x	y	z
La (4c)	-0.0078	0.049	0.25
Mn (4b)	0.5	0	0
O1 (4c)	0.0745	0.4874	0.25
O2 (8d)	0.7256	0.3066	0.0384

Table 1.1 gives the $LaMnO_3$ structure at room temperature with space group Pbnm, and lattice parameters are a=5.5367(1)Å, b=5.7413(1)Å, c=7.6929(2)Å; Mn-O1(m)=

1.9880(3)Å, O2-Mn(s)=1.907(1)Å, Mn-O2(l)=2.178(1)Å; Mn-O1-Mn=155.48(2)°, Mn-O2-Mn= 155.11(5)°.

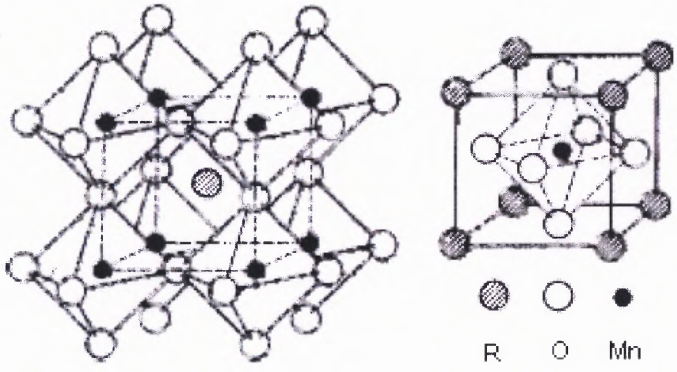

Figure 1.5 The ideal cubic perovskite structure of $RMnO_3$[21].

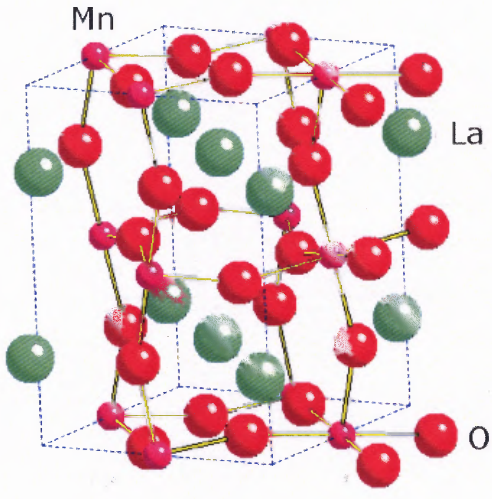

Figure 1.6 Distorted perovskite structure of undoped $LaMnO_3$ (figure drawn from the data of Table 1.1).

In Figure 1.6, the Jahn-Teller distortion of $LaMnO_3$ leads the tilt of MnO_6 octahedra with the bond angles of Mn-O-Mn decreasing from 180°. The space group is

Pbnm and its lattice parameters at room temperature are listed in the Table 1.1. More data at different temperatures about this stoichiometric $LaMnO_3$ have been published. And pressure effects on its crystalline structure were proposed by Loa *et al.*[22]. They observed that Jahn-Teller distortion may be completely suppressed above pressure ~18 GPa.

1.4 Chemical Doping Effects

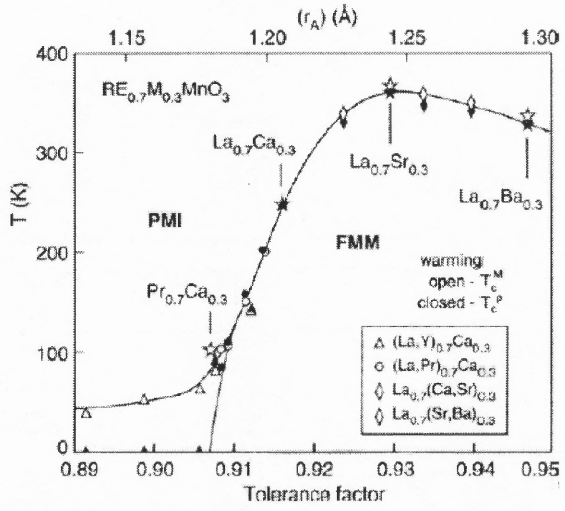

Figure 1.7 Phase diagram of temperature versus tolerance factor and average radius of A-site cations for the system $R_{0.7}A_{0.3}MnO_3$[23].

Chemical doping is one of primary method used to alter the physical properties and then optimize the CMR materials. In $R_{1-x}A_xMnO_3$ perovskite manganites, the trivalent cations substituted by the divalent cations not only change the ratio of Mn^{3+}/Mn^{4+} for carrier equilibrium but also alter the tolerance factor f. In equation (1.3), the different doping rates change the average R-site ion size $\langle r_R \rangle = r_R(1-x)+r_Ax$, which change both bond lengths and Mn-O-Mn bond angles, and result in the alterations of carrier bandwidth W. Compared with the external pressures, the chemical doping has similar effects on crystalline structures and electronic structures, so-called " internal pressure". In several perovskites,

the overlap between Mn 3d orbital and O 2p orbital can be strongly influenced by the internal pressures through changing the bond lengths and the Mn-O-Mn buckling.

Table 1.2 Ionic Radii for Ions in Perovskite Structure Oxide (nm)[24].

Ti^{4+}	0.0605	Y^{3+}	0.119	Ca^{2+}	0.134	Na^{+}	0.139
Mn^{4+}	0.053	La^{3+}	0.136	Sr^{2+}	0.144	K^{+}	0.164
Mn^{3+}	0.0645	Pr^{3+}	0.129	Cd^{2+}	0.131	Rb^{+}	0.172
Mn^{2+}	0.083	Nd^{3+}	0.127	Sn^{2+}	0.130		
Fe^{3+}	0.0645	Sm^{3+}	0.124	Ba^{2+}	0.161		
Co^{3+}	0.061, 0.0545 (ls)	Gd^{3+}	0.122	Pb^{2+}	0.149		
Ni^{3+}	0.069	Bi^{3+}	0.096				
Ga^{3+}	0.062						
Al^{3+}	0.0535						
						O^{2-}	0.140

The chemical doping effects have been studied by a great number of experimentalists, which exhibit the maximum ferromagnetic DE around x=1/3 and $\langle r_R \rangle$=1.24Å in Figure 1.7. The reduction of $\langle r_R \rangle$ from the optimum value results in the buckling of Mn-O-Mn from 180° and thus leads to an increasing distortion, which localizes the itinerant e_g electrons to reduce the conductivity. In the metallic state, a direct correlation between conductivity, ferromagnetism and Curie temperature was proposed by Zener[25]:

$$\sigma = \frac{xe^2}{ah}\frac{Tc}{T} \tag{1.4}$$

Where x is the doping rate, a is the Mn-Mn distance, compatible with the experimental results of Jonker[26] *et al.* in the doping range 0.2<x<0.4. The model should be extended to account for the high temperature insulating phase.

1.5 Electronic Structure

In ambient condition, an isolated transition metal ion has five degenerated orbital states. However, due to the combined effects of crystal field, exchange, and Jahn-Teller distortion, the splitting of the Mn (3d) bands of $LaMnO_3$ is modified as shown in Figure 1.8. The exchange splitting is about 3.0eV which moves the minority-spin bands above Fermi Energy E_f. In a crystal, the degeneracy is partly lifted by the crystal field into two subgroups: three t_{2g} orbits (d_{xy}, d_{zx}, d_{yz}) and two e_g orbits ($d_{x^2-y^2}$. $d_{3z^2-r^2}$), between which the maximum energy splitting is Δ~2.0eV. Because of the first Hund's rule, the spins of three t_{2g} electrons for Mn^{4+} are parallel with S=3/2 whereas e_g electron spin for Mn^{3+} is also parallel to t_{2g} in the state of $t_{2g}^{3\uparrow}e_g^{\uparrow}$ with S=2, corresponding to the magnetic moments $3\mu_B$ and $4\mu_B$ roughly.

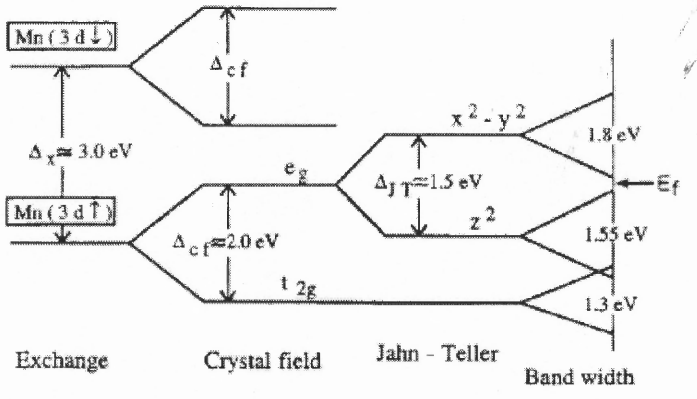

Figure 1.8 Energy levels of $LaMnO_3$[27].

In the lower symmetry structure, due to the strong Jahn-Teller distortions of MnO_6 octahedral the 2-fold e_g orbit splitting leads the single e_g electron of Mn^{3+} to occupy the lower energy level, therefore the Fermi level falls into the gap. At low temperature, the ground state of $LaMnO_3$ is A-type antiferromagnetic with Neel temperature ~120K.

In the perovskite manganites, several interactions with energies of the order of 1 eV come into play for their electronic properties[28]:

(1) d-d coulomb interaction U, by which a $d^{n+1}d^{n-1}$ charge excitation is created in an array of d^n ions;

(2) charge-transfer interaction Δ_{CT}, by which an oxygen 2p electron can be transferred to the neighboring Mn 3d orbital to create a p^5d^{n+1} charge excitation from $p6d^n$;

(3) p-d transfer integral t, which determines the 3d electron bandwidth W;

(4) Hund's rule magnetic coupling energy $J_H(=U_{ex}/2)$, U_{ex} is the on-site exchange interaction energy to flip a d-spin;

(5) The crystal-field energy splitting Δ_{cf} and Jahn-Teller energy splitting Δ_{JT};

(6) Intra-atomic exchange between adjacent 3d orbital.

The energies of these interactions are so delicate that the electronic structure can be easily modified by adjusting temperature, chemical doping, pressure and magnetic field and so on.

1.6 Physics of CMR

In perovskite manganites, a large change of resistance can be induced by an external magnetic field. This negative MR effect can be interpreted by applying the theories of double exchange, super exchange, charge ordering/ orbital ordering and Jahn-Teller distortion on the spin, charge, and orbital states, long range and local structure.

1.6.1 Double Exchange

The double exchange mechanism originally proposed by Zener[25] (1951) explains the strong correlation between ferromagnetism and electronic transportation. In the doped

manganese oxides, Zener points out a simultaneous jump of the e_g electron of Mn^{3+} to the O 2p orbital and from the O 2p orbital to the empty e_g orbital of Mn^{4+} in the configuration of $Mn^{3+}O^{2-}Mn^{4+}$. Due to strong Hund's coupling, the hoping integral has a finite value only when the spins of neighboring Mn^{3+} and Mn^{4+} are aligned ferromagnetically.

This theory was further developed by Anderson and Hasegawa[29] (1955). They treated the core spins of Mn ions classically but treated the mobile electrons quantum mechanically and found that Zener's energy level splitting was proportional to $\cos(\theta/2)$, where θ is the angle between the neighboring t_{2g} spins. Therefore, the possibility of the e_g electron hopping between the neighboring Mn sites is of the expression as:

$$t_{ij} = t_0 \cos(\theta_{ij}/2) \tag{1.5}$$

Where t_0 is the transfer integral determined by the Mn-O bond distances and Mn-O-Mn bond angles which influence the overlap of Mn 3d orbital and O 2p orbital, θ_{ij} shows the classical angles between the t_{2g} core spins, and subscripts i and j represent the neighboring Mn sites. For $\theta_{ij}=0$, the core spins being parallel maximizes the hopping rate and minimizes the electronic resistance and vice versa for $\theta_{ij}=\pi$.

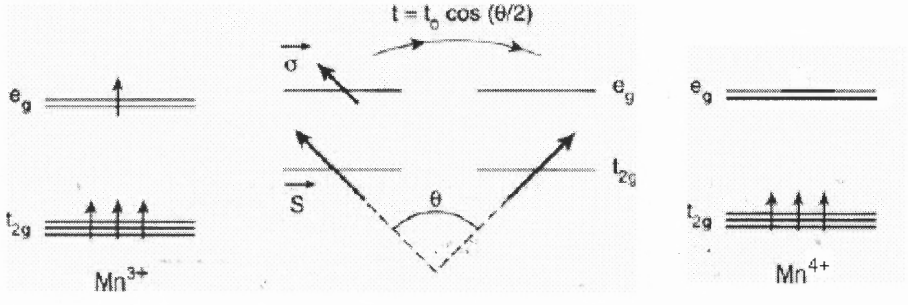

Figure 1.9 Schematic for Double Exchange (DE) mechanism.

The double exchange mechanism can qualitatively describe the negative magnetoresistance. By applying an external magnetic field, the Mn core spins are aligned ferromagnetically, hence the increasing of hopping rate results in a low resistance state. Further, Millis *et al.* proposed[30] that double exchange alone does not explain the resistance of perovskite manganites and electron-phonon interactions induced by Jahn-Teller distortions of MnO_6 octahedra should be involved for quantitative consideration.

1.6.2 Superexchange

Superexchange is defined as the interactions taking place between the neighboring magnetic cations such as transition-metal ions which are well separated by the diamagnetic anions such as O^{2-}. The superexchange between Mn-Mn cations has several different magnetic configurations, which are described by the following[29, 31, 32]:

(a) When two filled e_g orbitals overlap well with an anion, both Mn-O bonds can be covalent. The Mn-Mn bond distance is smallest and the cations coupling is strongly antiferromagnetic below Curie temperature (Ordinary superexchange between $e_g(\sigma)$).

(b) When a filled e_g orbital and an empty one overlap an anion with each site, only one Mn-O bond can be covalent and another can be ionic. The Mn-Mn separation is large and the cation coupling becomes ferromagnetic (direct exchange between e_g orbital and t_{2g} shell).

(c) When two e_g orbitals overlap an anion, neither Mn-O bond can be covalent and both of them are ionic. The Mn-Mn bond distance becomes the largest and the coupling is a weaker antiferromagnetism (π-bond superexchange of t_{2g} shell).

(d) The two states of Mn^{3+}-O-Mn^{4+} and Mn^{4+}-O-Mn^{3+} are degenerate below the Curie temperature, so the electron can jump freely through O^{2-} anion to form a metallic-like bond. In the case of anion separating ferromagnetically coupled Mn^{3+} and Mn^{4+} in a disordered lattice system can be explained by double exchange model, which is different with the first three in the order lattice conditions. It is noted that double exchange phenomenon corresponds the low resistivity while the other three exchange situations have high resistivity even if there is ferromagnetic coupling in case (b).

In crystal field theory, Anderson worked out the superexchange effect, by using the expression[29]:

$$J_{eff} = 2\frac{b^2}{U} \tag{1.6}$$

Where b is the transfer integral and U is the Coulomb repulsive energy relating to the local structure. The superexchange J_{eff} depends on the charge transfer bandwidth W, which strongly correlates with the Mn-O-Mn bond angles and Mn-Mn bonds. The strong e_g-electron coupling to the oxygen displacements introduces σ type ferromagnetic coupling in Mn^{3+}-O^{2-}-Mn^{4+} via superexchange or a fast Mn^{3+} to Mn^{4+} electron transfer via a strong double exchange. When the bandwidth W is increased to form a small polaron that traps a carrier at a single cation site, a transition of electron state occurs from localized to itinerant, which means a transition of the ferromagnetic coupling from superexchange to double exchange. However, due to different mechanism the superexchange varies as $\cos(\theta_{ij})$ whereas the double exchange as $\cos(\theta_{ij}/2)$.

1.6.3 Charge Order

Charge order, also called as Wigner crystallization, results from the interatomic Coulomb interactions[21, 32, 33]. It shows the ordering of Mn^{3+}/Mn^{4+} in the crystal lattices, which can be seen as a superlattice modulation to the fundamental Bragg reflections in the electron diffraction.

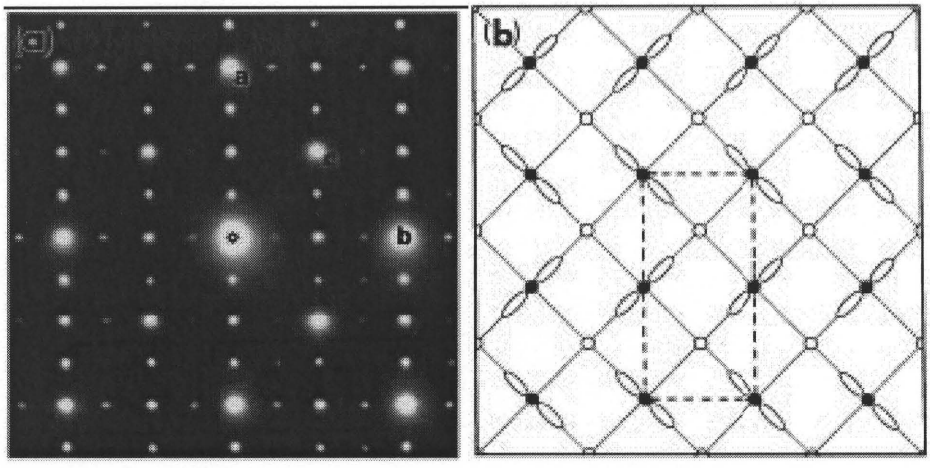

Figure 1.10 Charge Ordered state of $La_{0.5}Ca_{0.5}MnO_3$ (a) [001] zone-axis electron diffraction pattern obtained at 95 K. The fundamental Bragg peaks labeled *a, b,* and *c* can be indexed as (200), (020), and (110), respectively. The presence of superlattice spots with modulation wave vector (1/2, 0, 0) or (0, 1/2, 0) is evident. Kinematically forbidden (100) and (010) spots also appear as a result of multiple scattering. (b) Schematic charge-ordering picture of Mn^{4+} and Mn^{3+} ions. Open and closed circles represent Mn^{4+} and Mn^{3+} ions, respectively. The orientation order of d_{z2} orbitals of Mn^{3+} ions which results in the cell doubling along the *a* axis is also indicated[34].

Charge order can be explained as the competition between long-range Coulomb interactions and carrier bandwidth. The mobile d electrons can be trapped and then localized on certain Mn sites to form a regular sublattice when the coulomb interaction between atoms is comparable with the conduction-electron bandwidth W. The charge ordered state appears most likely at the low temperature at rational doping levels, especially x=1/8, 1/2, or 3/4. Intermediate doping yields mixed patterns. This effect always happens with the narrow bandwidth manganites, in which the bandwidth can be more

easily adjusted by the lattice structure. The lattice distortion can be modified by changing the average A-site ion size $<r_A>$. And it is found that in the small $< r_A >$ compounds T_{CO} decreases monotonically with the increasing of $< r_A >$[35]. Also for half-doped manganite $La_{0.5}Ca_{0.5}MnO_3$, the degree of canting in the AFM state increases with the applied field which is eventually driven to an FM state in a large field (H)[36, 37]. So the local structure distortions can be controlled by the chemical doping, applying magnetic fields or pressures. The magnetic fields can align the spin direction to improve the electron mobility. The pressures can suppress the local structure distortion in the low pressure range. However, in our work we find that the higher pressures can impose Jahn-Teller distortion for some CMR manganites.

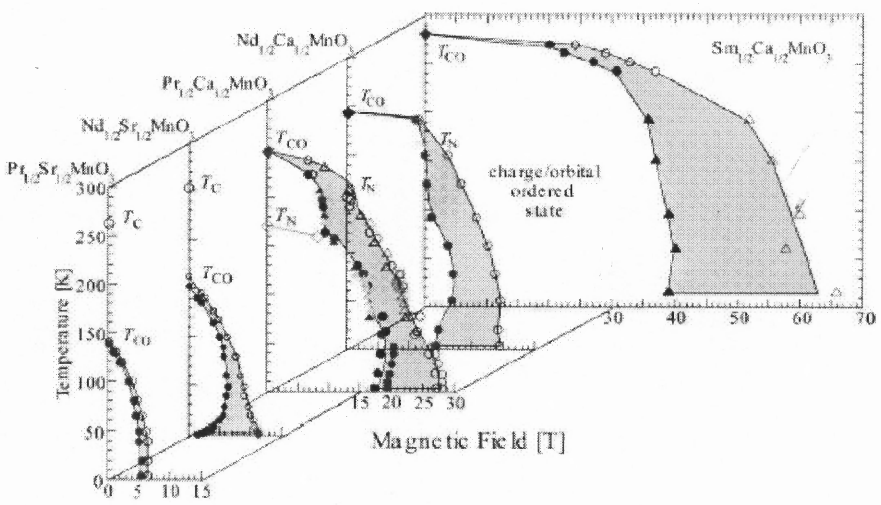

Figure 1.11 The charge/orbital-ordered phase diagraph with the various $<r_A>$ in $RE_{1/2}AE_{1/2}MnO_3$ system[38].

1.6.4 Orbital Order

For an octahedral-site Mn^{3+} ion, the single e_g electron can be in the degenerated orbital $d_{z^2-x^2}$ and $d_{z^2-y^2}$. The orbital state alternates between neighboring Mn^{3+} cations; the

relative orientation of the spin and orbital order are shown in Figure 1.12. The orbital order can be linearly combined by the form $d_{z^2-x^2}$ and $d_{z^2-y^2}$ with lobes along Mn-O-Mn directions.

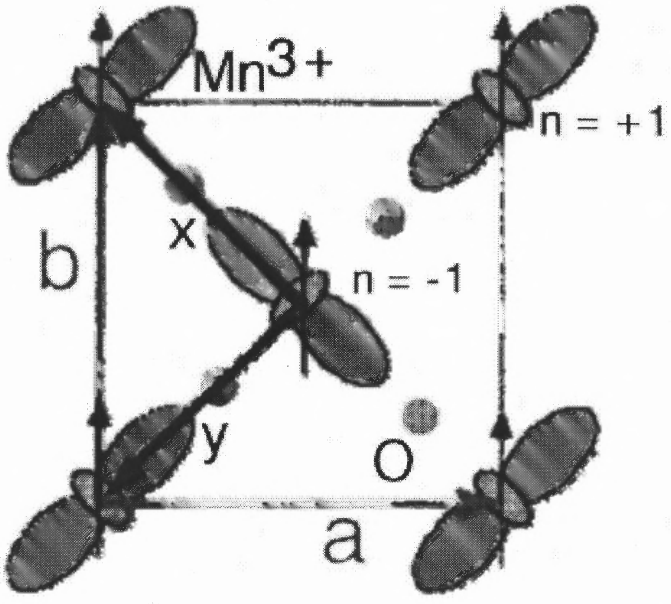

Figure 1.12 Schematic view of the orbital and spin ordering in the a-b plane of the perovskite manganite $LaMnO_3$, which shows the Orbital G spin A state[39].

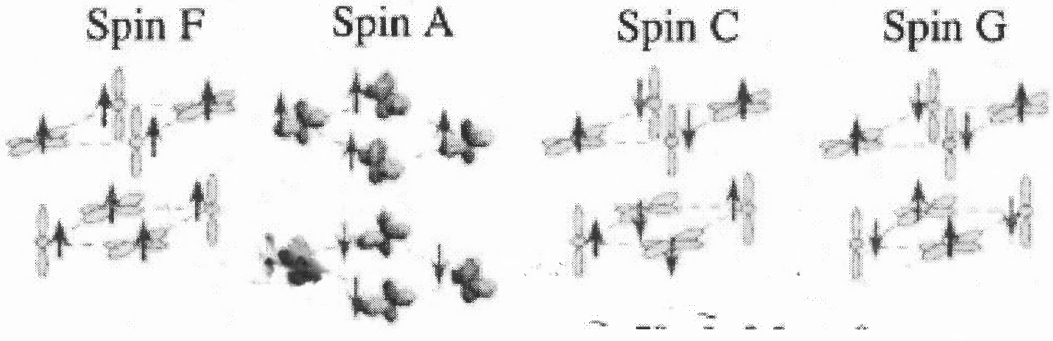

Figure 1.13 Optimized orbital structure for ferromagnetic (FM) and antiferromagnetic (AF) spin orders[40].

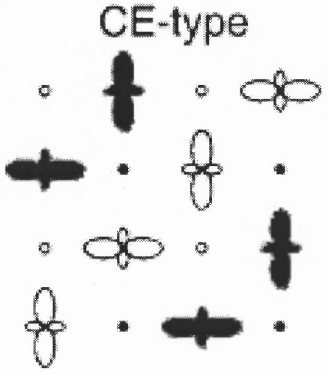

Figure 1.14 Schematic representations of spin, charge and orbital ordering for CE-type AFM structure. Solid and open symbols indicate up and down t_{2g} spins, respectively. The lobes indicate $(3x^2-r^2)$ or $(3y^2-r^2)$ orbitals and the change of its size symbolically indicates the spatial modulation of orbital density[41].

For perovskite manganites, the orbital order is always coupled with spin orders shown in Figure 1.13. Also the orbital order is coupled with the charge order and lattice distortion, e.g. the Jahn-Teller distortion (JDT) may lower the electron energy to induce CO and OO. Goodenough[21] proposed that in the perovskite $LaMnO_3$, the cooperative JDT of MnO_6 octahedra below T_{JT} can minimize the elastic energy by ordering the occupied e_g orbitals within *ab* plane at long range. Especially, when n=0.5, CE-type AFM structures are widely observed in manganites such as $La_{0.5}Ca_{0.5}MnO_3$ and $Nd_{0.5}Sr_{0.5}MnO_3$, as shown in Figure 1.14.

1.6.5 Electron-Lattice Coupling

Two sorts of electron coupling have been broadly studied in pervoskite manganites.

As defined in Equation 1.3, the tolerance factor t is an important indicator of the structure distortion. When t is small, a typical O-type structure with $a < c/\sqrt{2} < b$ can be obtained by the cooperative rotation of MnO_6 octahedral about a 110 axis. Whereas due to different <A>, $RMnO_3$ (R=La-Dy) has a different, O' type, orthorhombic structure where

$c/\sqrt{2} < a < b$. There are two more orthorhombic structures: $O^{\ddagger}$-type when $a \approx b < c/\sqrt{2}$ and a quasi-cubic structure O*-type when $a \approx c/\sqrt{2}$.

When t is not equal to one, the idea cubic structure is distorted by the size mismatch between A-site atoms and Mn ions in manganites $RE_{1-x}A_xMnO_3$. Therefore this internal stress is applied on the Mn-O-Mn bonds to produce a buckling along the bonds and the effective Mn-Mn hoping integral is sensitive to this buckling, decreasing rapidly as the buckling increases.

Another electron-lattice coupling is the conventional coupling due to the displacements of atoms from their idea crystallographic positions, which is called a structural Jahn-Teller distortion. The distortion of highly symmetric molecule can reduce its symmetry and lower its energy. In 1936, Jahn and Teller[42] firstly proposed that stability and degeneracy cannot exist simultaneously unless the molecular is linear. All orbital degenerate electronic states of non-linear molecules are unstable no matter the degeneracy is caused by spin or orbital, except that the twofold spin degeneracy contains an odd number of electrons. In the nonlinear molecules, the degeneracy of electronic states can be removed by this effect. The Jahn-Teller effect is most encountered in octahedral complexes of transition metals, such as Cu and Mn.

In perovskite manganites, by the octahedral crystal field the fivefold 3d orbital are split into two subgroups: t_{2g} and e_g with 3-fold and 2-fold orbital degeneracy respectively. The t_{2g} orbital have lower energy than e_g orbital because three t_{2g} orbital points along the bond axis while e_g orbital point to the interstice between bond axes. Further, Jahn-teller distortion destroys the degeneracy of the subgroups and the electronic structure becomes more complex.

Jahn-Teller distortions lead to three distinct pairs of Mn-O bonds: long (l), medium (m), and short (s) bonds in the MnO_6 octahedral, which includes two normal modes: Q2 mode, in which two of in-plane bonds contract while the other two bonds elongate; Q3 mode, in which the four in-plane Mn-O bonds contract while the two apical Mn-O bonds elongate. And there is also another Q1 mode with the simultaneous contraction or elongation of all six Mn-O bonds.

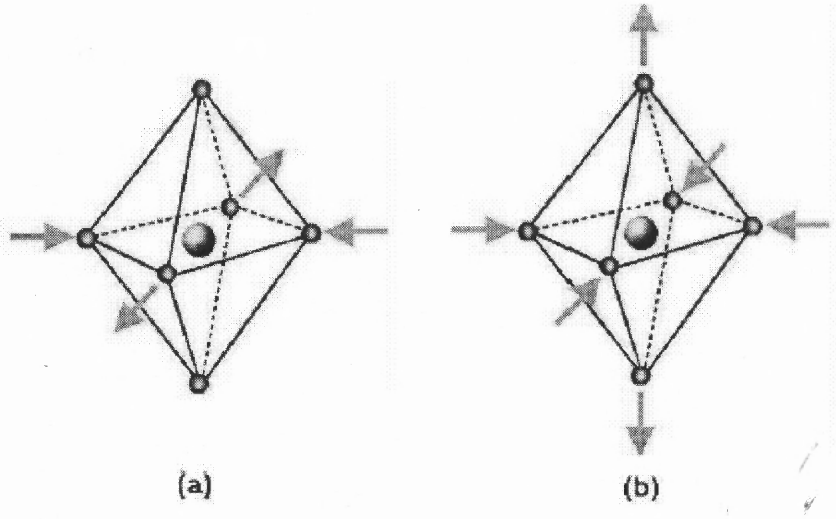

Figure 1.15 Jahn-Teller distortion of MnO_6 octahedral: (a) Q2 mode; and (b) Q3 mode.

Jahn-teller effect is an electron-lattice coupling, also named dynamical electron-phonon coupling, which is independent with spins. This strong electron-phonon coupling may trap the itinerant electrons into the orbital due to the local structure distortions producing a minimum potential. When this coupling is strong enough, the itinerant e_g electrons can be self-trapped to form a Jahn-Teller polaron in MnO_6 octahedral. As proposed by Millis[30] *et al.*, the Colossal Magnetoresistance (CMR) phenomenon can not only be explained qualitatively by electron-spin coupling, such as Double-Exchange and Superexchange. The other mechanisms like Orbital / Charge Order (OO/CO), and the

strong electron-lattice coupling (JTD) should also be involved in this complex system of perovskite Manganites.

CHAPTER 2

PHYSICS OF PRESSURE EFFECTS ON MANGANITES

2.1 Introduction

Pressure is a fundamental thermodynamic variable, which affects the electron transport and magnetic properties by modifying the long range symmetry (e. g. phase transition) and local atomic structure (such as static/dynamic JT distortion). Applying pressure (P) or magnetic field (H), or modifying chemical doping (x) can produce qualitatively similar effects. All of them can work together to maintain or modify the balance of the interactions among spins, charges, orbital, and atomic coupling.

2.2 On Structural Distortion

High pressure affects CMR manganite structure, including long range order (crystal structure transition) and short range order (local atomic structure distortion).

Several manganites have been investigated to exhibit a structural phase transition under pressure. In lightly doped $La_{1-x}Sr_xMnO_3$ compounds, the structure transforms from rhombohedra phase to orthorhombic phase at transition temperature T_s. Moritomo[43] *et al.* observed that the phase transition temperature T_s for x=0.17 presented a sudden jump around ~50K accompanying with a slightly pressure change from ambient to 0.1 GPa and with the applied pressure increasing, the rhombohedra phase extended to lower temperature range, shown in Figure 2.1.

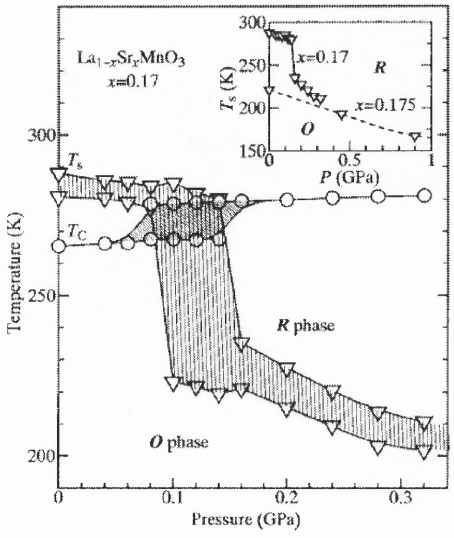

Figure 2.1 Pressure-temperature phase diagram for $La_{0.83}Sr_{0.17}MnO_3$[43].

Recently a half-doped manganite $La_{0.5}Ca_{0.5}MnO_3$ was shown to exhibit a pressure-induced phase transition from rhombohedrally distorted perovskite structure (space group Pnma) to monoclinic symmetry ($P2_1/m$) at ~15 GPa and room temperature in Figure 2.2.

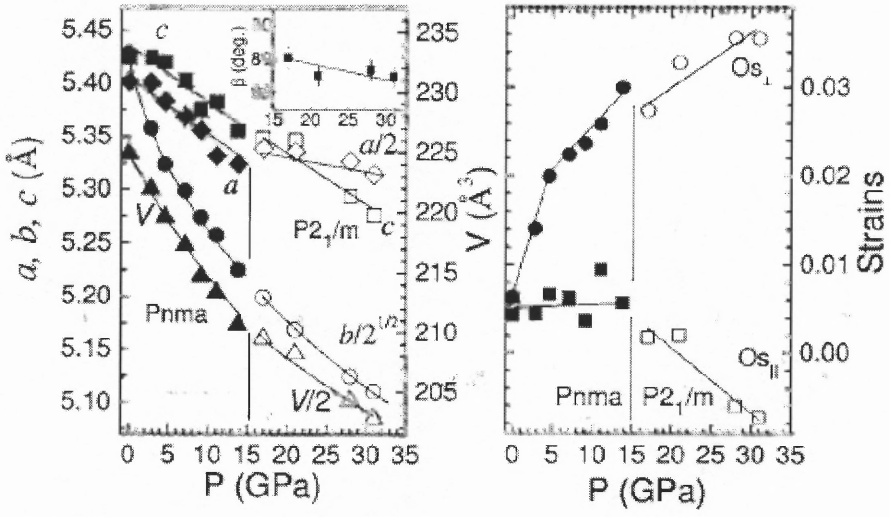

Figure 2.2 Pressure dependence of lattice parameters, unit-cell volume, and orthorhombic strain in $La_{0.5}Ca_{0.5}MnO_3$[44].

Pressure effects on local atomic structure have been intensively investigated. Under pressures, the unit cell can be compressed anisotropically due to the different compressibility of *a, b* and *c* parameters. Especially, the oxygen anion positions are sensitive to the applied pressures, which results in the octahedral distortion of perovskite manganites. Both Mn-O-Mn bond angles and Mn-O bond lengths may be changed significantly. Because of the anisotropic compression ratio of the three Mn-O bonds in octahedral, the Jahn-Teller type distortions can be enhanced or suppressed with increasing pressures. Therefore pressure affects the bandwidth by modifying the overlap of Mn^{3+} e_g orbital and O^{2-} 2p orbital. In undoped $LaMnO_3$, Lao[22] reported a continuous reduction of Jahn-Teller distortion with increasing pressure. Above ~18 GPa, the higher pressures completely suppress the distortions. Whereas, Meneghini[45] *et al.* showed that the Jahn-Teller distortion of $La_{3/4}Ca_{1/4}MnO_3$ abruptly jumped up at ~7GPa.

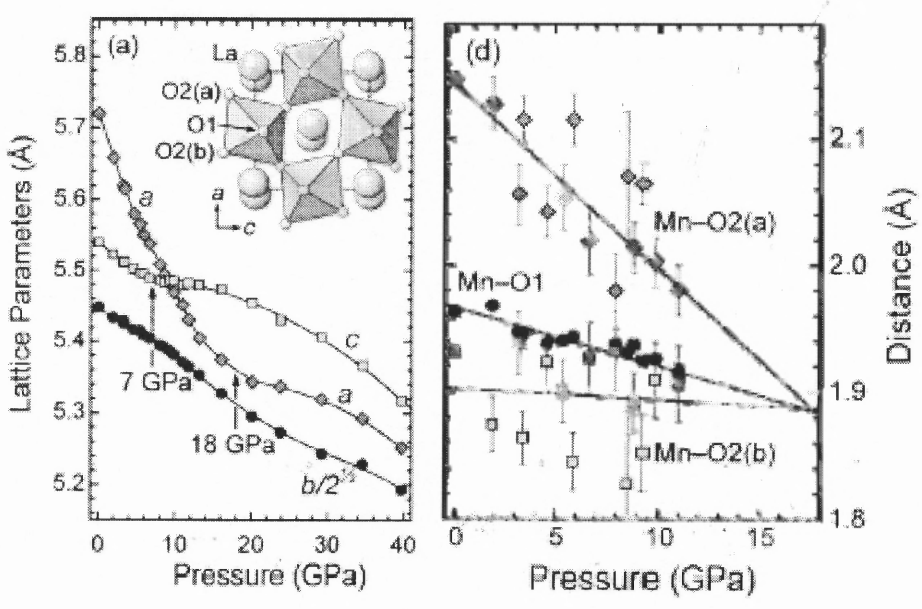

Figure 2.3 Pressure dependence of lattice parameters (a) and Mn-O bond distances in the perovskite octahedral (b) for $LaMnO_3$.

2.3 Equation of State

High pressure x-ray diffraction experiments provide measurements of the variation of unit-cell parameters for solid state samples and therefore the pressure dependence of unit-cell volume can be described by the equation of state (EoS) like gas or liquid state. In perovskite manganites, the first-order Murnaghan EoS (Murnaghan 1937) is typically used as below:

$$P(V) = \frac{B_0}{B_0'}\left(\left(\frac{V_0}{V}\right)^{B_0'} - 1\right) \qquad \textbf{(2.1)}$$

Where V and V_0 are the unit-cell volume under pressure P and at ambient pressure respectively; B_0 and B_0' are corresponding to the ambient pressure bulk modulus and its first-order derivative, defined as $B_0 = -V_0(\partial P / \partial V)_{p=0}$ and $B_0' = (\partial B / \partial P)_{p=0}$ separately.

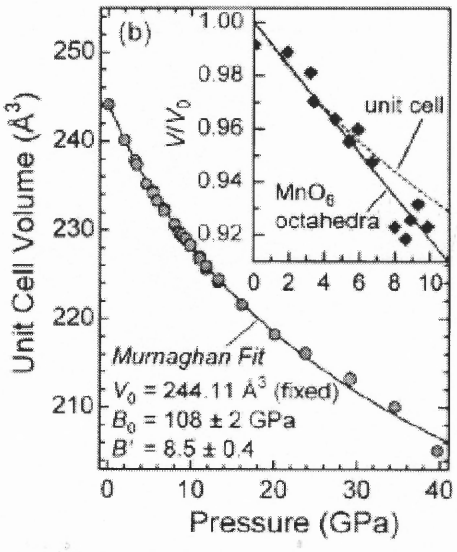

Figure 2.4 Pressure dependence of unit-cell volumes and its Murnaghan fitting for $LaMnO_3$ up to ~40 GPa[22].

In Figure 2.4, the first-order Murnaghan EoS fitting presents the bulk modulus B_0=108±2GPa and its derivative B_0'=8.5±0.4for undoped $LaMnO_3$. For other manganites,

similar results have been acquired. For example, Meneghini[45] *et al.* obtained B_0=178GPa and B_0'=4 for $La_{3/4}Ca_{1/4}MnO_3$.

2.4 On Bandwidth and Activation Energy E_g

In the framework of double-exchange model, the magnetic and transport properties are determined by the charge carrier bandwidth W, which depends on the Mn-O bond distance d and the octahedral tilt angle through the overlap integral between 3d orbitals of Mn^{3+} and Mn^{4+} via 2p orbital of O^{2-}. The detailed structural dependence of the bandwidth has been studied by Goodenough *at el.*[21]. Like chemical doping and magnetic field, pressure can be one of the most essential paths to modify the electronic carrier bandwidth by compressing Mn-O bond distances and changing the buckling of Mn-O-Mn. With the tight-binding approximation, the bandwidth W can be described by the empirical expression[21, 46, 47],

$$W = \cos\omega / d_{Mn-O}^{3.5} \qquad \textbf{(2.2)}$$

Where d_{Mn-O} represents the distance between the Mn cation site and the nearest O site in octahedral, in which six bonds are usually separated into long (l), middle (m) and short (s) bonds. As shown in Figure 2.5, ω means the average tilting angle between the neighboring octahedral and its relationship with Mn-O-Mn bond angles is:

$$\omega = \frac{1}{2}(\pi - < \theta_{Mn-O-Mn} >) \qquad \textbf{(2.3)}$$

In the low pressure range below ~2 GPa, the pressure dependence of bandwidth has a similar trend with chemical doping. Pressures compress Mn-O bond distances and increase Mn-O-Mn bond angles simultaneously, both of which may work together to increase the bandwidth for manganites, such as $La_{1-x}Ca_xMnO_3$ ($0.2<x<0.5$)[48, 49]. Pressure can suppress the charge order, enhance the carrier mobility and induce the FMM state.

Therefore, both metal-insulator transition temperature T_{MI} and Curie temperature T_C may shift to higher temperatures.

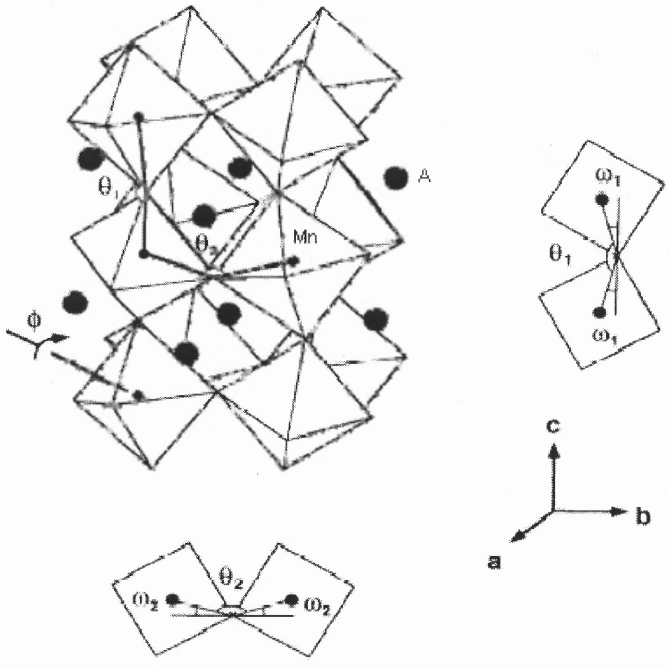

Figure 2.5 Schematic of distorted Pbnm perovskite structure with the definitions of tilting angle ω and bond angle θ.

However, for the study of manganites under higher pressures (beyond ~2GPa), the pressure dependence of bandwidth becomes more complex due to the different trends of bond distances, bond angles and pressure-induced/suppressed Jahn-Teller distortions.

Because of different pressure dependence of bandwidth and lattice distortions, the perovskite manganites can reach a saturated metal-insulator transition temperature T_{MI} at a critical pressure P*, which means that the sample presents more metallic state and T_{MI} increase below P*; while above P* the sample becomes insulating and T_{MI} decreases with increasing pressure. This phenomenon have been observed for a series of manganites such as $Nd_{1-x}Sr_xMnO_3$ (x=0.45, 0.50), $La_{0.60}Y_{0.07}Ca_{0.33}MnO_3$, and $Pr_{1-x}CaMnO_3$ (x=0.25, 0.30, 0.35) by Cui and Tyson[50-53] *et al.* in Figure 2.6.

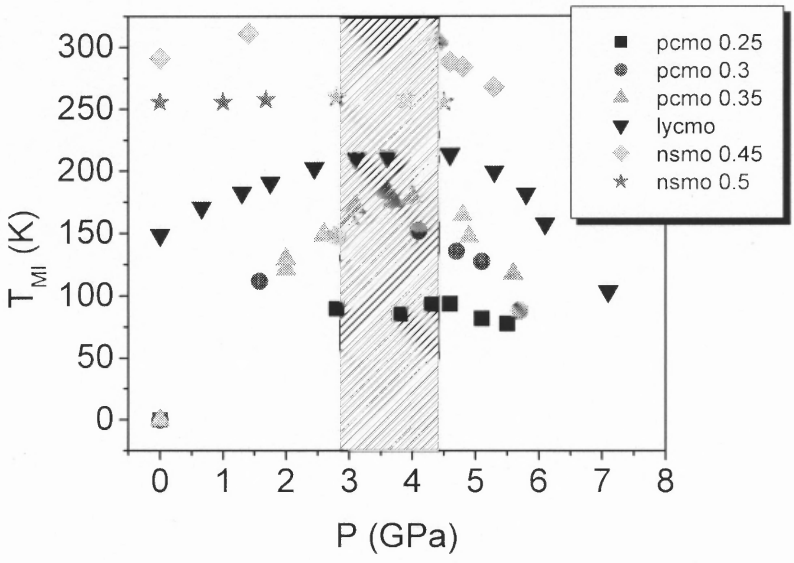

Figure 2.6 Pressure dependence of Metal-Insulator Transition (MIT) temperatures of $Nd_{1-x}Sr_xMnO_3$ (x=0.45, 0.50), $La_{0.60}Y_{0.07}Ca_{0.33}MnO_3$, and $Pr_{1-x}CaMnO_3$ (x=0.25, 0.30, 0.35).

2.5 Compared with Chemical Doping and Magnetic Field

Pressure (below ~ 2GPa), magnetic field and chemical doping produce qualitatively similar effects to stabilize the ferromagnetic metallic state. However, the mechanisms by which the electron mobility can be modified have significant difference: in the DE model the magnetic field aligns the t_{2g} spins of the neighboring Mn Site to reduce the scattering of itinerant e_g electrons by the localized core spin and thus enhance the carrier bandwidth.

Compared with the external applied pressure, the chemical doping is called "internal pressure". In the low pressure range, Hwang[54] *et al.* found that the applied pressure presents consistent effects on bandwidth enhancement as the modification of $\langle r_A \rangle$ with a conversion factor ~3.75×10^{-3} Å/GPa. In chemical doping method, the doping components and doping rate directly modify the average A site cation size $\langle r_A \rangle$ and

tolerance factor t, thus affect the bandwidth. The mismatch of $\langle r_A \rangle$ can affect the Mn-O-Mn bond angle without reducing significantly the equilibrant Mn-O bond length while hydrostatic pressure may directly compress Mn-O bonds.

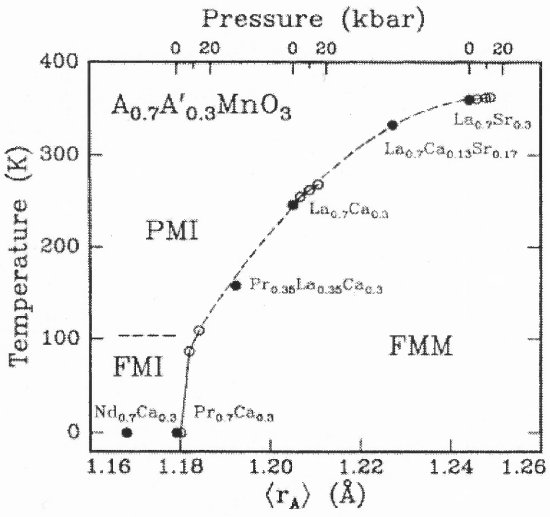

Figure 2.7 The phase diagram of $A_{0.7}A'_{0.3}MnO_3$.

As we can see, pressure affects the bandwidth directly by modifying the Mn-O bond distance and Mn-O-Mn bond angle distributions without introducing any chemical impurities.

CHAPTER 3

HIGH PRESSURE EXPERIMENTS AND TECHNIQUES

3.1 Introduction

In the study of materials properties, the high-pressure technique is attracting the scientists and engineers like other controlled variables such as temperature, electrical and magnetic field, and chemical doping[18, 54, 55]. In the research of CMR manganites, pressure affects the material properties significantly through changing the atomic structure by moving the atoms closer or by adjusting the bond angles. Therefore, the electronic structure shows some obvious difference with the ambient pressure, such as the appearance of insulator to metal transition, or even to superconductivity at high pressure conditions.

3.2 History of High Pressure Techniques

Most early work used the quenching technique to produce the high-pressure phase at ambient pressures. Until the Bridge era came (between 1910 and 1950), both the piston-cylinder device and Bridgman anvil were invented and developed by Bridgman for resistance and compressibility measurements up to ~ 10 GPa[56]. In the late fifties and early sixties, the piston-cylinder device was further improved for studies up to 15GPa[57, 58], but it was limited by the compressive strength of the sintered tungsten carbide. And then Drickamer and co-worker used their own designed anvil device to reach higher pressure around tens of GPa. Their high-pressure work had been extended to x-ray diffraction[59], Mössbauer[60], and optical[61] absorption measurement in solid-state physics.

In the mid 1960s, the use of diamond anvil cell made it possible for high-pressure studies in non-specialized laboratories. As its remarkable properties not only with extreme hardness but also high thermal conductivity and high transparency in a wide range of electro-magnetic radiation spectrum, the diamond anvil cell can be used as an ideal tool for high-pressure research, which has been applied in a number of experimental studies: optical absorption, reflectivity, Brillouin scattering (Whitfield[62] *et al.* 1976), Raman scattering (Sharma[63] 1977, Sherman[64] 1984), electron and nuclear resonance spectroscopy (Lee[65] *et al.* 1987), x-ray diffraction and absorption[66, 67].

With the efforts of nearly a century, the artificial high pressure in the laboratory can go up to ~560GPa, higher than the estimated pressure about 360GPa[68] at the center of the Earth.

3.3 Principle of Operation and Design for DAC

3.3.1 Diamond Anvil

Diamond is the premier anvil material because of its mechanical properties and transparency to photons over a relatively wide spectrum range (infrared, visible, ultraviolet to hard x-rays with the energy from 5eV to 10keV). Moreover, the extraordinary thermal conductivity, low thermal expansion and insulating properties of diamond strongly enhanced the ability to be broadly used in high pressure physical and chemical characterization.

Diamonds are classified as Type-I and Type-II. Standard diamonds (Type-I) are lightly yellow with nitrogen impurities. Type-II diamonds are white, which do not have absorption bands in the infrared and ultra-violet regions, but they are relatively expensive.

As usually Type-I diamonds are used in most of high-pressure experiments and moreover the nitrogen impurities enhance the resistance to plastic deformation, which results in the usage of Type-I diamonds in the Mbar pressure level.

Typical diamonds in high-pressure experiments are 1/3 carat (1 carat = 200 milligrams), usually with a culet size (d) from 300μm to 1000μm, a table diameter (D) ~3 mm and the thickness (t) around 1.5 mm, shown as Figure 3.1.

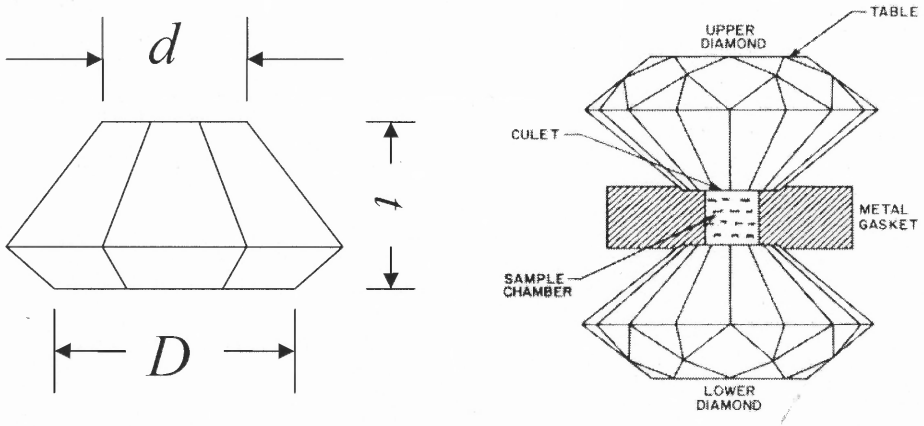

Figure 3.1 Designs of diamond anvil cell (a) Schematic graph of diamond anvil, (b) Basic configuration of DAC.

However, the applying pressure limit is determined by the anvil dimension (culet size d), which can be optimized for different pressure purposes. From previous experiences, the culet diameter of 750μm can reach 10 GPa. For pressure up to ~40 GPa, 400μm culet diamonds can be used. When the table-to-culet ratio increases to 100, 140 GPa can be achieved. The limitation of the applying pressure is roughly defined by the following empirical formula[69, 70]:

$$P_{mas}(GPa) = \frac{12.5}{(d(mm))^2} \qquad \textbf{(3.1)}$$

The maximum pressure applied in experiments should be lower than this, approximately $0.8P_{max}$.

Furthermore, the culet shape may play an important role, especially in the electrical measurement. The beveled culet edge can protect the connection wires though the gasket by reducing breakage. In addition, beveled culets may have smaller size to increase the pressure limitation to Mbar region (100 GPa).

3.3.2 Backing Plates

The diamond anvils must be mounted on a strong material which also allows access for the incident and diffraction beams. Due to its transparency to x-rays, beryllium (Be) has been chosen in the original Merril-Bassett cell in 1974. However, the beryllium has several disadvantages to limit its broader use in some conditions. First of all, Be is an extremely toxic metal and can only be machined by the licensed machine shops with relative high cost. Another problem is that the mechanical properties of beryllium can be significantly reduced by heating and cooling processes.

Therefore, as supplements, several other plate materials have also been widely used. Although it has higher level of x-ray absorption, tungsten-carbide maintains its mechanical strength over a wide range of temperatures. A further choice is to use boron or boron-carbide, which are both strong and have low x-ray absorption cross-section; but with the lower tensile strength, drilling optics holes can lead the supporting disc failure. In 2000, Miletich[71] *et al.* introduced diamond plates, which do not have a textured background in x-ray beams except occasional single crystal diffraction. Moreover, for other research purposes, several other materials have been involved. As a non-magnetic alloy, Be-Cu has

been used in high pressure magnetic experiments. Inconel 718 is suitable for high temperature measurements up to 900°C.

3.3.3 Diamond Mounting and Alignment

Mounting diamonds in place is crucial to optimize the high pressure performance of DAC. Before mounting, the diamond should be cleaned by ultrasonic machine to reduce the surface contamination. Then one of convenient method for mounting is to glue the opposite diamonds to each backing plate by epoxy such as a mixture of epoxy 2850 and catalyst 9 (Emerson & Cuming Company) with the mass ratio of 100:3.5. However there are several disadvantages resulting in a short lifetime of the glue. At first, it can partially react with the clean reagent such as acetone and ethanol. The glue often can not last a long time after several cryogenic cycles due to the brittleness at low temperature and the stresses induced by the different thermal expansion of diamonds and backing plates. Further more, in the synchrotron x-ray measurements, the high-intensity radiation can damage the polymer structure and then reduce the adhesive ability. As a result, anvils can fall off and need be re-mounted and realigned. Some other mounting methods can be used as the relatively important alternatives, such as using a clamp ring or a metal leaf spring, or soldering the anvils on the backing plate.

Maintaining the alignment of diamond culets is essential to optimize the maximum hydrostatic pressure and to avoid the diamond breakage. Before checking the alignment, the contaminations and sample particles should be clean up from the diamond surface. The two opposite anvils are gently pushed together. One of the diamond anvils is fixed on the backing plate, but the other can be adjusted in motion to be parallel with its seat through a microscope by viewing from the side of DAC. Further alignment can be achieved by

rotating the movable anvil by viewing through the diamond. The interference fringe rings between diamond culets indicate the parallel status. The fringes are caused from the air wedge between the non-parallel culet faces. The more rings represent the larger tilting angle. When all fringes disappear and the culets show homogeneous "gray", the perfect alignment can be achieved, shown in Figure 3.2 (d)[72]. Care must be taken to apply pressures when touching the diamonds to check alignments since cracks on the surfaces can occur without a gasket between diamonds.

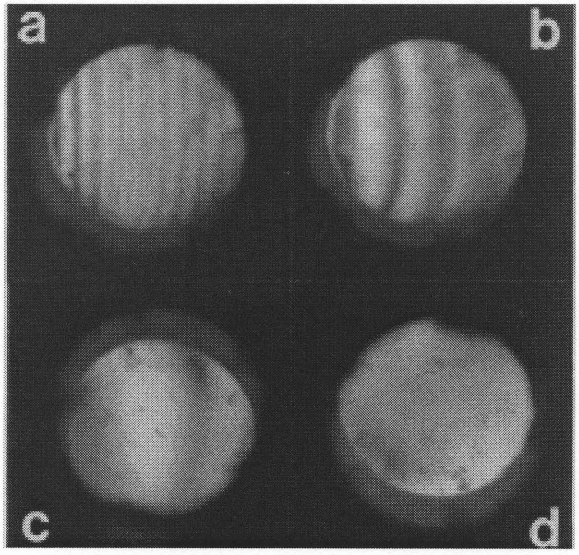

Figure 3.2 DAC alignment through observation of the Newton interference fringes caused by the contacted anvils[72].

3.3.4 Gasket Materials and Making

As shown in Figure 3.1(b), the gasket provides an encapsulated chamber in which the pressure transmitting media applies a hydrostatic pressure to the sample. Furthermore, the gasket supplies a buffer between the opposite diamond anvils to avoid their failure due to shear strength and extremely high pressures.

For these purposes, the gasket materials should have excellent mechanical strength, such as shear strength and thermal expansion, to reduce the pressure gradient inside the sample chamber. Suitable gasket materials include steel, stainless steel, rhenium, and alloys such as Cu-Be or Inconel (Ni:Cr:Fe=72:16:8). Composite gaskets like pyrophyllite[73] or lithographic stone[74] or corundum insulator materials sandwiched between metal layers have been used for electrical measurements or high temperature measurements.

The dimensions of gasket hole (sample chamber), including the diameter and thickness, play an essential role on the pressure limit. When high pressure is applied inside the sample chamber, a pressure gradient can lead a failure of gasket by a shear force. Therefore, a suitable diameter-to-thickness ratio should be reached to balance the shear force of the gasket with the friction between the gasket and anvils. Typically the diameter of gasket hole is around 1/3 of d, the culet diameter. For example, for a 400μm culet the stainless steel gasket should be drilled with the diameter ~130 μm and the indentation thickness ~60 μm to optimize the pressure limit up to ~40 GPa.

For making a gasket hole, pre-indentation before drilling is crucial not only to position the hole but also to improve the stability of pressure regime. When the gasket is squeezed by the diamond anvils, it deforms physically and extrudes outward as shown in Figure 3.1(b). Generally, a typical initial thickness ~250 μm gasket may be pre-indented to 50-80 μm. After centering the drilling tools in the indented area, the gasket hole can be drilled by many different approaches such as mechanical drilling, sparking erosion and laser beam burning.

In general, sparking erosion is most popular and economic method to make the gasket hole for electrical conductive materials. The instrument named the electric

discharge machine (EDM) has been widely used for those hard metal gaskets such as tungsten, rhenium and stainless steel. Figure 3.3 shows the basic circuits of electrical discharge machine, including a DC power supply of 0-50 V, resistor R1 of 100 Ω and R2 of 4 Ω, and a variable capacitor C. The size, quality and drilling rate of the gasket hole can be relatively controlled by adjusting the capacitor. The XYZ stages used in Figure 3.4 are to position the gasket hole drilling by centering the tungsten cutting wire. The commercial EDM has a voltage feedback system to automatically control the drilling speed and drilling depth, but it cost much more than this home-made EDM.

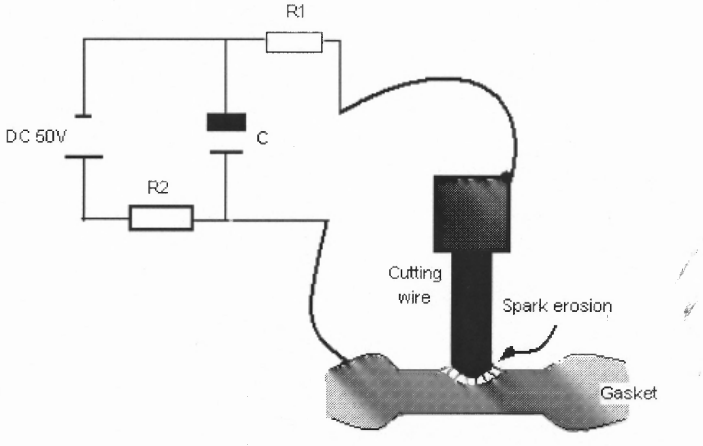

Figure 3.3 Principle of an electric discharge machine (EDM) and its basic electrical circuit diagram.

Moreover, dielectric fluid is another important factor for the drilling quality. When the discharge passes through the dielectric fluid, spark melts the gasket metal; then during the discharge ceases, the dielectric fluid flushes the molten rust off the gasket surface. Several fluids such as vacuum pump oil, machine oil, kerosene, methanol and ethanol can be used for different metals. In usual, thinner fluid should be used for hard materials while soft materials need a more dense dielectric fluid.

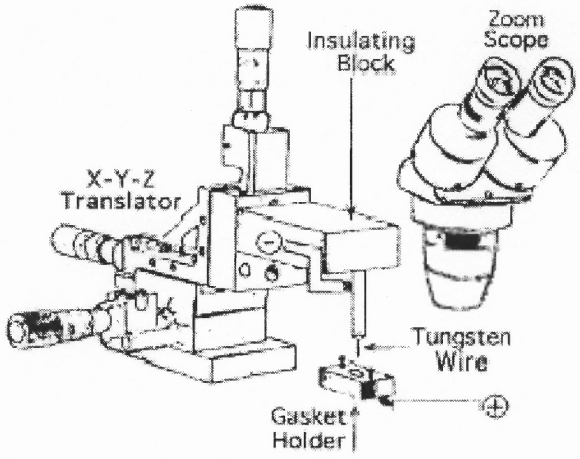

Figure 3.4 The mechanical setup of EDM including XYZ translator and microscope for positioning the gasket center under the cutting wire[75].

3.3.5 Pressure Media and Loading

The pressure transmitting media is essential to ensure homogeneity of the applied pressure inside the sample chamber. Choosing the suitable pressure media can minimize the pressure gradient to achieve a hydrostatic or quasi-hydrostatic pressure over the required pressure range. The usual pressure media includes liquids media (methanol, ethanol, water and silicon oil), solid media (AgCl, NaCl, KCl and KBr), and gas media (Helium, Nitrogen, Argon and Neon). Table 3.1 shows the media performance under pressures.

Solid pressure media with low shear strength are easy to be load into the sample chamber, which is suitable for some special optical measurement. For example, KBr can be used to measure the mid-IR spectrum, due to its low absorption for this wavelength range. However, the non-zero shear strength of solid induces a large pressure gradient over a high pressure to form non-hydrostatic pressure distribution.

Liquid pressure media are convenient to use and maintain quasi-hydrostatic pressure within a relatively large pressure range. But the pure component liquids can

crystallize at a modest pressure, although they still show liquid-like states. The mixture of several media may retard the transformation from liquid to glass and the increase of shear strength until a relatively high pressure. For example, the mixture of methanol, ethanol and water with a special ratio can improve the maximum quasi-hydrostatic pressure from ~8.6 GPa of methanol to ~14.5 GPa. The loading process of liquid media is quite easy. After loading the sample into the gasket hole and placing ruby chips on the culet surface of the diamond anvil, we use a syringe to drop the liquid media into the gasket hole and then cover the opposite anvil to seal the sample chamber.

Table 3.1 Performance of Pressure Transmitting Media.

Medium	freezing P (GPa)	(quasi) hydra-Static pressure (GPa)	Comments and Ref.
Silicon Oil		2	freezing at low T
water		2.5	freezing at low T
Isopropyl alcohol		4.3	freezing at low T[76]
Glycerine: water (3:2)		5.3	freezing at low T[77]
Methanol		8.6	freezing at low T[76]
Methanol:water (4:1)		10.4	freezing at low T[76]
Methanal:ethanol:water (16:3:1)		14.5	freezing at low T[78]
Hydrogen	5.7	177	[79]
Helium	11.8	60-70	[80]
Neon	4.7	16	[80]
Argon	1.2	9	[80]
Xeon		55	[81, 82]
Nitrogen	2.4	13	[83]
FC84:FC87 (1:1)		4.9	Working for low T(77K)
FC70:FC77 (1:1)		4.9	Working for low T(77K)

The gaseous media can acquire a much higher pressure range due to its lowest viscosity and almost zero shear strength. Also because of an extremely low liquefying temperature, these gaseous transmitting media can work well in low temperature. The major problem of using gas media is that they have large expansion rate from liquid. So the

best way is to load the liquid form of the media by cooling the whole DAC below the boiling temperature.

3.3.6 Pressure Calibration

Pressure measurement in the sample chamber is a major problem due to the uncertainty of the contribution from the external applying force due to the internal frictions and the gasket deformation. Several pressure calibration techniques have been developed, such as measuring the magnetic transition temperature of In, Pb and $ErCO_2$ or the resistance of standard samples Mn, InSb etc. For the x-ray diffraction at high pressure, some standard makers, such as NaCl, Al, Au, Pd, Pt and quartz with high compressibility, are used. The unit-cell volume and lattice parameters can work as the pressure indicators in situ, since the equations of state are known.

The most popular and convenient approach for pressure calibration is to observe the fluorescence shifts of luminescence sensors, such as ruby or Re-doped oxyhalogenides and so on. Ruby, Cr^{3+} doped α-Al_2O_3, is known to be quite stable and no phase transition up to ~100 GPa, which is suitable for broadly use in DAC. Even for the ruby chips with the diameter of 10 μm, the sufficient fluorescent signals can be induced by blue-green laser beam. The ruby spectrum shows doublet peaks R1 and R2 with the corresponding wavelengths of 694.2 nm and 692.8 nm at the ambient pressure and temperature. With applied pressure increase, the doublet peaks both have obvious red-shifts in near linear trend. Mao and Bell *et al.* proposed a relative accurate formula by calculating the equation of state for several metals under hydrostatic and non-hydrostatic pressures and calibrating an empirical quasi-linear formula up to ~180 GPa[84]:

$$P(GPa) = 1904[(\lambda_{p,T} / \lambda_{0,T})^{B} - 1] / B \qquad \textbf{(3.2)}$$

Where $\lambda_{0,T}$ is the wavelength of ruby R1 line at the ambient pressure and the fixed temperature ($\lambda_{0,300K}$=694.2nm), $\lambda_{p,T}$ is the wavelength at the applied pressure P in the unit of GPa and the same temperature. B=7.665 is for quasi-hydrostatic while B=5 is for hydrostatic conditions.

Furthermore, the wavelength R1 also has strong temperature dependence. The wavelength correction is shown as[85]:

$$\Delta\lambda_p(T) = C_1 \times \Delta T + C_2 \times \Delta T^2 + C_3 \times \Delta T^3 \quad \textbf{(3.3)}$$

So the temperature dependence of the R1 wavelength at the given pressure is:

$$\lambda_p(T) = \lambda_p(T_0) + \Delta\lambda_p(T) \quad \textbf{(3.4)}$$

In hydrostatic pressure range, the separation of R1-R2 doublet peaks retains almost constant. With the pressure increasing, both peaks become broader and then the separation decreases until the overlapping of the doublet peaks. Overlapping of the R_1 and R_2 lines at low pressures is an indicator of non-hydrostatic conditions.

Table 3.2 Comparison of Luminescence Pressure Sensors.

Calibrant	$\lambda_{p=0}$ (nm)	$d\lambda/dP$ (nm GPa^{-1})	$d\lambda/dT$ (x 10^3 nm K^{-1})	$(d\lambda/dT)/(d\lambda/dP)$ (x 10^3 GPa K^{-1})
Cr^{3+}:Al_2O_3	694.2	0.365	6.3	17
Sm^{2+}:SrB_4O_7[86, 87]	685.4	0.255	-0.1	-0.4
Sm^{2+}:BaFCl[88]	687.6	1.1	-1.6	-1.5
Sm^{2+}:SrFCl	690.3	1.12	-2.36	-2.1
Eu^{3+}:LaOCl	57837	0.25	-0.5	-2
Eu^{3+}:YAG	590.6	0.197	-0.54	-2.5

Under simultaneous high-pressure and high-temperature conditions, the ruby sensor shows strong temperature dependence on wavelength. Some alternative materials with smaller temperature dependence but larger pressure dependence have been used. Several rare-earth elements-doped compounds have been investigated in Table 3.2.

3.3.7 Application of Force

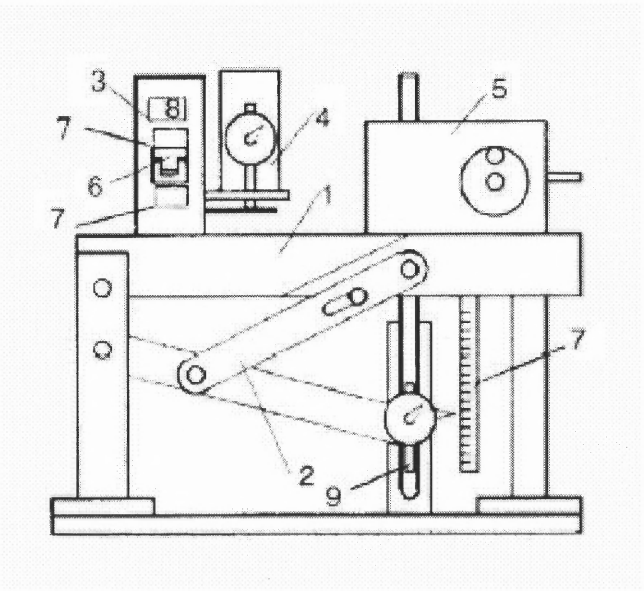

Figure 3.5 Automated high-pressure setup: (1) table; (2) lever mechanism; (3) pressure chamber; (4) sensor of plunger displacement; (5) reduction gear with the electro-motor and handle drives; (6) portable cassette with pressure anvils, container and sample; (7) thermal regulators; (8) sensor of plunger stress; (9) sensors of lever springs contraction[89].

In the diamond anvil cell, pressure is generated by squeezing the two opposite diamonds together. Generally, even a small external force can produce a relatively high pressure inside the sample chamber by the design of DAC with small culet size. Several different devices have been used for providing a stable and uniform external force, such as a lever-arm device and inflatable device. Among all these methods, force generation by screws/bolts is the most convenient and economical way with a much simpler design. Further, the use of threads with half the standard pitch can obtain more accurate and controllable pressure steps.

Most recently, Shchennikov *et al.*[90] designed a mechanical apparatus to provide continuous pressure automatically, in which the electromotor (handle) drive produce the

load force transferring to the high-pressure plunger by a mechanical level. This portable device can achieve nearly consecutive pressure up to ~30 GPa, shown in Figure 3.5.

3.4 High Pressure Experiments at High Temperature

For HP-HT experiments, it is necessary to heat the sample chamber in the experiment duration. There are several heating approaches, whose advantages and disadvantages make the selection important.

1) External resistive heating raises the temperature of both sample and anvil simultaneously by wrapping the heating coil outside DAC, which limits temperature to ~1000°C due to the graphitization of diamonds (some specific cements are used as the adhesives to hold the diamonds)[91, 92].
2) Internal resistive heating is using a heating wire through sample chamber, which provide a homogeneous temperature distribution and higher temperature limit up to ~2000°C[93, 94]. However, for such tiny sample chamber the insert wire disturbs the loading of sample and pressure medium.
3) The highest temperature above 4000°C can be reached by using laser heating and it is very convenient[95, 96]. But the key weakness is the extremely large temperature gradient up to ~400°C/μm inside the sample chamber.

3.5 High Pressure Experiments on Magnetization and Resistivity

For magnetic characterization under high pressure, both direct and indirect methods are exerted broadly. Indirect methods, such as neutron scattering, show the high pressure effects on magnetic properties by determine the magnetic structure. Temperature

dependence of diffraction peaks can be used to identify antiferromagnetic and ferromantic peaks (as opposed to nuclear scattering peaks)[97, 98]. Due to the simple device for neutron scattering approach, it can acquire ~100 GPa pressure like x-ray diffraction. However, neutron source is too expensive to be reached. Direct methods include high-pressure measurements of magnetization moment M and susceptibility χ.

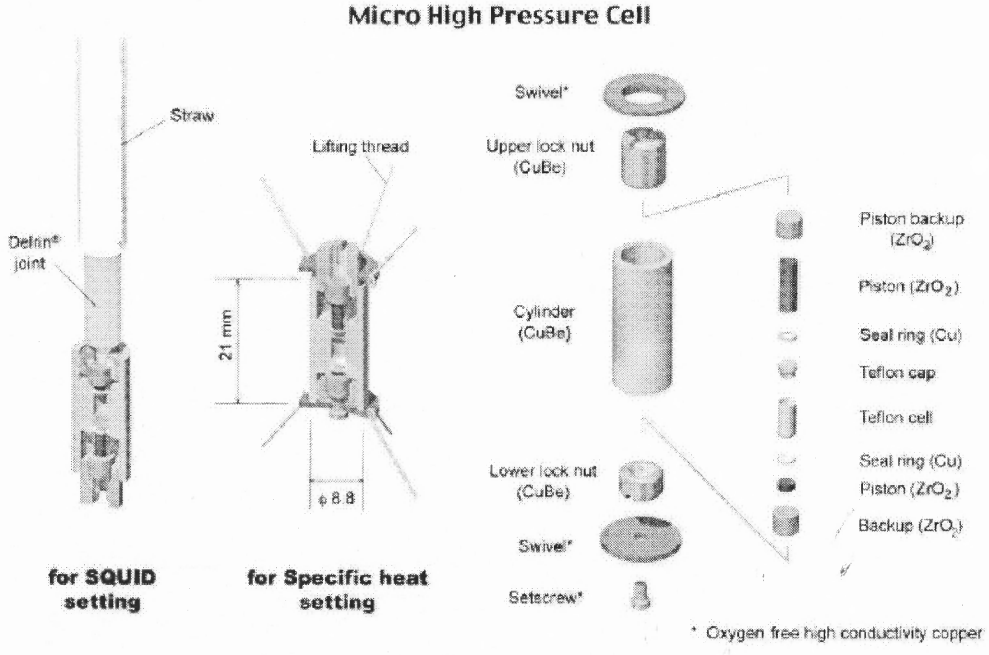

Figure 3.6 A schematic drawing of high pressure micro-cell[99].

Uwatoko *et al.*[99] developed a complex hydrostatic pressure cell for magnetization and heat capacity measurements across the low temperature range by SQUID magnetometer (Quantum Design), shown in Figure 3.6. But the pressure limit can not exceed ~2.5GPa. In 2003, Alireza *et al.*[100] presented a micro-coil system for susceptibility study up to ~7.5 GPa in DAC. For higher pressure purpose, Weir and Jackson fabricated microcircuits on the diamond anvil, which was covered by depositing artificial diamond layer. This new type design makes it possible to probe resistivity, heat capacity and

magnetic susceptibility under the high-pressure up to 50GPa and also high temperature up to ~2900 K[101].

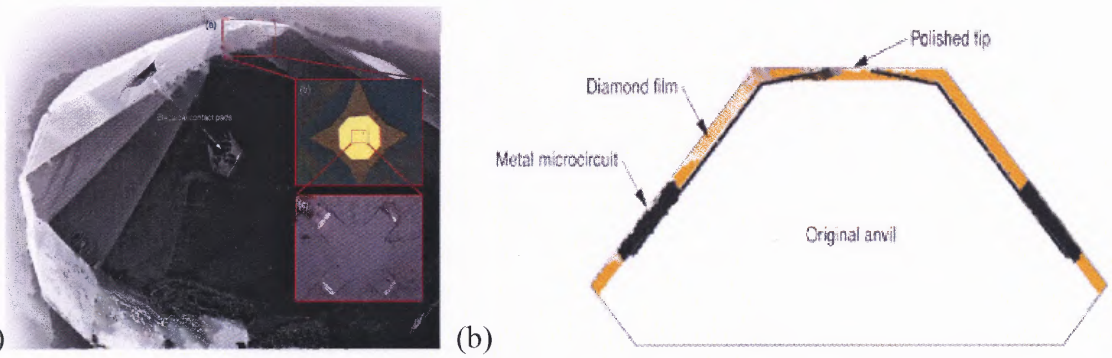

Figure 3.7 (a) Scanning Electronic Microscope photos of new type of DAC for conductivity measurement and the inserts showing electrical connectors on the tip of diamond culet; (b) cross section graph for this new design[102].

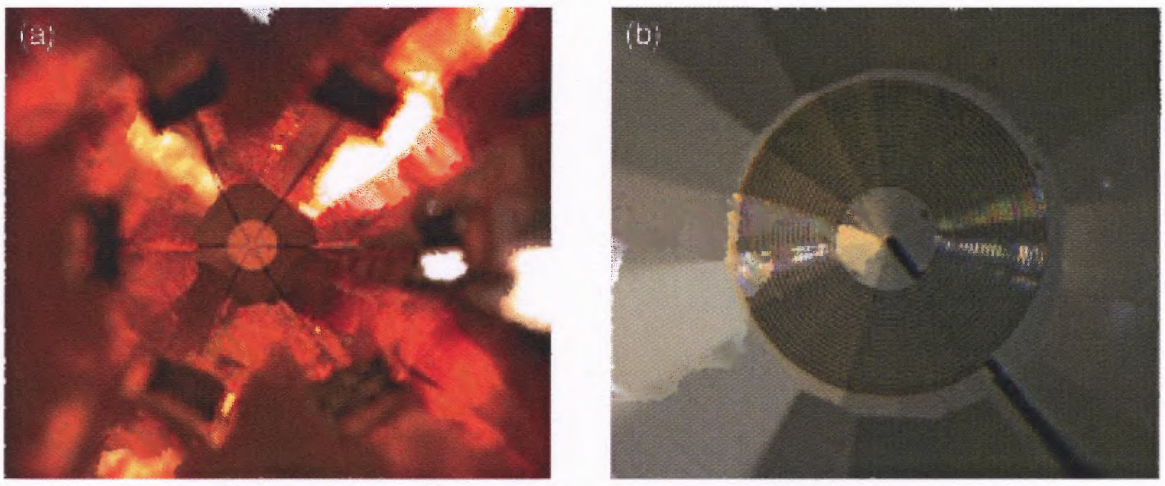

Figure 3.8 Each type of design for different properties: (a) electrical conductivity measurement, (b) magnetic susceptibility measurement[102].

In 2004, to improve the experimental capability under high pressure up to ~100 GPa and high temperature up to ~2900K, the scientists from Livermore and University of Alabama designed some new types of DAC (Figure 3.7 and Figure 3.8).

By two-dimensional optical lithographic methods, a tungsten micro-circuit is fabricated on the diamond culet. And then a 10~50 -micron single crystal diamond layer is deposited by plasma enhanced chemical vapor deposition (PECVD) to protect the circuit. The rough diamond culet is polished to a smooth surface with a tolerance of 1 micrometer, and microprobes are completely encapsulated except several electrical connectors on the tip of diamond culet and the anvil side.

3.6 High Pressure Techniques for Resistivity Measurements

3.6.1 Gasket Preparation

The gasket is an essential factor in our high-pressure experiments. The quality of the gasket material and preparation not only determines the maximum hydrostatic pressure in the sample chamber, but also protects the diamond anvils from breakage under non-hydrostatic conditions.

In our work, considering the pressure requirement and the quality of materials, we choose Stainless Steel, AISI302 (Fe/Cr18/Ni8), to prepare gaskets with a starting thickness of 250μm. To fit the diamond anvil cells used in the resistivity measurements, the stainless steel sheet is cut into small rectangles with a dimension of 6mm x 15mm, in which a guiding hole then is drilled to maintain gasket mounted on the same position of DAC for each loading. To reduce the deformation of gasket hole under high pressure, another step named pre-indentation is added. The depth of indent can be monitored and controlled with a micrometer. Typically 100μm depth of indent is enough to reach ~6GPa for our resistivity measurements.

The next step is to drill a gasket hole, which size depends on the pressure we need. To get higher pressure, the hole should be smaller to avoid deformation and collapse. But for resistivity measurements, it is much more convenient to work with a large hole for sample loading. We make 350μm-400μm gasket holes for resistivity measurement with the stainless steel gasket thickness of 250μm and culet diameter of 800μm. In addition, the hole position and shape are important quality factors. The center-position and round-shape of gaskets are needed to enable hydrostatic condition to higher pressure range. To drill the gasket hole, a home-made electrical discharge machine (EDM) has been used with a similar design as Lorenzana's[75], shown in Figure 3.3 and Figure 3.4. The DC power supply is a variable source from 0 to ~50 V, which can be adjusted to control the drilling rate and quality of the gasket hole. A tungsten wire (the diameter of ~200μm) with a sharpened tip works as the cutting wire. Usually, it takes around half an hour to drill an indent with a thickness of 100μm. After both sides are drilled, an adjustment by a sewing needle is necessary, which gets a vertical hole-wall for hydrostatic pressure.

For resistivity measurements, another key but difficult step is to deposit an insulator layer on the metallic gasket. To reduce the failure of the insulator layer, the gasket needs to be cleaned by boiling it in acetone. Two insulator layers at different regions are deposited on the steel gasket, shown in Figure 3.9.

On the outer part of insulating layer: we fix four outer connection leads. The Stycast 2850 epoxy is the best choice for mounting the wires and the insulator layer due to its excellent thermal expansion properties. The Stycast 2850 epoxy is fully mixed with Catalyst 9 to acquire better adhesive ability and mechanical strength. The epoxy need to be cured for several hours at RT or be annealed at ~100°C for fast cure.

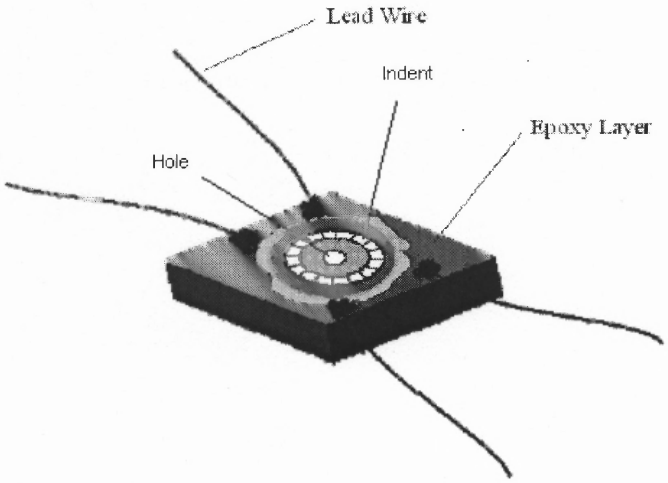

Figure 3.9 Gasket preparation for resistivity measurement.

Inner part of insulating layer: Mix Al_2O_3 powder and Stycast 1266A, and then stir the mixture in one direction until it is uniform. Add proportional Stycast 1266B to the mixture and mix them as mentioned. The mass ratio of Al_2O_3 powder, Stycast epoxy 1266A and 1266B is 1:1:0.123. Here a little more Al_2O_3 powder is added to harden the inner layer to reduce the deformation when higher pressure applied. Coating the mixed epoxy on the inner part of the gasket including the indent area and the inside wall of the gasket hole. This will insulate the steel gasket for the Van der Paul Method resistance measurement.

With gasket prepared in this way, the highest pressure reaches ~6 GPa in the resistivity measurement.

3.6.2 Sample Preparation and Loading

As usual, two methods have been used for resistivity measurements. Standard four point method has higher accuracy but it requires more precise wire connections on the sample. However, Van der Paul method with four-point connections on the corners of sample

sample surface is a better choice for high-pressure resistivity measurement when the shape is not well known, due to the limitation of gasket hole. Comparison with of ambient pressure measurements with for DAC samples and large bulk samples are done to calibrate the resistivity curves.

At first, the polycrystalline sample pallet is polished to a sheet of 40-70μm in thickness. The resistivity sample with the lateral dimension of 150-250μm is cut from the polished sample pallet. The most difficult step is to attach four gold wires on the sample surface. To improve the quality of leads, a new approach has been introduced by Matsuzaki[103]. According to the instruments and tools in our lab, the method is simplified by using two xyz stages as shown in Figure 3.10. The lead-making includes the following steps:

(1) The gold wires are cut into short pieces with a length of 2-3 mm and adhered by silver paste in parallel on the glass slide. To enhance the adhesive ability, the gold wires need to be straightened by hand and the tips of wires need to be flattened by using micro-tweezers.

(2) The sample pallet is polished to ~50-100 μm thickness and then tailored into a square-piece with the lateral dimension of ~150-250 μm, which freely sits on the glass slide of another xyz stage.

(3) A tiny droplet of silver paste is brushed onto the loose end of the gold wire by a fine-tipped needle.

(4) Aiming at one of sample corners, the gold wire is pushed and attached on the surface precisely by motions of the xyz stages.

(5) Wait for 2-3 minutes until the droplet is dry on the sample surface. Then the wire is

cut to ~1 mm. The sample is rotated to the other empty corners successively to attach the gold wires.

(6) Steps (3)-(5) are repeated until all four leads are attached.

(7) After the four leads are glued, the sample should be cured for more than half an hour at ~80°C. (Note: It is very important to use high quality of silver paste, which used in our experiments is from Alpha Aesar)

(8) The leads should be examined to check that no short-cut occurs.

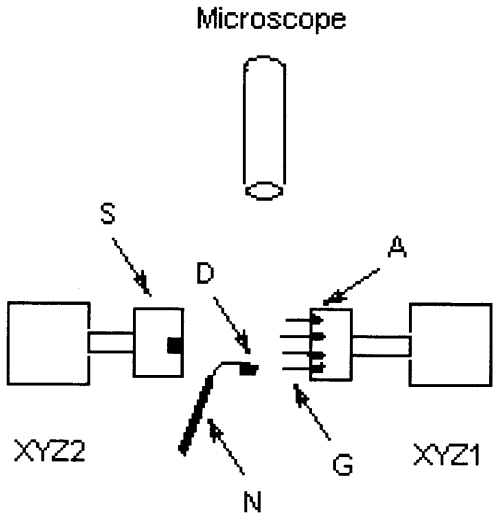

Figure 3.10 A schematic diagram of the process to attach electrical leads on sample surface. XYZ1 and XYZ2 are mechanical XYZ stages. A, adhesive (silver paste); D, droplet of silver paste; G, gold wires; N, needle with a fine tip; S, slides (glass).

Due to the tiny sample dimensions, all work should be conducted under the microscope. Because of the fast drying of silver paste, the attachment need to be done as fast as possible.

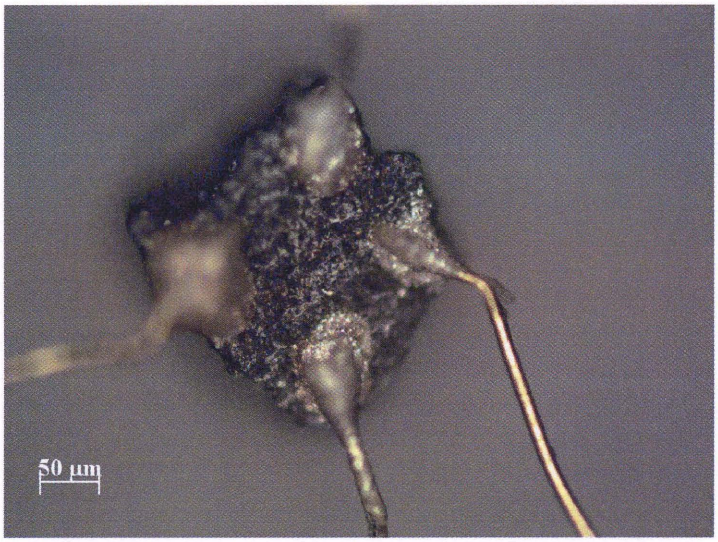

Figure 3.11 Photograph of a finished sample with four leads attached.

In a traditional method, the leads are glued by hands, which may cause bad connection quality due to some human factors such as shaking fingers. However, this new approach uses a more reliable and more precise mechanical instrument to improve the efficiency of lead attachment. This approach can be quickly learned for a beginner.

For the high-pressure resistivity measurement, the wired sample needs to be mounted into the prepared gasket as described in subsection 3.6.1. At first, the four wires are glued on the indent with a little silver paste. Then the connections are extended from the samples leads to the external leads by using silver paste. Here silver paste is a good choice for connections, due to its excellent ductility on the insulator layer under high pressures. Before the sample set can be loaded into the DAC, the silver paste should be cured for ~1/2 hour at bout 80℃. The loaded sample in the gasket hole has been shown in Figure 3.12 and Figure 3.13.

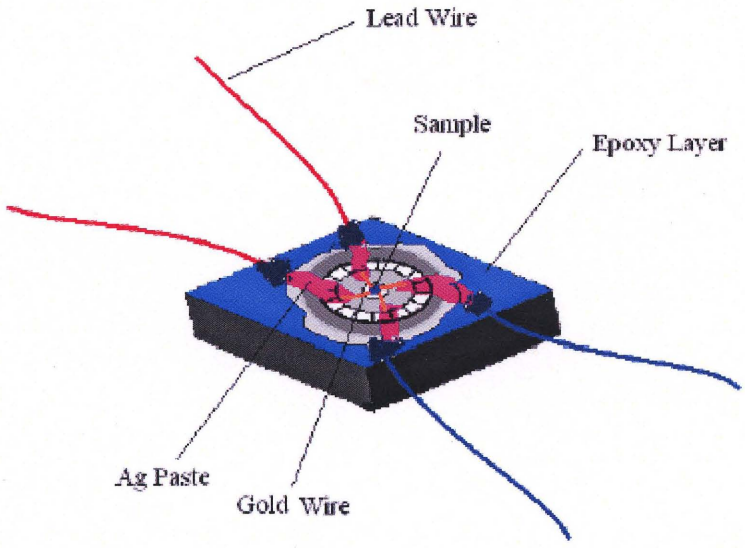

Figure 3.12 Schematic of the complete sample and gasket set for high-pressure four-probe resistivity measurements.

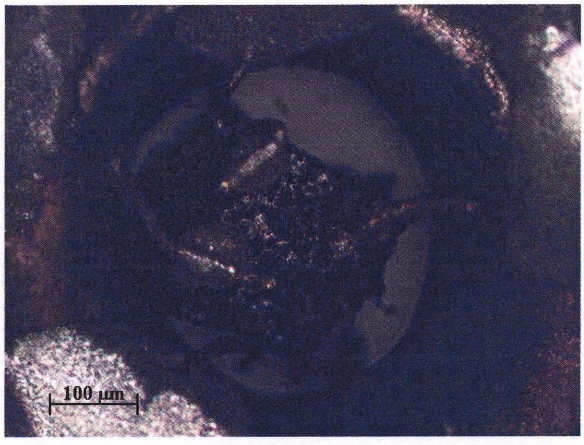

Figure 3.13 Photograph of a sample mounted into the gasket for high-pressure resistivity measurement.

As described by Dunstan and Spain[69, 70], the sample loading for resistivity measurement is much easier than other previous steps because the sample is already fixed with the gasket. To avoid the squeezing in the gasket hole, ruby chips less than 10μm are chosen for pressure calibration and loaded to surround the sample. Due to the tiny size, the

ruby chips are better to be adhered by a film of vacuum grease onto the culet of DAC. After the gasket set is mounted and the liquid pressure medium is filled, another side of cell is put on the top of gasket. Then the whole DAC is sealed by tightening screws. Because our resistivity measurement runs from ~77K (liquid nitrogen) to 300K (room temperature), FC-77 is chosen as the pressure medium, which has lower freezing temperature.

3.6.3 Resistivity Measurement System

The high-pressure resistivity measurement system includes a Janis cryostat, a Keithley 2400 source-meter, and LakeShore 330 temperature controller. The measurement data including temperature and resistance are automatically controlled and recorded by using a program in LabView. The cryostat with four optical windows can be operated in the temperature range from liquid helium to 325K. The sample with DAC is mounted on a holder inside the cryostat and the pressure can be calibrated in situ through the optical window by checking the fluorescence spectrum of ruby chips. A diode laser system is used for producing the green light. Several ruby chips are loaded around the sample at different positions and the temperature dependence of the ruby R1 line shift is also considered. Therefore, the average pressure and pressure variance can be obtained.

3.7 High Pressure Techniques for Synchrotron XRD Measurements in Our Work

In high pressure x-ray diffraction (XRD) measurement with DAC, The x-ray beam must go through both of the diamond anvils (~5 mm). Figure 3.14 shows that the cut-off energy of diamond anvils is around 12-18 keV. The x-ray transmission coefficient reaches 50% at ~20 keV. So for the conventional x-ray generator of Cu Kα line with low energy photon, the beam signal may be significantly attenuated by diamonds. Also the low photon flux

produced by the conventional x-ray tube can not provide enough intensity for the amount of sample in gasket hole (typical sample volume of 100μm x 100 μm x 30 μm). In addition, the small opening angle of the cell limits the usage of DAC in the rotating anode x-ray machine.

However, these problems can be solved by using synchrotron radiation source, which has continuous spectrum from IR to hard x-ray region. Compared to a conventional source, a synchrotron x-ray beam has much higher brightness and can be easily focused to a micron-size beam, which makes it as an idea light source for high-pressure x-ray diffraction in DAC. Wiggler beamlines such as X17 at NSLS have high flux in the hard x-ray region (above 50 keV). But since the small opening angle of DAC and beam wavelength, the synchrotron x-ray data reduced the resolution if a large sample to detector distance is not used.

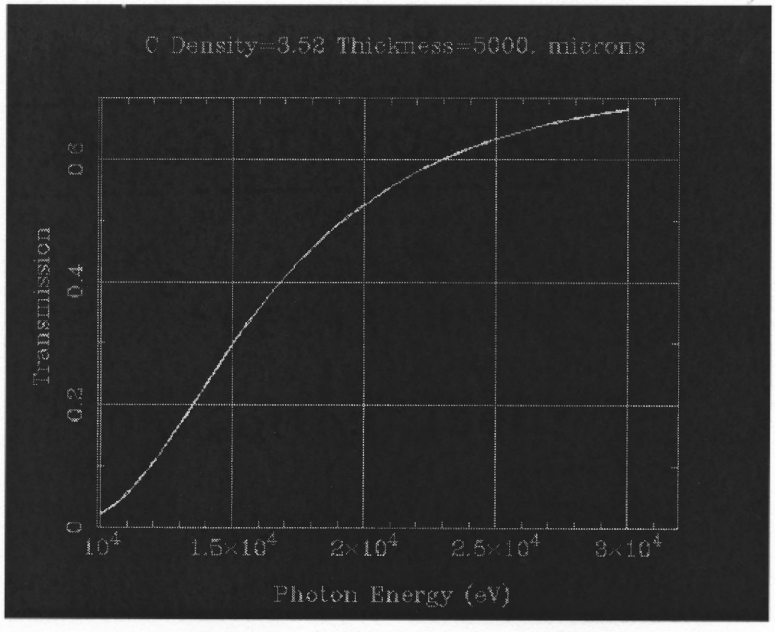

Figure 3.14 The x-ray transmission of diamond anvils versus photon energy (eV).

For high-pressure synchrotron XRD, standard stainless steel gaskets can be used. To achieve excellent powder diffraction data, the sample needs to be grinded and sieved by a 500-mash sieve (25μm) or smaller in order to increase the number of particles in the x-ray beam. X-ray beams with the spot size of 50μm x 50μm were used. Due to small size of sample chamber (gasket hole), as much powder sample should be loaded as possible. So the powder is squeezed into a tablet with thickness of 30-50μm and then cut into tiny pieces with 50-100μm dimensions. The method by using another cell to compress powder into a pallet can work. Alternatively, a pair of tungsten carbide cubes and a c-clamp can also work. The ruby chips with size less than 10μm are adhered by vacuum grease on one of diamond culets. After the gasket is mounted, the sample tablet is loaded into the gasket hole and then liquid medium is filled. Because high-pressure synchrotron x-ray measurements are performed at room temperature, a mixture of liquid pressure medium, Methenol/Ethenol/Water with a ratio of 16:3:1, is chosen due to its higher hydrostatic pressure range up to ~14 GPa.

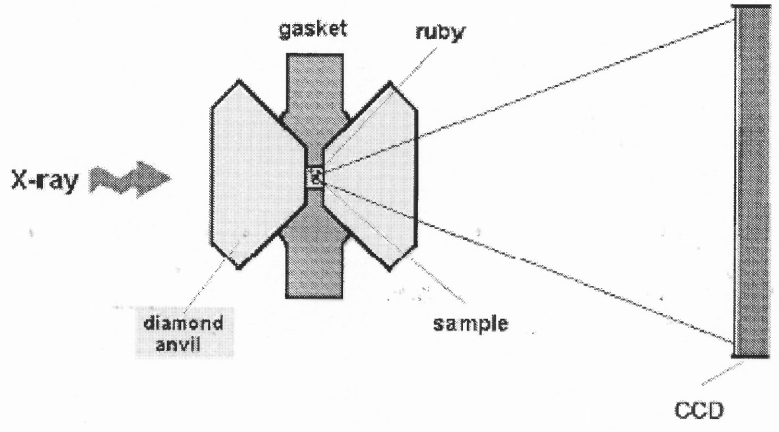

Figure 3.15 The set-up scheme of high-pressure synchrotron x-ray diffraction with DAC.

The focused synchrotron x-ray beam travels through the pair of diamond anvils and is diffracted by sample. The diffraction patterns are collected by a CCD system as shown in Figure 3.16.

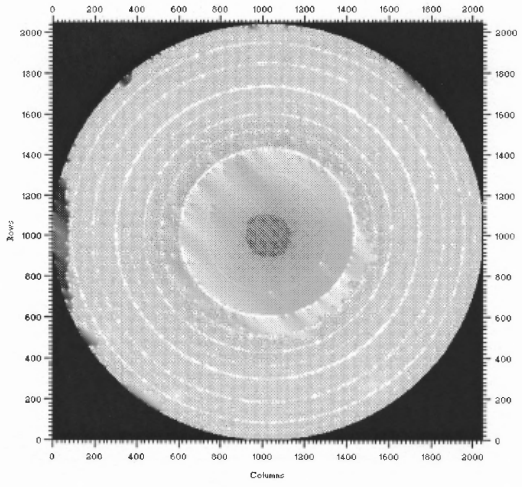

Figure 3.16 The synchrotron x-ray diffraction rings for sample $La_{0.85}MnO_3$ at ambient pressure at beamline X17b1 with λ=0.1825Å.

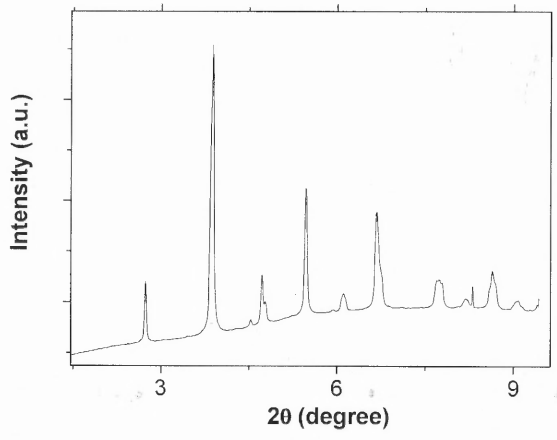

Figure 3.17 The diffraction pattern of $La_{0.85}MnO_3$ is integrated from Figure 3.16.

High pressure X-ray diffraction measurements were conducted at the National Synchrotron Light Source, Brook Haven National Lab (using the beam line X17b1 and

X17c). A charge-coupled device (Mar, 2048 × 2048 pixels with 79μm resolution) was used to obtain the 2-Ddiffraction rings (Figure 3.16), which was converted to 1-D diffraction pattern by program Fit2D (Figure 3.17). Measurements at X17b1 were conducted with the x-ray energy of 67KeV and with a detector to sample distance of ~41 cm. For X17c the corresponding parameters were 30KeV and ~25cm.

Furthermore, the diffraction patterns can be fitted by Rietveld refinement. The detailed structural parameters, such as lattice parameters, atomic positions, bond lengths and bond angles, are obtained by Rietveld software named Rietica.

CHAPTER 4

PRESSURE EFFECTS ON ELECTRON TRANSPORT AND STRUCTURE

4.1 High Pressure Effects on Electron Transport and Structure of $La_{0.85}MnO_3$

4.1.1 Introduction

As has been stated earlier, the $Re_{1-x}A_xMnO_3$ (Re= rare earth and A = Ca, Sr, Ba) mixed valence (Mn^{3+} ($d^4, t_{2g}^3 e_g^1$)/ Mn^{4+} ($d^3, t_{2g}^3 e_g^0$)) perovskite system exhibits complex and intriguing properties and an understanding of the basic physics of these materials has still not been realized[18, 104]. This system is being studied in both from fundamental science and as well as application perspectives. It has been found that a strong coupling exists among the lattice, spin, and electronic degree of freedom that are manifested by complex phase diagrams. The properties of manganites depend strongly on subtle changes in the structure and chemistry of the system induced by changing the Re or A site ion sizes[23]. Separating the changes in structure from the changes in valence can be accomplished by using series of Re cations with varying size at fixed Re/A ratio. However, precise control of the stable crystalline form produced by substitution is not typically possible. Modification of the structure by cation substitutions may alter the system in unpredictable ways.

A controllable way to explore the effect of strain or pressure on these systems is to apply hydrostatic pressure and then to measure the transport and structural properties[105]. Not many high-pressure measurements have been conducted on manganites. Early temperature dependent studies of high magnetoresistance phase for pressures below 2 GPa

predicted a linear increase of the metal-insulator (MI) transition temperature with pressure[54, 106, 107]. More recent studies on the changes in the metal insulator transition temperature (T_{MI}) at pressures up to 6 GPa reveal that an optimal pressure is reached beyond which the transition temperature decreases with pressure[50, 51, 53]. Meneghini[45] *et al.* conducted studies (up to 15 GPa) on the effects of high pressures on the transport properties of $La_{1-x}Ca_xMnO_3$ (x=1/4), but the electrical transport data were presented only between ~190K and ~380K – limiting the access to the MI transition at high pressures.

The motivation for studying lanthanum deficient $La_{1-x}MnO_3$ is that it is chemically simpler than the chemically doped systems, such as $La_{1-x}Ca_xMnO_3$, yet possessing similar transport, magnetic and structural characteristics. For example, the studied system ($La_{0.85}MnO_3$) has a low-temperature magnetic saturation moment which corresponds to a theoretical value of ~3.55 μ_B/Mn site as in the case of the chemically doped systems. Note that the T_C and T_{MI} coincide approximately at ~ 250 K, which is close to what is obtained for $La_{0.67}Ca_{0.33}MnO_3$. The overall shape of the resistivity curves of $La_{0.85}MnO_3$ and the chemically doped materials coincide. Although the space group is different (monoclinic with β=90.78° for this system compared to orthorhombic for the $La_{0.67}Ca_{0.33}MnO_3$), the approximate ABO_3 perovskite structure is maintained in spite of the defects on the La site.

In order to understand the origin of the changes in the electronic structure of manganites at both high and low pressures and to compare this system with the classical ion doped systems, we conducted detailed high-pressure transport and structural studies.

4.1.2 Sample Preparation

A Polycrystalline $La_{0.85}MnO_3$ sample was synthesized by the conventional solid-state reaction. After required ratios of La_2O_3 and Mn_2O_3 are mixed completely, the powder was

compressed in a stainless steel die, calcinated at 950°C for 12 hrs, reground and repressed into pellets. The sample was reheated to 1300°C and maintained for 12 hrs for compound synthesis, then cooled down to 800°C with a cooling rate of 5°C/min and the furnace was turned off at 800°C. All cycles were conducted in air. In order to avoid chemical inhomogeneity, the processes of grounding, heating and cooling were repeated three times.

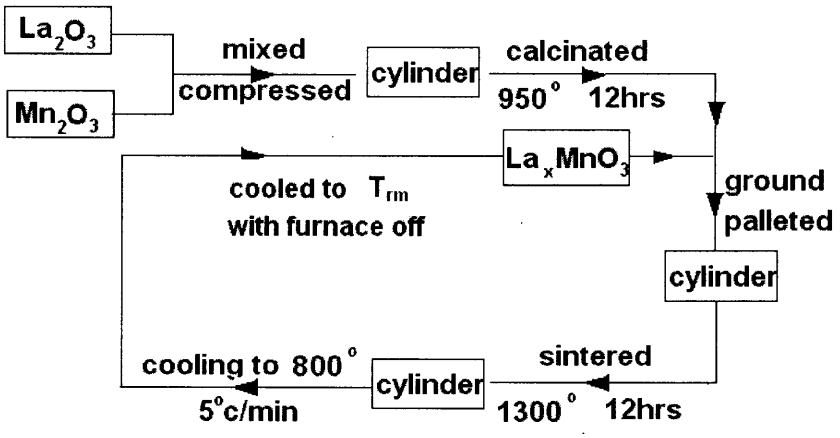

Figure 4.1 The flow chart for self-doped sample preparation.

The cationic composition of the pallet, determined by ICP (Inductively Coupled Plasma) method (by QTI corp.) yielding a ratio of 0.852 for La/Mn.

4.1.3 Conventional X-ray Diffraction

The polycrystalline sample $La_{0.85}MnO_3$ was characterized by x-ray diffraction, magnetization, resistivity and magnetoresistance measurements.

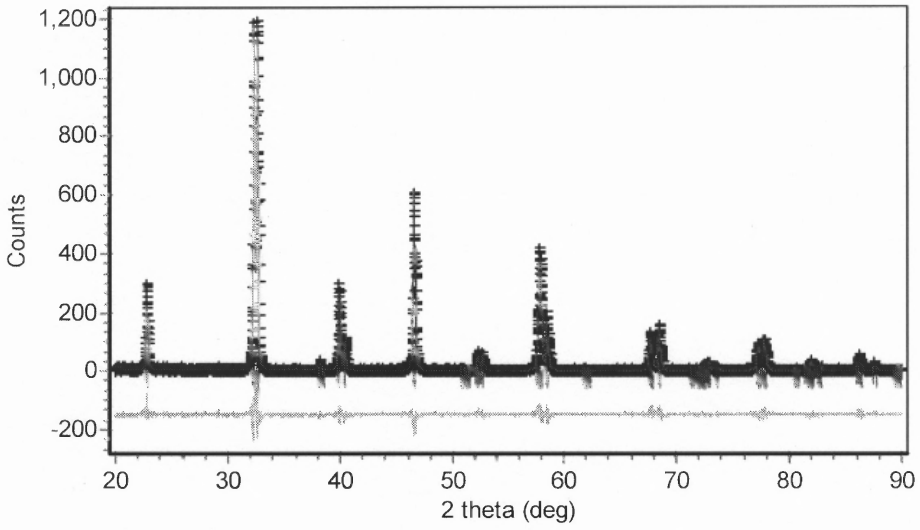

Figure 4.2 The conventional x-ray diffraction data (crosses) at ambient pressure with its Rietveld refinement (solid) and residual (lower line), and the fitting parameters are R_p=16% and χ^2=1.4.

The conventional x-ray diffraction pattern by Cu Kα doublets (Rigaku RINT 2100) at room temperature shows that the sample is in a single crystallographic phase. The Rietiveld fitting results (Figure 4.2) presented that this self-doped sample $La_{0.85}MnO_3$ has a monoclinic symmetry of space group I 2/a with lattice parameters of a= 7.7943(1) Å, b= 5.5286(2) Å, c= 5.4835(6) Å, and β= 90.814(4) °, consistent to the results published by Maignan[108] *et al.* The detailed structural parameters are listed in Table 4.1.

Table 4.1 Refined Structural Parameters for the Monoclinic I 2/a of $La_{0.85}MnO_3$ at Ambient Pressure.

Atom	Site	x	y	z	B	n
La	4e	0.25	0.501(2)	0	0.55(4)	0.852
Mn	4a	0	0	0	0.80(9)	1
O1	4e	0.25	0.11(3)	0	0.6	1
O2	8f	-0.013(1)	0.167(7)	0.336(3)	0.6	2

The magnetization measurements were performed by PPMS and MPMS system from Quantum Design, which utilize SQUIDs (Superconducting Quantum Interference Devices) technology. The sample $La_{0.85}MnO_3$ has a saturation value of ~3.5μ_B/Mn site, close to the theoretical limit of 3.56μ_B/Mn, with a Curie temperature (244.0 ± 1.0K) at a magnetic field H=0.5T. Figure 4.3 shows both the low-temperature magnetization and Curie temperatures are increasing with the magnetic field up to H=4.5T.

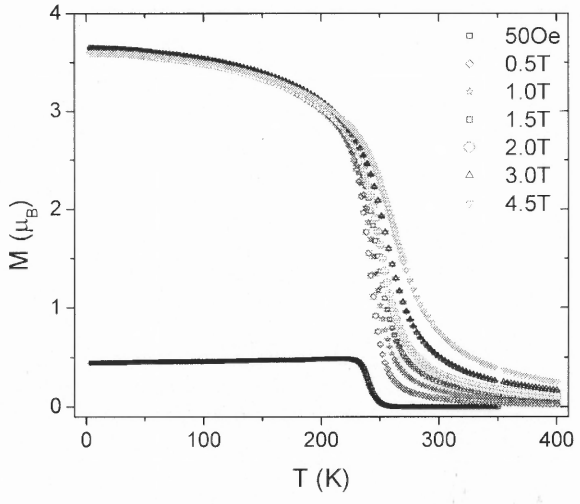

Figure 4.3 Magnetization versus temperature at various magnetic fields.

4.1.4 Resistivity Measurement at Ambient Pressure

The ambient-pressure resistivity was measured by standard four point methods. A bulk sample with a rectangle shape was used. It shows an obvious Metal-Insulator transition at T= 248.0 ± 1.0K consistent to its curie temperature, which means (considering also the magnetization measurements) it has a transition from ferromagnetic metal to paramagnetic insulator states (Figure 4.4).

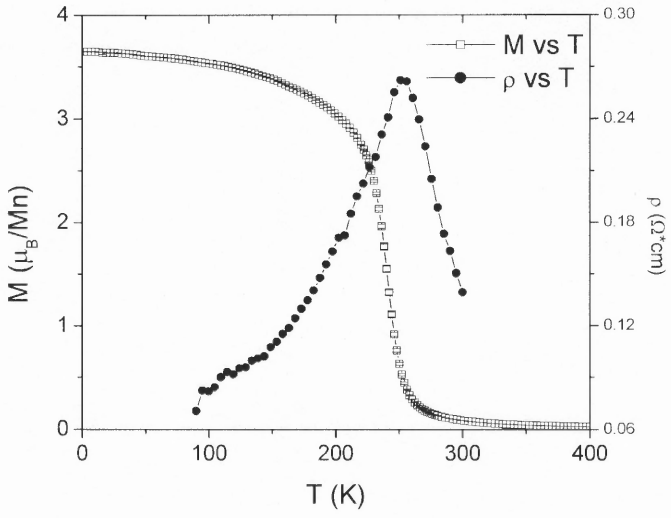

Figure 4.4 Ambient pressure resistivity and magnetization (at H=0.5 T) as a function of temperature for $La_{0.85}MnO_3$.

4.1.5 Magnetoresistance (MR) Measurement

As most of typical chemically doped perovskite manganites, this self-doped system $La_{0.85}MnO_3$ also shows strong CMR effects in magnetic fields. There are obvious magnetic effects on resistivity curves shown in Figure 4.5. It has a very large magnetoresistance (MR), larger than 60% for a magnetic field 7.5 Tesla at ~250K. With increasing magnetic field, the low-temperature (90K) resistivity and high-temperature (300K) resistivity drop with the rates of -4.5±0.8mΩ*cm/T and -5.9±1.1mΩ*cm/T, respectively. Magnetic fields enhance monotonously the metal-insulator transition temperature T_{MI} from 245.9K to 270.7K with a rate of ~3.3±0.5K/T. According to double-exchange (DE) mechanism, external magnetic fields align the spins of Mn atoms and enhance the electron hopping between neighboring Mn sites through O 2p orbital.

Comparison of magnetization (Figure 4.3) and magnetoresistance (Figure 4.5 and Figure 4.6) measurements of self-doped $La_{1-x}MnO_3$ with the classic CMR system chemical doped $La_{1-x}Ca_xMnO_3$ (x=1/4), the close similarities have been shown in Figure 4.7 by Huang *et al.*

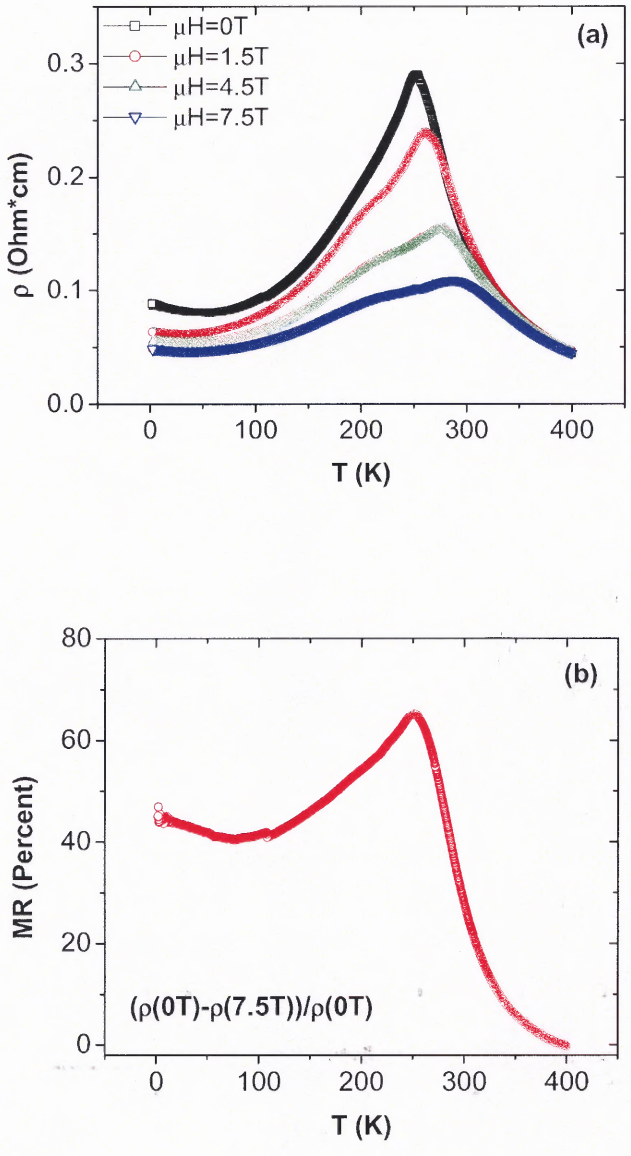

Figure 4.5 Magnetoresistance at different magnetic fields: (a) resistivity at various magnetic fields up to 7.5T, (b) magnetoresistance for the field of 7.5T.

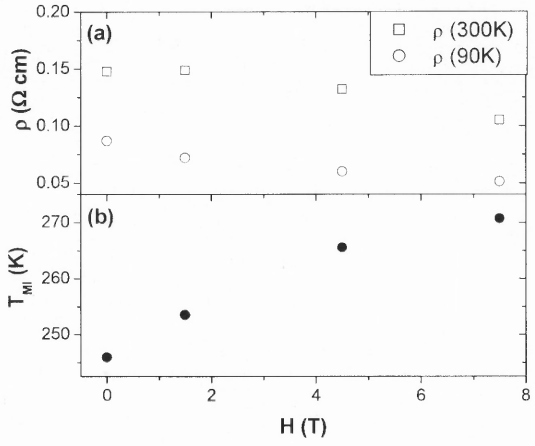

Figure 4.6 Magnetic field dependence of (a) resistivity at T=300K and T=90K, (b) Metal-Insulator transition temperature.

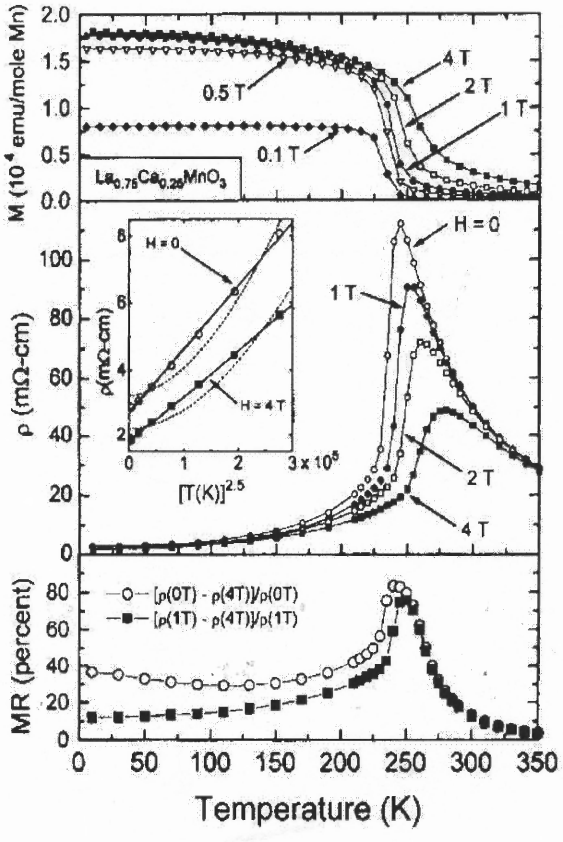

Figure 4.7 Magnetization and Magnetoresistance of $La_{0.75}Ca_{0.25}MnO_3$ at various magnetic fields up to 4T.

Compared with the pressure effects in the following section, the magnetic fields produce similar effects on resistivity as that of the lower pressure range below the critical pressure P*.

4.1.6 Electron Transport under Pressure

Figure 4.8 shows the electrical resistivity versus temperate for pressures ranging from ambient up to 5.8 GPa. At ~3.4 GPa (P*, the critical pressure), T_{MI} reaches its maximum value of ~280 K. The metal-insulator transition temperature T_{MI} is defined as the inflection point of the first-order derivative maximum of the resistivity curve.

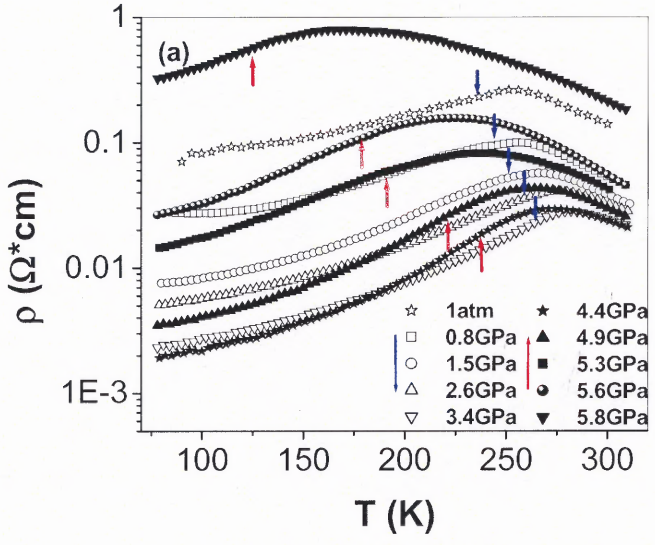

Figure 4.8 Temperature dependence of resistivity under various pressures.

In Figure 4.9, we present the resistivity at 300K and 90 K as a function of pressure. Note the increase in resistivity at high pressure. Similar results have been found for $La_{0.60}Y_{0.07}Ca_{0.33}MnO_3$[51], $Nd_{1-x}Sr_xMnO_3$ (x=0.45, 0.5)[50], and $Pr_{1-x}Ca_xMnO_3$ ($0.25<x<0.35$)[53]. In this work, we present the non-linear structural changes induced by

pressure in the self-doped system, their relations to transport properties, and the physical basis for a saturation of physical properties at P* in the full class of manganites.

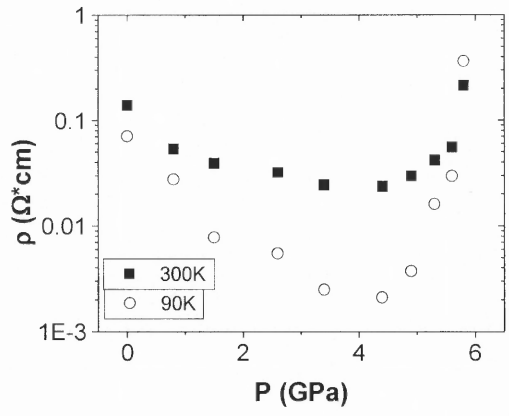

Figure 4.9 Pressure dependence of resistivity at low temperature 90K and high temperature 300K.

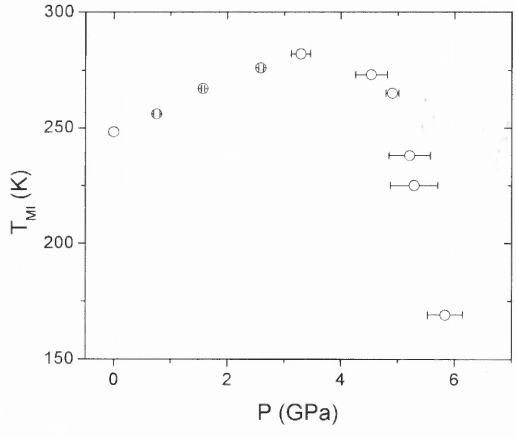

Figure 4.10 Pressure dependence of T_{MI} for $La_{0.85}MnO_3$.

Below P*, the transition temperature T_{MI} increases linearly with the pressures at the rate of 10.1±0.4K/GPa and the resistivity near room temperature decreases with the pressures. This result agrees with most of earlier investigations of pressure dependent

resistivity for mixed valance perovskite samples such as $La_{1-x}Ca_xMnO_3$ ($0.2<x<0.4$)[48, 49] for pressures below 2GPa. However, above ~3.4 GPa, T_{MI} is found to decrease sharply with increasing pressure at the rate of approximately -74.0±8.0K/GPa. The pressure dependence of T_{MI} is given in Figure 4.10.

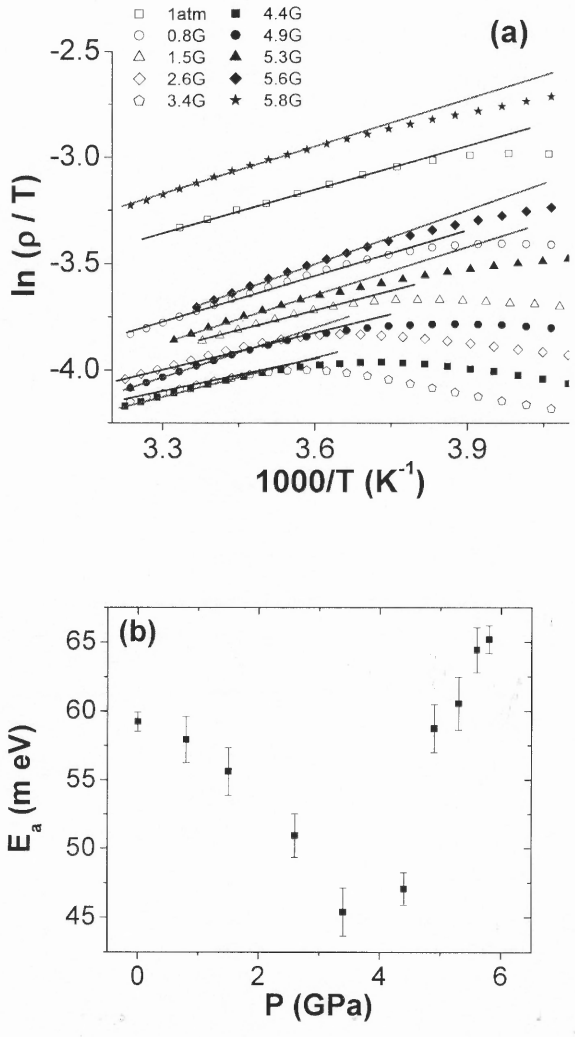

Figure 4.11 (a) The temperature dependence of resistivity at various hydrostatic pressures with linear fitts above T_{MI}, (b) the pressure dependence of activation energy E_a.

At ambient pressure, we find T_C and T_{MI} coincide with each other. A similar result for $La_{0.67}Ca_{0.33}MnO_3$ shows the coincidence of T_C and T_{MI} up to at least 1.6 GPa[48].

However, due to the difficulty in high-pressure magnetization measurements above 2GPa, the pressure dependence of T_C will be left to future work.

Figure 4.10 also shows that the pressure error bars increase with pressures especially above P*, which may imply that the liquid medium freezes to lead a pressure gradient at higher pressure. Several small ruby chips around the sample show variations of pressure less than 0.5GPa, and the fluorescence doublet still separate quite clearly, both of which may verify that the sample chamber maintains quasi-hydrostatic in the pressure range up to ~6 GPa.

Above T_{MI}, in the insulating phase the electrical resistivity ρ is due to charge-carrier hopping with activation energy E_a. Figure 4.11 (a) shows the $\ln(\rho/T)$ vs $1000/T$ using the expression $\rho = \rho_o T \exp(E_a/kT)$. As seen in Figure 4.11 (b), the activation barrier E_a has a minimum value at P*, which also verify the existence of the non-linear pressure effect on electron transport for this self-doped system $La_{1-x}MnO_3$.

4.1.7 Structure under Pressure

To reveal the non-linear pressure effects on electron transport, we conducted high-pressure x-ray diffraction measurements to study the pressure effects on crystalline structure.

Figure 4.12 displays representative x-ray diffraction patterns over the pressure range ambient up to ~ 7 GPa at room temperature. Higher pressure structural analysis revealed that no phase transition is observed up to 11 GPa. At ambient-pressure, the lattice parameters for space group I2/a are a= 7.8012 (13) Å, b= 5.5265 (1) Å, c= 5.4818 (1) Å, β= 90.828(7) °. The residual amplitudes in the worst case (weak peaks) are smaller than 1/8 of the corresponding peak intensities in Figure 4.12 (b). The accuracy of the data was assessed by comparison of ambient measurements in the diamond cell with synchrotron

beam and standard bulk measurements with a laboratory x-ray diffractometer (Rigaku RINT2100). The analyzed structure parameters are fully consistent in three independent sets of measurements (Table 4.2).

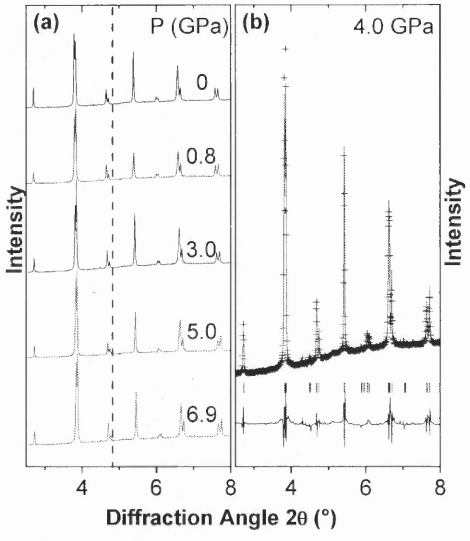

Figure 4.12 (a) The synchrotron x-ray powder diffraction patterns at various pressures up to 6.9 GPa, at room temperature, with a vertical dotted line as a guide to the eyes. (b) Diffraction pattern (crosses) at the 4.0 GPa with its Rietveld fit (solid) and residual (lower line).

Table 4.2 Lattice Parameters of $La_{0.85}MnO_3$ at the Ambient Condition from Different Measurements.

	Synchrotron X-ray	Standard X-ray	Data of Reference[80]
a (Å)	7.8012(13)	7.7943(1)	7.790(1)
b (Å)	5.5265(1)	5.5286(2)	5.526(1)
c (Å)	5.4818(1)	5.4835(6)	5.479(1)
β (deg)	90.828(6)	90.814(4)	90.78

The high-pressure synchrotron x-ray diffraction data were refined by Rietveld method based on the parameters of conventional XRD at ambient pressure. Table 4.3 and Table 4.4 present the detailed structural and lattice parameters under the selected hydrostatic pressures for $La_{0.85}MnO_3$.

Table 4.3 Structural and Lattice Parameters at Various Hydrostatic Pressures for $La_{0.85}MnO_3$ at Room Temperature.

$La_{0.85}MnO_3$ Pressure (GPa)	1 atm	0.82	2.24	3.05	4.08	4.98	6.91
Space Group	I 2/a	I 2/a	I 2/a	I 2/a	I 2/a	I 2/a	I 2/a
La (4e) (1/4 y 0)							
y	0.501(2)	0.501(3)	0.507(3)	0.500(5)	0.501(4)	0.502(4)	0.502(1)
Mn (4a) (0 0 0)							
O(1) (4e) (1/4 y 0)							
y	0.011(6)	-0.024(3)	0.013(3)	-0.028(5)	-0.062(4)	-0.031(7)	0.0051(8)
O(2) (8f) (x y z)							
x	-0.013(1)	-0.017(7)	-0.011(1)	-0.023(1)	-0.027(2)	-0.115(16)	-0.026(4)
y	0.167(7)	0.215(1)	0.185(1)	0.203(5)	0.205(2)	0.198(2)	0.199(1)
z	0.336(3)	0.337(7)	0.333(1)	0.314(1)	0.324(4)	0.331(3)	0.350(4)
B_{La} (Å^2)	0.55(2)	4.85(52)	1.89(6)	1.22(9)	1.36(4)	3.73(2)	2.81(7)
B_{Mn} (Å^2)	0.80(5)	3.15(48)	1.57(2)	1.46(1)	0.19(3)	0.04(1)	1.76(1)
B_O (Å^2)	0.6	0.6	0.6	0.6	0.6	0.6	0.6
a	7.8012(13)	7.772(0)	7.7629(2)	7.7618(12)	7.7385(4)	7.7259(1)	7.7022(2)
b	5.5265(1)	5.513(6)	5.4981(1)	5.4911(5)	5.4876(0)	5.4770(1)	5.4548(1)
c	5.4818(1)	5.472(5)	5.4573(2)	5.4586(5)	5.4493(1)	5.4180(1)	5.4080(1)
β	90.828(6)	90.884(4)	90.911(5)	90.921(6)	90.920(2)	90.738(1)	90.869(1)
R_p	1.673	2.111	1.551	1.791	1.662	1.817	1.738
R_{wp}	2.951	3.829	2.804	3.497	2.856	2.995	2.869
χ^2	0.044	0.076	0.045	0.078	0.045	0.045	0.048

In Figure 4.13, we show the pressure dependence of the lattice parameters and the unit-cell volume. The linear compressibility of all three lattice parameters have similar value db/dP=0.0092(6) Å/GPa and K_b=0.00166 GPa^{-1}. Note the changes of slope in the lattice parameters near ~3.4 GPa. Attempts to fit an equation of state for the two regions P < P* and P > P*, resulted in significant uncertainty in the parameters (B_0 and B') because of the limited range of the pressure data (ambient to ~3.4 GPa and ~3.4 to 7 GPa). While data can be acquired for the second region by extending the measurements up to higher pressures, the lower range will be difficult to fit. We also fit the entire pressure range

from ambient to 7 GPa and show the results in Fig. B below. The parameters with errors are shown in Table 4.5. Again, there is a large uncertainty in B' and significant deviations of the data points from the fit near P* (~3.4 GPa). Higher order equations of state produce the same result. The lattice parameters shown in Fig. B part (b) also reveal a kink at the critical pressure. This suggests that two distinct equations of state exist.

Table 4.4 Selected Bond Distances and Angles versus Pressures for $La_{0.85}MnO_3$ Calculated from the Parameters Shown in Table 4.3.

$La_{0.85}MnO_3$							
Pressure (GPa)	1atm	0.82	2.24	3.05	4.08	4.98	6.91
Space Group	I 2/a	I 2/a	I 2/a	I 2/a	I 2/a	I 2/a	I 2/a
$d_{Mn\text{-}O(1)}$ (×12)	1.952(2)	1.950(4)	1.946(2)	1.964(6)	1.965(4)	1.939(4)	1.926(2)
$d_{Mn\text{-}O(2)}$ (× 8)	2.084(14)	2.077(16)	2.085(2)	2.053(2)	2.109(18)	2.115(18)	2.196(22)
$d_{O(2)\text{-}Mn}$ (× 8)	2.032(14)	1.967(9)	1.958(6)	1.928(20)	1.889(18)	1.908(16)	1.839(8)
Mn-O(1)-Mn (× 6)	176.1(20)	171.54(2)	171.1(22)	162.1(10)	159.9(12)	169.8(24)	178.3(2)
Mn-O(2)-Mn (× 8)	142.0(12)	147.0(6)	146.7(6)	152.8(8)	150.5(6)	146.4(6)	144.1(14)

The unit-cell volume fit by using the first order Birch-Murnaghan equation of state (Equation 4.1) is shown as the solid line Figure 4.13 (b). Note that significant deviation of the points from the line particularly also near P* in Figure 4.13 (b) and remarkable fitting errors shown in Table 4.5, both of which suggests that a single equation of state does not adequately describe the pressure dependence.

$$V(P) = V_0(1 + B'\frac{P}{B_0})^{-1/B'} \qquad \textbf{(4.1)}$$

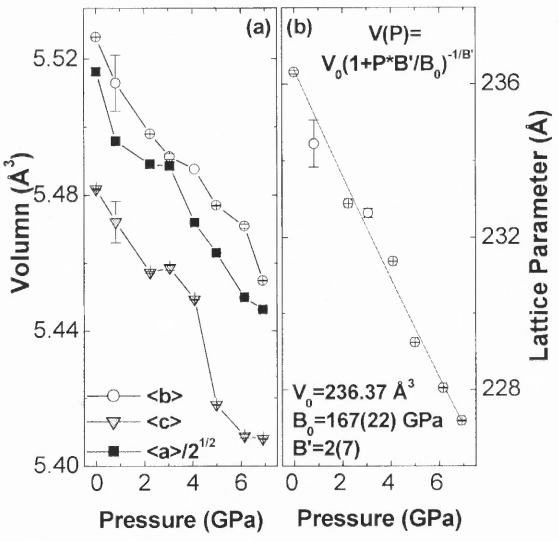

Figure 4.13 (a) Lattice parameters of $La_{0.85}MnO_3$ at the ambient temperature as a function of pressure. (b) Unit-cell volume versus pressure up to 7 GPa with a curve depicting the first order Birch-Murnaghan fit for equation of state.

Table 4.5 First Order Murnaghan Fit.

Parameter	Value	Error
V_0	236.37	0 (fixed)
B'	2.00108	7.88117
B_0	167.25987	22.04927

We calculated the out-of-plane bandwidth W_1 (along *a* axis) and in-plane (in *b-c* plane) bandwidth W_2 (two bonds) by using the corresponding angles $<\theta_{Mn\text{-}O1\text{-}Mn}>$ and $<\theta_{Mn\text{-}O2\text{-}Mn}>$, with the empirical expression[47]:

$$W_x \propto \frac{\cos(\frac{1}{2}(180° - <\theta_{Mn-Ox-Mn}>))}{d_{Mn-O}^{3.5}} \qquad (4.2)$$

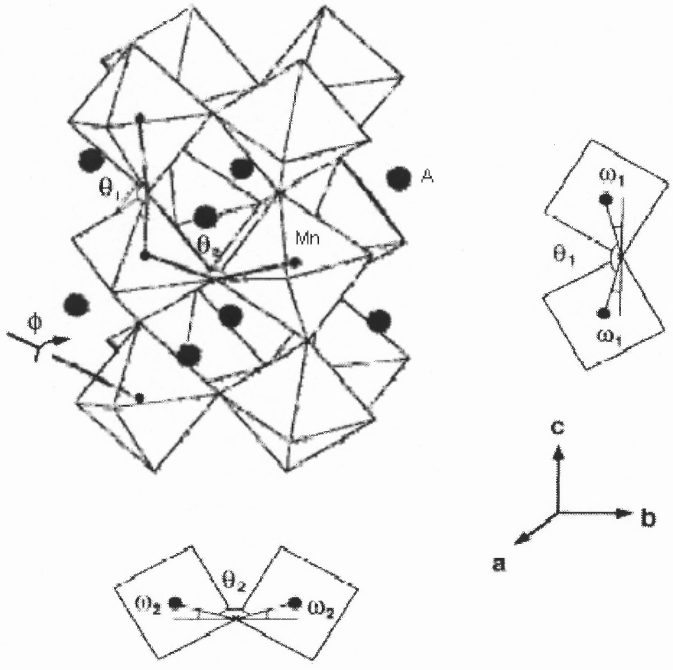

Figure 4.14 The tilting angles (ω_1 and ω_2) and bond angles (θ_1 and θ_2), in which the subscripts 1 and 2 represent the out-of-plane (along *c* axis) angles and in-plane (*ab* plane) angles, respectively.

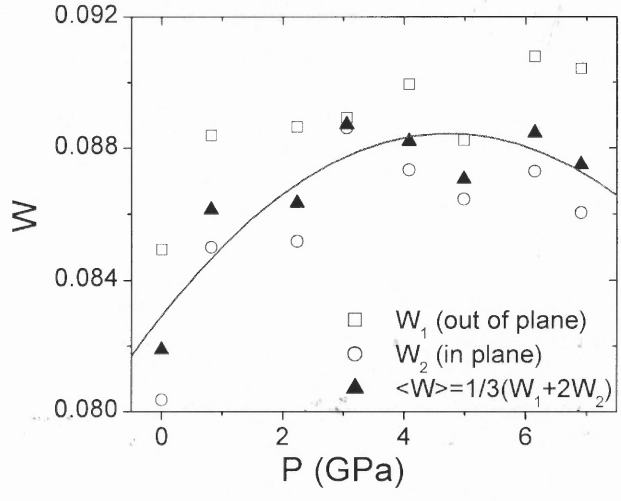

Figure 4.15 Pressure dependence of bandwidth for $La_{0.85}MnO_3$. The red line is just a guide to the eyes.

Figure 4.14 shows the definition of the tilting angles ω and the buckling angles θ between MnO_6 octahedra. Where the subscript x can be 1 or 2 corresponding to the apical and in-plane situations, respectively, and d_{Mn-O} is the average bond distance over all bonds. The average bandwidth <W> is obtained by the relation $<W>=1/3(W_1 + 2\ W_2)$.

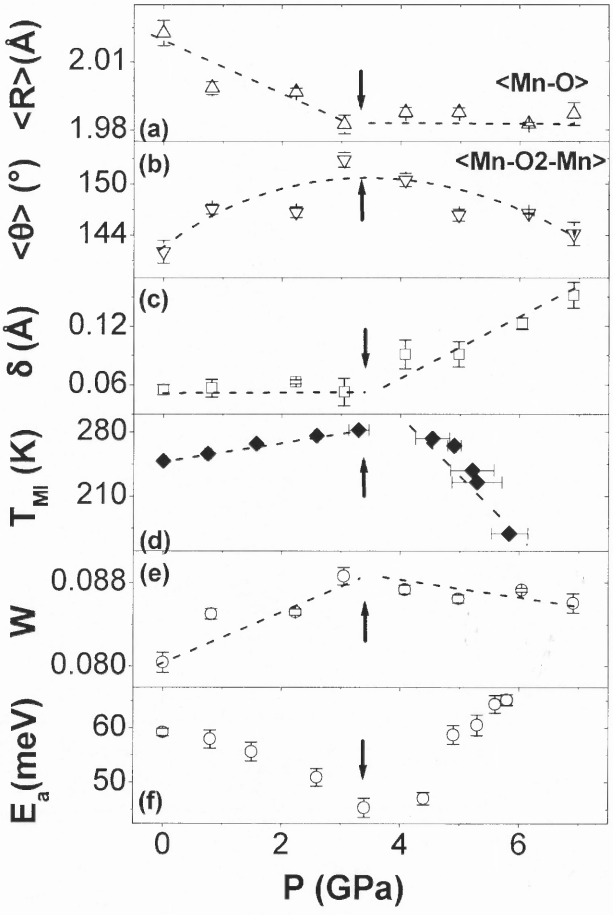

Figure 4.16 Pressure dependence of structural and electronic parameters. The average Mn-O distance (a), average Mn-O2-Mn bond angle (b), the MnO_6 octahedral distortion (c), the metal-insulator transition temperature T_{MI} (d), the electron bandwidth W with arbitrary units, (e) and activation energy E_a for charge-carrier hopping above T_{MI} (f), are plotted as a function of pressure.

The pressure dependence of all components is shown in Figure 4.15, which reveals that the in-plane bandwidth W_2 has the largest pressure dependence. This contribution dominates the bandwidth variation and was plotted in Fig. 4.16 (e). Note that in this system the bond angle $\theta_{Mn\text{-}O1\text{-}Mn}$ is close to 180° and $\theta_{Mn\text{-}O2\text{-}Mn}$ is in the range of $142° < \theta < 155°$. Hence the expressions $\cos(1/2(180°\text{-}\theta))$ and $\cos(180°\text{-}\theta)$ used in the literature yield the same functional form. Note that θ is the measured Mn-O-Mn bond angle.

By Rietveld refinements of the XRD data, the pressure dependence of the structures was obtained. Figure 4.16 shows the pressure dependence of the average bond distance of $<d_{Mn\text{-}O}>$ (a), the bond angle of $<\theta_{Mn\text{-}O2\text{-}Mn}>$ in the b-c plane (b), the MnO_6 octahedral distortion $\delta = \sqrt{\frac{1}{6}\sum(d_{Mn\text{-}O} - < d_{Mn\text{-}O} >)^2}$ (c), T_{MI} (d), the charge-carrier bandwidth W (e), and the activation energy E_a (taken from fits to the resistivity above T_{MI}) (f) based on $\rho = \rho_0 T \exp(E_a/kT)$[109].

In the observed pressure range, the average tilt angles of MnO_6 octahedra do not change significantly. However, the average Mn-O bond distance contracts monotonically below the critical pressure P* and maintains a constant value above P*. In the framework of the double-exchange model, the magnetic and transport properties are determined by the charge-carrier bandwidth W, which depends on the Mn-O bond distance and the Mn-O-Mn bond angle through the overlap integral between Mn 3d orbital via O 2p orbital. In our work, we have used an approximate expression, $W \propto \cos(1/2(\pi - < \theta_{Mn\text{-}O\text{-}Mn} >)) / d_{Mn\text{-}O}^{3.5}$, based on the radial[47] and the angular dependence (Mn-O-Mn) of the overlap matrix[21, 46], as shown in Figure 4.16 (e). Note that the bandwidth increases below P*, however, it decreases very slowly above P*. The MnO_6 octahedral distortions were found to be

constant at the low-pressure range but suddenly increase at higher pressures (Figure 4.16 (c)).

These results show that, below P*, the increase in T_{MI} with pressure is due to the increase in the electron bandwidth, which reaches its maximum at P*. Moreover increases in pressure yield enhance local distortions, which trap the e_g conduction electrons and produce an insulating phase. This can be further seen from the enhancement of the resistivity for pressure above P*. In fact, the increase of the resistivity seen at low temperature is reminiscent of percolation, which occurs through the introduction of an insulating phase into a metallic phase[110]. The activation energy E_a for hopping (in the high-temperature region) exhibits a minimum at P*, which is consistent with the maximum of the bandwidth.

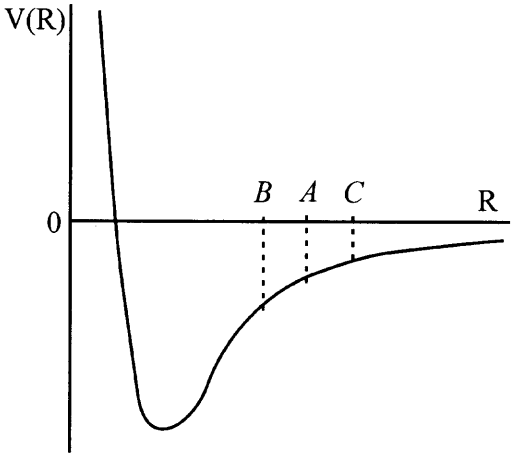

Figure 4.17 Schematic drawing of the interatomic potential between the rare earth and the oxygen ions. *A* marks the RE-O distance before Mn-O-Mn buckling in perovskite manganites with a tolerance factor less than 1. *B* and *C* mark the two different RE-O distances after Mn-O-Mn buckling.

To explain our data below *P**, we consider a typical inter-atomic potential, *V(r)*, between the RE and the oxygen (O) ion in perovskite manganites, for example, a potential

energy curve similar to the Lennard-Jones potential with a strong repulsive core and a weakly attractive tail. In $RE_{1-x}A_xMnO_3$ perovskites when the tolerance factor ($t = \frac{(< R_A > + R_O)}{\sqrt{2}(R_{Mn} + R_O)}$ and R_i are the atomic radii) is less than 1, the distance between RE/A and O before Mn-O-Mn buckling, r_0 (position A shown in Figure 4.17), would be larger than the distance with the minimum potential energy. Buckling of a Mn-O-Mn bond moves an O ion closer to the RE on one side and farther apart from the RE on the other side, which gives rise to two different RE-O distances. The buckling would occur only if the net energy decreases upon buckling, in other words, $d^2V(r)/dr^2|_{r=r0} < 0$. If the RE-O potential is purely harmonic, the buckling of Mn-O-Mn bonds would not occur. It is the anharmonicity of the potential energy that reduces the total potential energy upon buckling. The effect of external pressure is to move the point r_0 closer to the harmonic region of the potential (more precisely, to the inflection point of the potential), which reduces the energy gain associated with buckling and, therefore, buckling itself as observed below P^* in our data. Such straightening of the Mn-O-Mn bond angles as well as the reduced volume under pressure contribute to the rapid decrease of the average Mn-O distance, as observed for pressure below P^*. Both effects associated with the Mn-O-Mn bond angle and the Mn-O distance add up to increase the effective hopping amplitude of the e_g electrons on Mn sites, which explains the increase of W and T_{MI} below P^*.

We now examine possible explanations for our data at pressures above P^*. Once the Mn-O distance is reduced into the region of a hard-core potential, the Mn-O distance is very hard to compress any further by external pressure. We believe that P^* marks such critical pressure. Above P^*, the average Mn-O distance remains almost constant as shown

in our data. The only way to reduce the Mn-Mn distance and, therefore, the volume of the unit cell by applied pressure is to buckle Mn-O-Mn bonds, which explains the observed increase of the buckling (i.e. reduced Mn-O-Mn angle) above P^*. Our data also shows the rapid increase of the Jahn-Teller distortion above P^*. The Jahn-Teller coupling can be considered in terms of hybridization between Mn e_g orbitals and oxygen p orbitals, which increases for a shorter average Mn-O distance. Therefore, the Jahn-Teller coupling would be enhanced for smaller average Mn-O distances. The appearance of the strong Jahn-Teller distortion only above P^* not below P^*, in spite of similar Mn-O-Mn buckling, demonstrates the importance of the average Mn-O distance on the strength of the Jahn-Teller coupling. The rapid decrease of T_{MI} above P^* is consistent with the reduced electron mobility due to the increased buckling and the Jahn-Teller distortion.

4.2 High Pressure Effects on Electron Transport and Structure of $La_{0.75}MnO_3$

A polycrystalline sample of $La_{0.75}MnO_3$ was also produced by solid state reaction methods with the appropriate ratio of reagents of La_2O_3 and Mn_2O_3. The sample cation ratio was determined by ICP (Inductively Coupled Plasma) method (by QTI corp.) and was found to a ration La/Mn of 0.749.

4.2.1 Electronic Transport under Pressure

In this self-doped sample, at the ambient pressure T_{MI}=239.0 ± 1.0K coincides with its Curie temperate T_C. Hence below T_{MI} the sample is a ferromagnetic metal.

High pressure resistivity measurements reveal that this sample also has a critical pressure P* of ~ 4.2 GPa, which is a little higher than $La_{0.85}MnO_3$. Figure 4.18 gives the resistivity at different pressures. Below P*, T_{MI} increases linearly with pressure while its

resistivity decreases. This implies that the compound becomes more metallic. Above P*, the reversal trends for both T_{MI} and resistivity reveal a transition to more insulating phase.

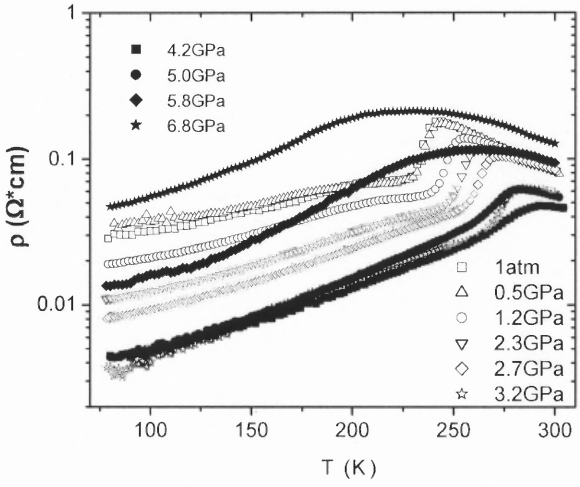

Figure 4.18 Temperature dependence of resistivity under various pressures for $La_{0.75}MnO_3$.

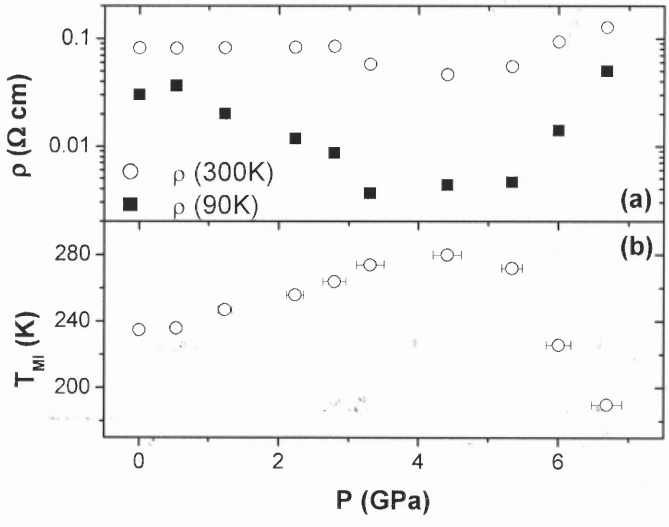

Figure 4.19 Pressure dependence of (a) resistivity at low-temperature T=90K and high-temperature T=300K, (b) Metal-Insulator transition temperature.

Due to more vacancies in the La site, sample $La_{0.75}MnO_3$ presents higher resistivity and smaller T_{MI} values than those of $La_{0.85}MnO_3$ within the measured pressure range. More electrons scattering by vacancies result in higher resistivity. The degree of disorder in this system can be studied by synchrotron X-ray diffraction under pressures. More vacancy sites leave more space to be compressed to the region of hard-core potential, which may cause a higher critical pressure. In figure 4.19, resistivity curves of this sample show a more flatten refraction, and the shifts in T_{MI} are over a smaller range. This may also be explained by DE theory and Jahn-Teller distortion: below P*, the carrier bandwidth increases due to the compression of Mn-O bond length and increasing of Mn-O-Mn bond angle, which implies that the high-temperature insulator state is suppressed by pressure, hence, the system becomes more metallic. Above P*, because the atoms are compressed to the hard-core region, the bond lengths are difficult to be shorten. Jahn-Teller distortion may dominate the enhancement of insulating state. The local distortion induces higher electronic resistivity due to the formation of potential wells in crystal structures. So above the critical pressure, this system also presents a reversal of trend compared with low-pressure range.

4.2.2 Structures under Pressure

To study relations between structure and physical properties under pressure, high-pressure synchrotron x-ray measurements were performed at Beamline X17C of Brookhaven National Laboratory. The x-ray wavelength was 0.4066Å corresponding to beam energy of 30 keV. The distance from sample to detector was about 25 cm. To obtain more diffraction rings, this beamline uses the off-center CCD to collect data shown as Figure 4.20 (a). Then we chose a wedge region (Figure 4.20 (b)) starting from beam center to integrate and then

obtain the one-dimension diffraction pattern. The CeO_2 polycrystalline powder has been used for the calibration of this measurement. From the photos, some over-exposed points can be seen. To avoid that, we scanned a series of short-time exposure and then summed them and some masks (small red polygons) were also used to reduce the signal from these "hot spots" shown as Figure 4.20 (b).

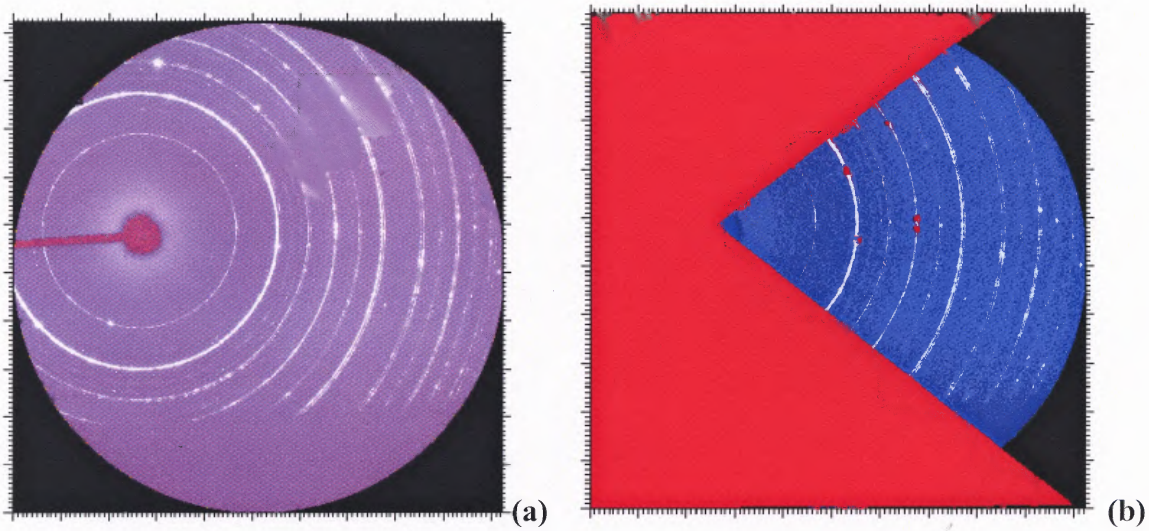

Figure 4.20 (a) X-ray diffraction rings of $La_{0.75}MnO_3$ at ambient pressure, (b) The masked diffraction rings (all regions in red are excluded for integration).

The synchrotron x-ray diffraction pattern at ambient pressure and room temperature showed that the self-doped samples $La_{0.75}MnO_3$ are in a single crystallographic phase. Over the pressure range from ambient up to 10GPa, the structure was refined to monoclinic symmetry and I2/a space group same as $La_{0.85}MnO_3$ using the Rietveld method.

In Figure 4.22, only shifts of diffraction peaks can be obviously seen but no peaks appear or disappear, which may show that this sample maintains monoclinic I 2/a symmetry up to the pressure ~9.4 GPa without a structural phase transition.

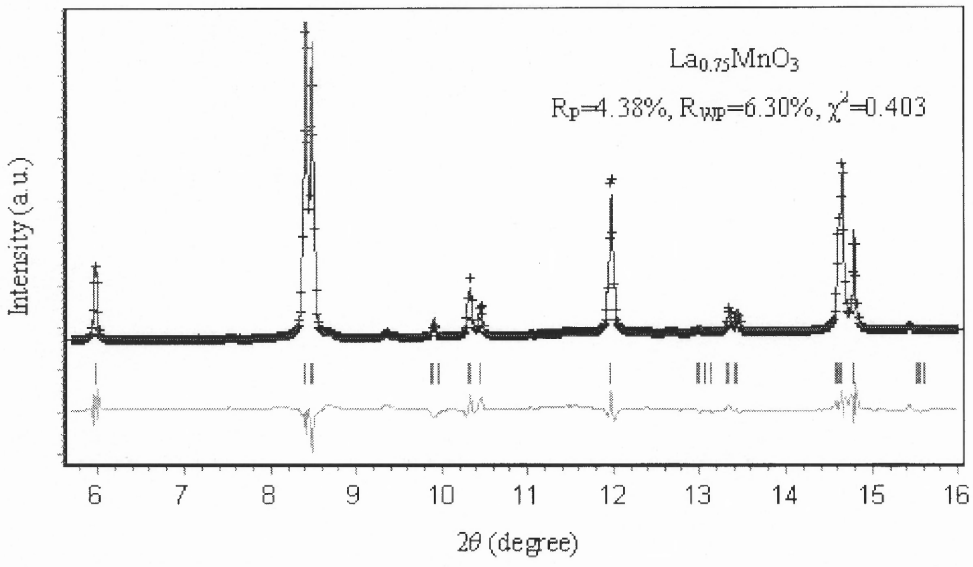

Figure 4.21 The synchrotron x-ray diffraction data (crosses) at ambient pressure with its Rietveld refinement (solid) and residual (lower line).

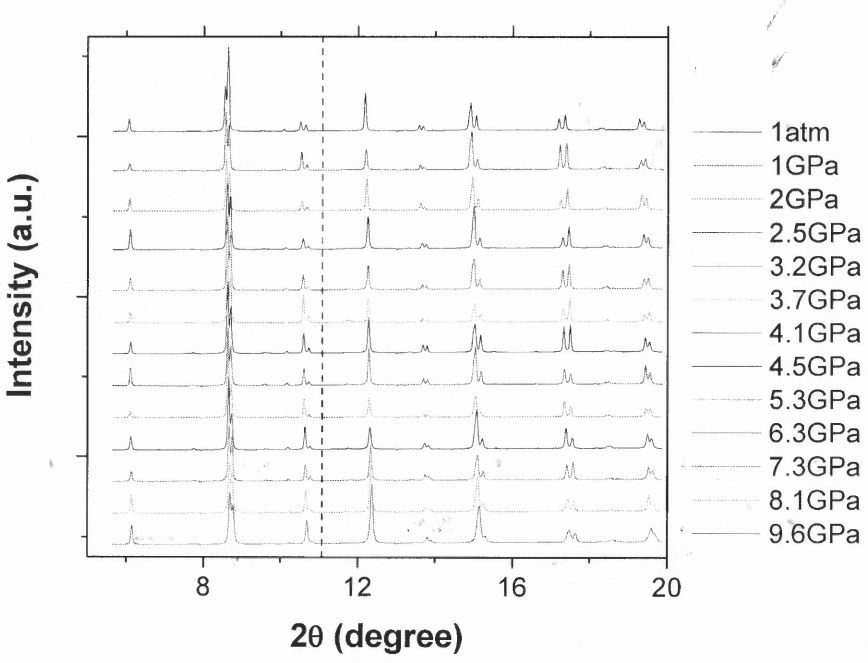

Figure 4.22 Synchrotron x-ray diffraction patterns at various pressures.

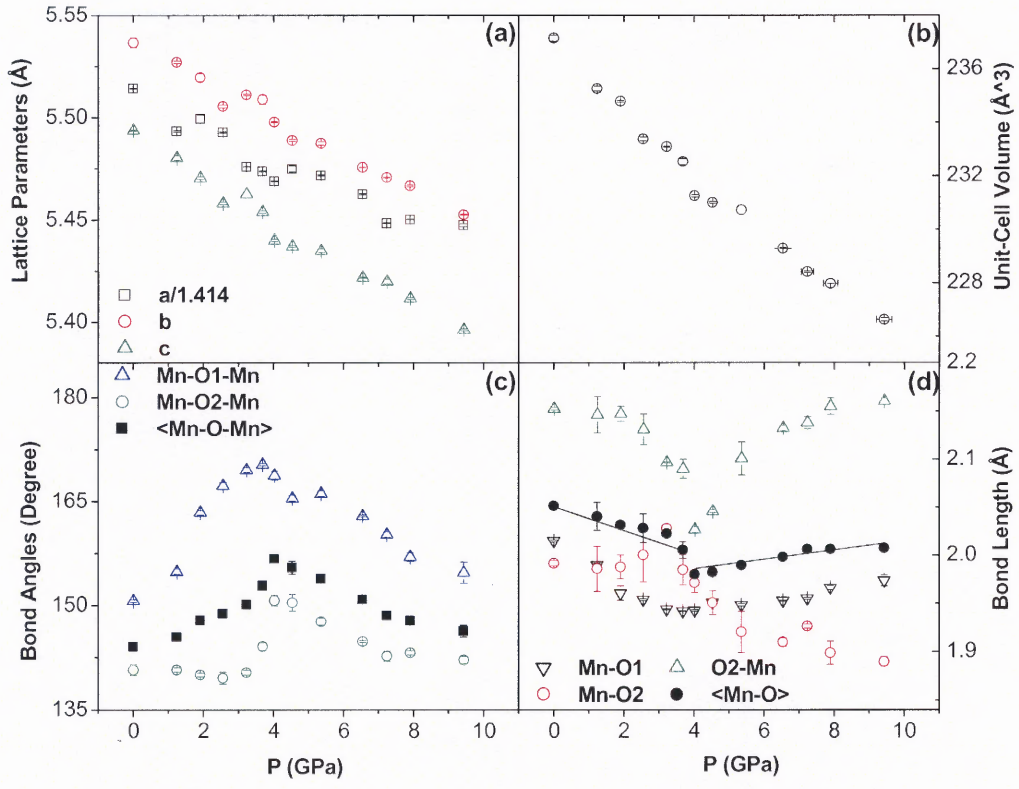

Figure 4.23 Pressure dependence of (a) Lattice Parameters, (b) Unit-Cell Volume, (c) Mn-O-Mn Bond Angles, and (d) Mn-O Bond Length for $La_{0.75}MnO_3$.

In Figure 4.23 (a), by linearly fitting the lattice parameters, their similar compressing rate around $d\langle a\rangle/dP$=-0.0101(5) Å/GPa is found to have a little larger absolute value than that of $La_{0.85}MnO_3$ $d\langle a\rangle/dP$=-0.0096(7) Å/GPa. Due to the less occupation of La site, the crystalline structure of $La_{0.75}MnO_3$ has more vacancies to accommodate compression than $La_{0.85}MnO_3$. In-plane bond angles (<Mn-O1-Mn>) and out-of-plane bond angles (<Mn-O2-Mn>) show similar pressure dependence with the maximum angles at ~4 GPa. In Figure 4.23 (d), a larger distortion of octahedral has also been found at the ambient pressures due to the higher La vacancy level of $La_{0.75}MnO_3$. The unit-cell volume fit by using the first order Birch-Murnaghan equation of state (equation

4.1) is shown as the solid line Figure 4.24. Also the prominent uncertainties for both B' and B_0 (in the *insert* of Fig, 4.24) suggest that a single equation of state does not adequately describe the pressure dependence, which provide further evidence on the existence of the critical pressure for this series of CMR materials La_xMnO_3.

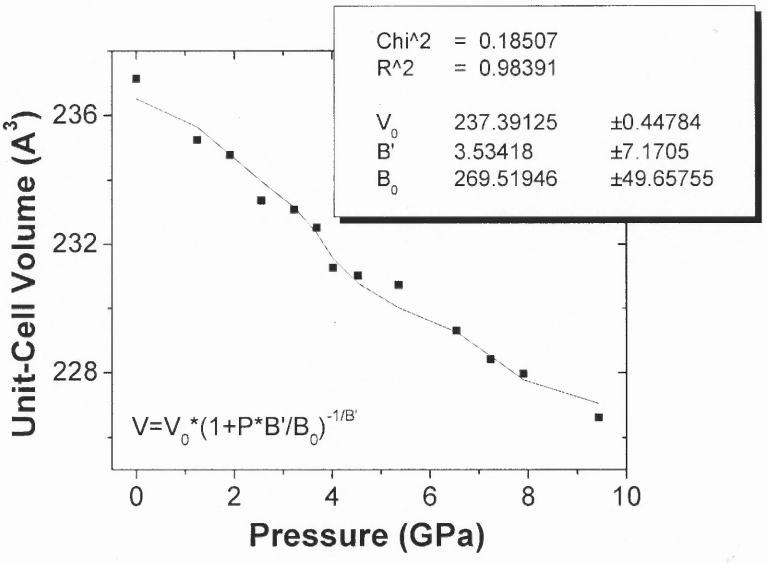

Figure 4.24 Pressure dependence of Unit-Cell Volume with a curve depicting the Birch-Murnaghan fit for equation of state.

To further understand the nonlinear pressure effects of $La_{0.75}MnO_3$ self-doped sample, the pressure dependence of all significant parameters were plot together in Figure 4.25. All parameters verified the existence of the critical pressure P*. Below P*, the carrier bandwidth W results in the increasing of T_{MI}, which means the sample becomes more metallic. However, above P*, much larger octahedral distortions become the important factor to decrease T_{MI}, which means that the stronger electron-lattice coupling can trap more carriers to result in a more insulating status.

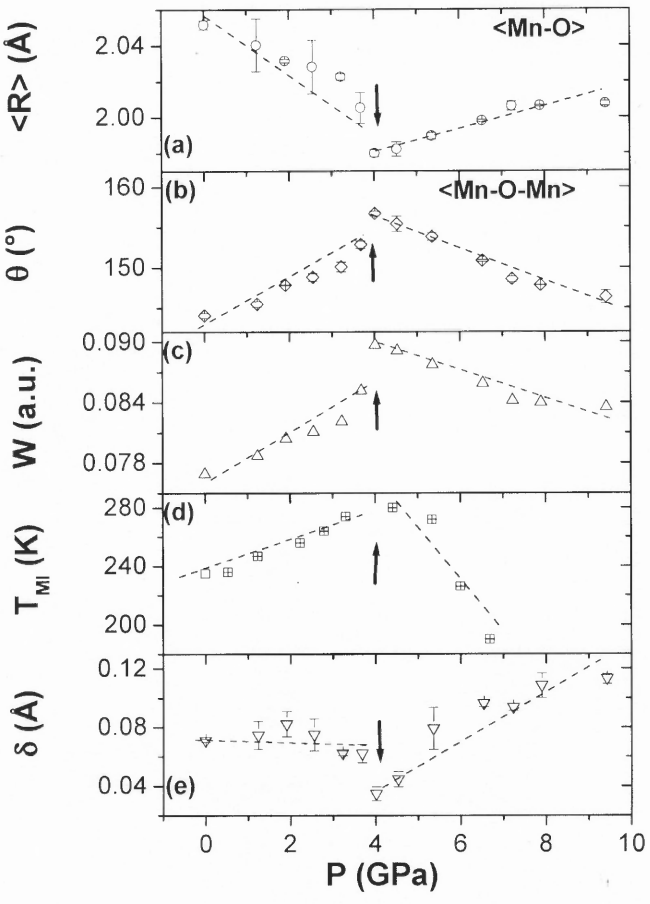

Figure 4.25 Pressure dependence of structural and electronic parameters. The average Mn-O distance (a), average Mn-O-Mn bond angle (b), the electron bandwidth W (c), the metal-insulator transition temperature T_{MI} (d), and the MnO_6 octahedral distortion (e), are plotted as a function of pressure.

In another way, compared with $La_{0.85}MnO_3$, we found that more vacancies at the La site in $La_{0.75}MnO_3$ tolerate larger local distortions. At the lower pressure range the distortions can be suppressed, and then be enhanced above P*.

4.2.3 Magnetization Measurement

Figure 4.26 shows that both the sample magnetization and T_C are enhanced by magnetic fields. The low-temperature magnetization (from $3.14\mu_B$/Mn at H=0.5T to $3.26\mu_B$/Mn at

H=4.5T) approaches the theoretical value of 3.25μ_B/Mn. The Curie temperature, T_C, increases with the rate of 4.81±0.44K/T shown in the insert of figure 4.26.

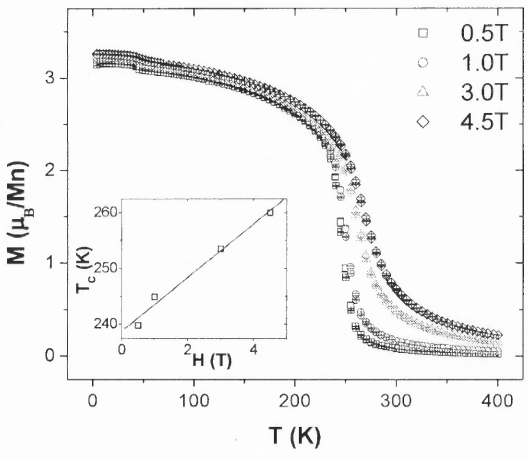

Figure 4.26 Magnetization versus temperature at different magnetic fields and magnetic field dependence on T_C (insert).

4.2.4 Magnetoresistivity Measurement

For $La_{0.75}MnO_3$, magnetic fields strongly enhance the electronic transport to produce a very large negative magnetoresistance as in $La_{0.85}MnO_3$. Both samples show typical CMR properties.

Figure 4.27 shows the resistivity curves of $La_{0.75}MnO_3$ at various magnetic fields up to 7.5T. We observed the sample resistivity was significantly reduced by the applied fields. And the *insert* of Figure 4.27 presents that the magnetic field enhances T_{MI} with a rate of dT_{MI}/dH =5.27±0.28K/T.

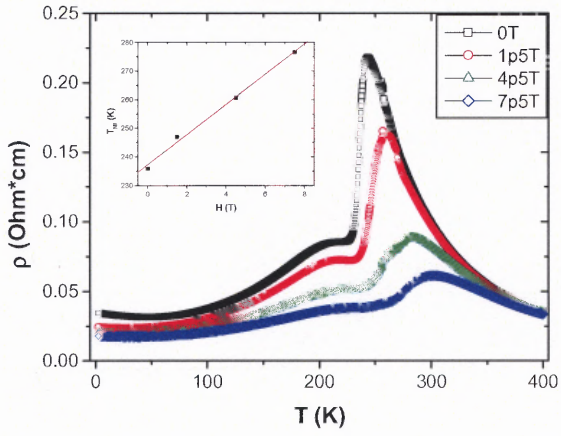

Figure 4.27 Magnetoresistance at various magnetic fields and magnetic field dependence of T_{MI} (*insert*).

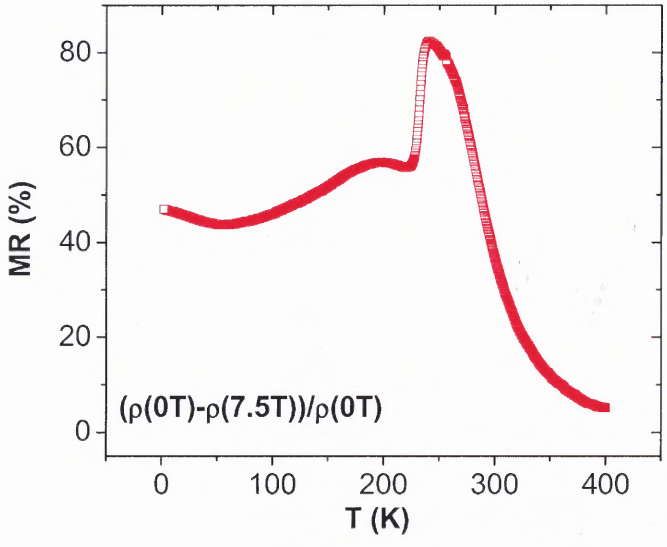

Figure 4.28 Magnetoresistance for the magnetic field of 7.5T.

Figure 4.28 reveals that $La_{0.75}MnO_3$ has a high magnetoresistance about 80% at ~252K. Figure 4.29 shows that T_{MI} and T_C coincide at ~252.0K similar to $La_{0.85}MnO_3$ sample. Compared with magnetic field effect on T_C shown in Figure 4.25, it is obvious that

T_{MI} and T_C coincide for various fields at ambient pressure. Upon cooling, this sample shows a phase transition from paramagnetic insulator to ferromagnetic metal.

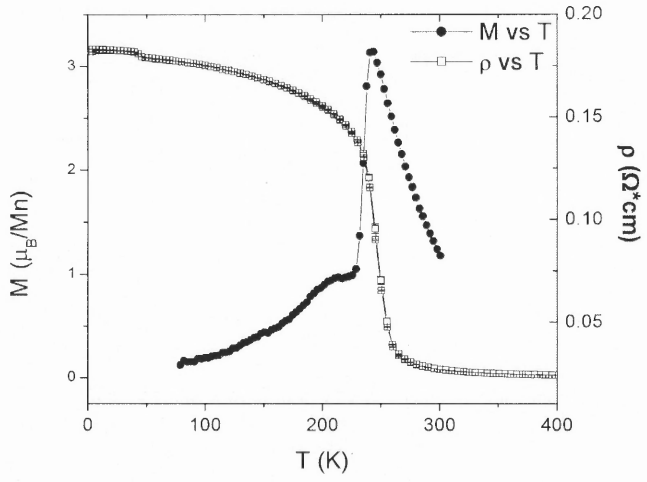

Figure 4.29 Ambient pressure resistivity and magnetization (at H=0.5 T) as a function of temperature for $La_{0.75}MnO_3$.

4.2.5 Discussion and Summary

High-pressure resistivity and x-ray diffraction measurements have been performed on the self-doped system $La_xMnO_{3-\delta}$ (x=0.85 and 0.75). We find that the metal-insulator transition temperature (T_{MI}) increases with pressures up to a critical value, P* ~3.4-4.0GPa, beyond which T_{MI} decreases with increasing pressure. The analysis of pressure dependence on the Mn-O bond distances and Mn-O-Mn bond angles reveal a close correlation between structural distortions and transport properties. In particular, the bandwidth increase drives the increase of T_{MI} for pressures below P*. The reduction of T_{MI} at higher pressures is found to result from the Jahn-Teller distortions of the MnO_6 octahedra and the localization of 3d electrons. The general trend is expected to be a characteristic feature of manganites. We find the anharmonic interatomic potential plays an important role for the structural

an important role for the structural changes in Mn-O distances, Mn-O-Mn bond angles, and the Jahn-Teller distortions under pressures.

As further work, local structural measurements under pressure, temperature and magnetic field variations will be conducted to examine the nature of the defect structure and determine the local structural changes due to these external perturbations. Neutron diffraction measurements and magnetization/susceptibility measurements under pressure will be conducted to probe the magnetic order as a function of pressure.

4.3 High Pressure Effects on Electrical Transport and Structure of $La_{1-x}Ca_xMnO_3$

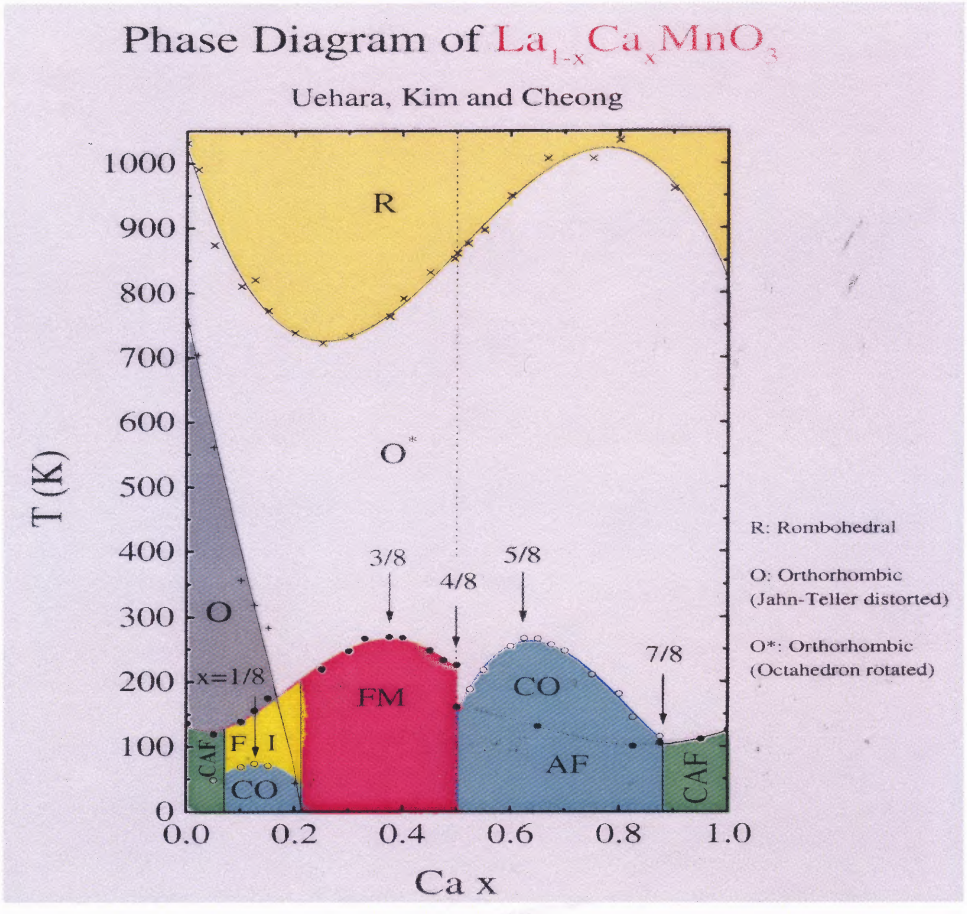

Figure 4.30 Phase diagram of $La_{1-x}Ca_xMnO_3$[111].

As the typical CMR perovskite manganite system, $La_{1-x}Ca_xMnO_3$ has been studied very well and the detailed phase diagram is shown in Figure 4.30. For the Ca-doping between ~0.2 and ~0.5, this perovskite manganite system shows a phase transition from paramagnetic insulator (PI) at high temperature to ferromagnetic metal (FM) at low temperature. Figure 4.31 shows that the Curie Temperature T_C coincides with the Metal-Insulator transition temperature T_{MI} at ~260.0K at ambient pressure for CMR manganite $La_{0.67}Ca_{0.33}MnO_3$.

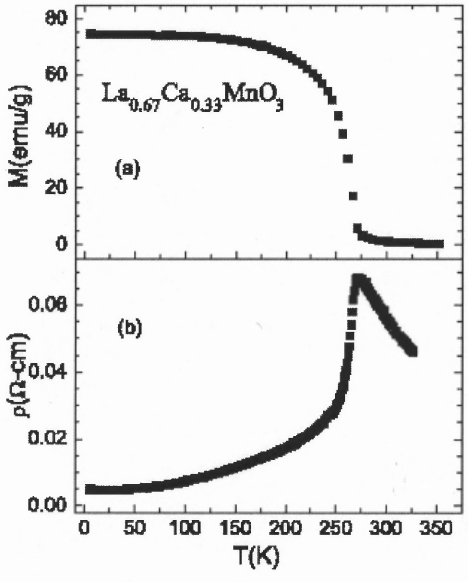

Figure 4.31 (a) Magnetization, (b) resistivity curves of $La_{0.67}Ca_{0.33}MnO_3$[38].

Even in this well-known system, most of research focused on the low pressure range below 2GPa, such as Moritomo[106] *et al*, Hwang[54] *et al* and Laukhin[49] *et al*. These experiments revealed a linear pressure dependence of T_C and T_{MI} at low-pressure range. To further understand the explanation presented in the previous sections and verify its universality for perovskite manganites, we conducted the same kinds of experiments on $La_{0.67}Ca_{0.33}MnO_3$ including high-pressure transport measurements, high-pressure synchrotron x-ray diffraction, and magnetization measurements.

The sample $La_{0.67}Ca_{0.33}MnO_3$ was synthesized by the solid state reaction method[112]. A mixture of stoichiometric reagents of La_2O_3, CaCO3, and MnO_2 was heated in air at 1250°C for 20h, at 1380°C for 20h, and at 1390°C for 20h with intermediate grindings. A final calcination, involving a 3-hour annealing at 1250°C with a cooling rate of 1°C/min was done to improve the uniformity of polycrystalline sample.

4.3.1 Electron Transport under Pressure

The resistivity of $La_{0.67}Ca_{0.33}MnO_3$ was measured by the four-probe methods under pressures up to ~6.0 GPa. Figure 4.32 shows the sample also has a critical pressure P* with a value of ~ 4GPa similar to the self-doped system. Below P*, pressure enhances the electrical conductivity and T_{MI} to induce a more metallic phase while it suppresses both of them to result in a more insulating phase above P*.

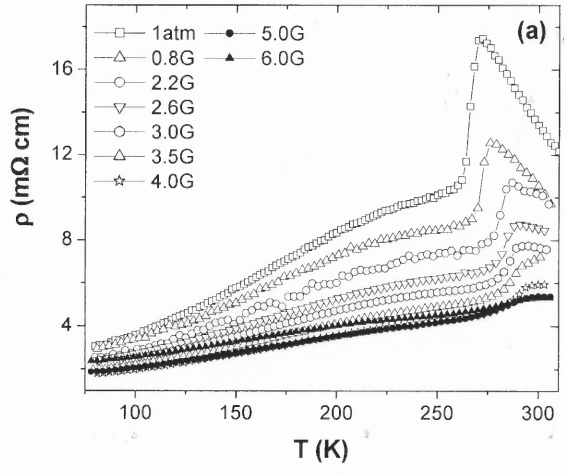

Figure 4.32 Electrical resistivity versus temperature at various hydrostatic pressures up to ~6.0 GPa for $La_{0.33}Ca_{0.67}MnO_3$.

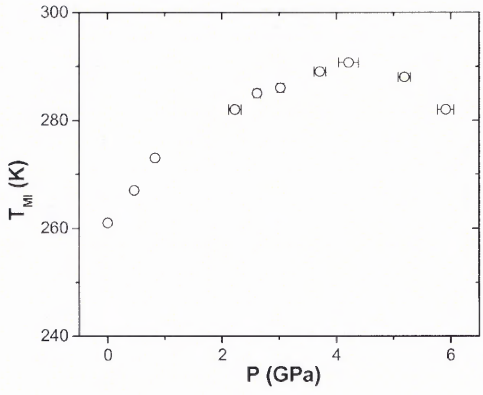

Figure 4.33 Pressure dependence of T_{MI} for $La_{0.67}Ca_{0.33}MnO_3$.

In $La_{0.67}Ca_{0.33}MnO_3$, the metal-insulator transition temperature T_{MI} is increased significantly from 260.0K to 290.7K with the pressure increase from 0 to 4.0 GPa and then decreased to ~280.1 K at 6.0 GPa above P*, shown in Figure 4.33.

4.3.2 Structure under Pressure

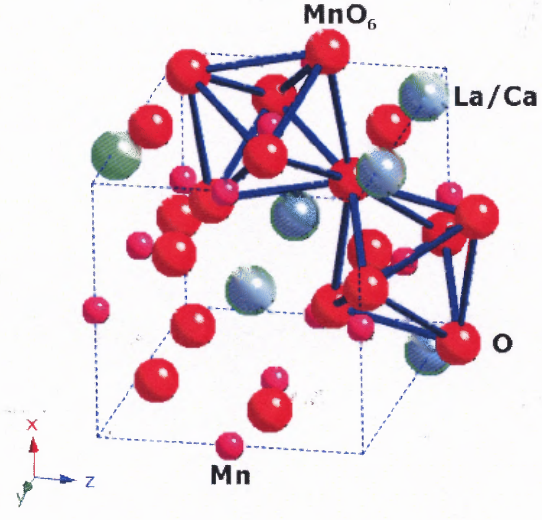

Figure 4.34 Crystalline structure of $La_{0.67}Ca_{0.33}MnO_3$ with Orthorhombic symmetry and Pnma space group (#62). Purple balls are Mn ions, red balls are O ions, green balls are La/Ca ions, and blue bars represent the O-O bonds of MnO_6 octahedra. The dash lines show the unit-cell.

To characterize the crystalline structure of $La_{0.67}Ca_{0.33}MnO_3$, both regular X-ray diffraction measurement by Rigaku (RINT 2100) and synchrotron X-ray diffraction have been conducted at the ambient condition.

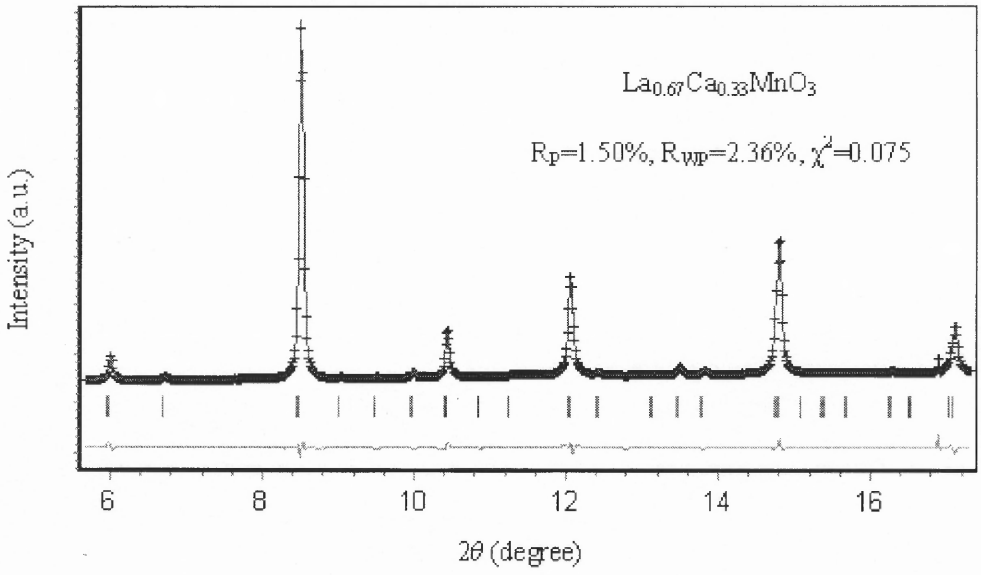

Figure 4.35 The synchrotron x-ray diffraction data (crosses) at ambient pressure with its Rietveld refinement (solid) and residual (lower line).

The synchrotron x-ray diffraction pattern at ambient condition showed that the polycrystalline samples $La_{0.67}Ca_{0.33}MnO_3$ are in a single crystallographic phase. The structure was refined to orthorhombic symmetry and Pnma space group (#62) by using Rietveld method.

The perovskite structure of unit-cell with MnO_6 octahedra have been shown in Figure 4.34, and the structural parameters have been shown in Table 4.6 and Table 4.7. It is obvious that our measurements and analysis on structures of $La_{0.67}Ca_{0.33}MnO_3$ are consistent with those data of all other references by neutron diffraction method. The difference between synchrotron XRD by us and neutron diffraction by others is less than

0.5% for lattice parameters, less than 1% for Mn-O bond lengths and around 3% for Mn-O2-Mn bond angles.

Table 4.6 Positional Parameters and Debye-Waller Factors of $La_{1-x}Ca_XMnO_3$ (x~0.33).

	Synchrotron X-Ray Diffraction	Neutron diffraction					
Ca	0.33	0.3	0.3	0.33	0.33	0.34	0.375
T (K)	300	270	300	270	298	275	300
a (Å)	5.4610(4)	5.46558(3)	5.46597(4)	5.4575(1)	5.4569(1)	5.464(2)	5.4730(5)
b (Å)	7.7098(7)	7.72035(4)	7.72603(6)	7.7126(2)	7.7112(1)	7.716(2)	7.7309(9)
c (Å)	5.4750(5)	5.48494(4)	5.48237(5)	5.4728(2)	5.4717(1)	5.473(2)	5.4875(1)
La/Ca							
x	0.0178(5)	0.0185(6)	0.0197(3)	0.0212(3)	0.0187(1)	0.024(1)	0.0209(7)
z	0.997(1)	-0.007(1)	-0.0050(5)	-0.0049(5)	-0.0035(2)	-0.009(2)	-0.0044(7)
B ($Å^2$)	0.43(1)	0.27(5)	0.38(1)	0.68(2)	-0.11(1)	0.9	0.69(1)
Mn							
B ($Å^2$)	0.10(3)	0.24(6)	0.22(2)	0.56(3)	-0.11(1)	0.9	0.69(1)
O(1)							
x	0.480(3)	0.490(1)	0.4913(5)	0.4910(5)	0.4916(8)	0.488(1)	0.4948(4)
z	0.0651(5)	0.0608(9)	0.0637(5)	0.0631(4)	0.0588(14)	0.062(2)	0.0637(1)
B ($Å^2$)	0.6	0.51(7)	0.62(3)	0.82(3)	-0.11(1)	1.3	0.72(4)
O(2)							
x	0.2846(9)	-0.2759(6)	-0.2751(3)	-0.2766(3)	-0.2786(11)	-0.275(2)	-0.2761(2)
y	0.044(1)	-0.0344(4)	-0.0330(2)	-0.0330(2)	-0.0333(3)	-0.032(1)	-0.0315(1)
z	0.7147(4)	0.2761(6)	0.2755(3)	0.2771(3)	0.2781(11)	0.277(2)	0.2762(8)
B ($Å^2$)	0.6	0.54	0.63(2)	0.94(3)	-0.11(1)	1.6	0.89(9)

Table 4.7 Selected Interatomic Bond Distances (Å) and Bond Angles (degree) for $La_{0.67}Ca_{0.33}MnO_3$.

	Synchrotron X-Ray Diffraction	Neutron diffraction		
Ca doping	0.33	0.33	0.33	0.33
T (K)	300	270	300	298
Mn-O(1) ×2	1.9632(7)	1.9601(4)	1.961(3)	1.955(1)
Mn-O(2) ×2	1.9789(6)	1.958(2)	1.958(1)	1.959(6)
O(2)-Mn ×2	1.9839(5)	1.964(2)	1.966(1)	1.963(6)
Mn-O(1)-Mn ×2	158.1(1)	159.4(1)	159.7(1)	160.9(3)
Mn-O(2)-Mn ×4	154.3(1)	160.52(9)	160.75(6)	160.4(14)

Note: Some selected bond distances and bond angles by synchrotron x-ray diffraction are given in the second column. And some neutron results are listed in the third and forth column by Huang *et al.* (1998), the fifth column by Blasco *et al.*

Table 4.6 provides the detailed structure from different research groups: The refined results of the synchrotron X-ray diffraction are given in the second column. Several results of neutron Rietveld analysis from the literature are listed in the right-hand columns for comparison. The third and fourth column results were reported by Hibble *et al.* (1999), the fifth column by Huang *et al.* (1998), the sixth column with an average Debye–Waller factor B = 0.11 (1) A° 2 by Blasco *et al.* (1996), the seventh column by Simopoulos *et al.* (1999) and the last column by Yang *et al.* (2004).

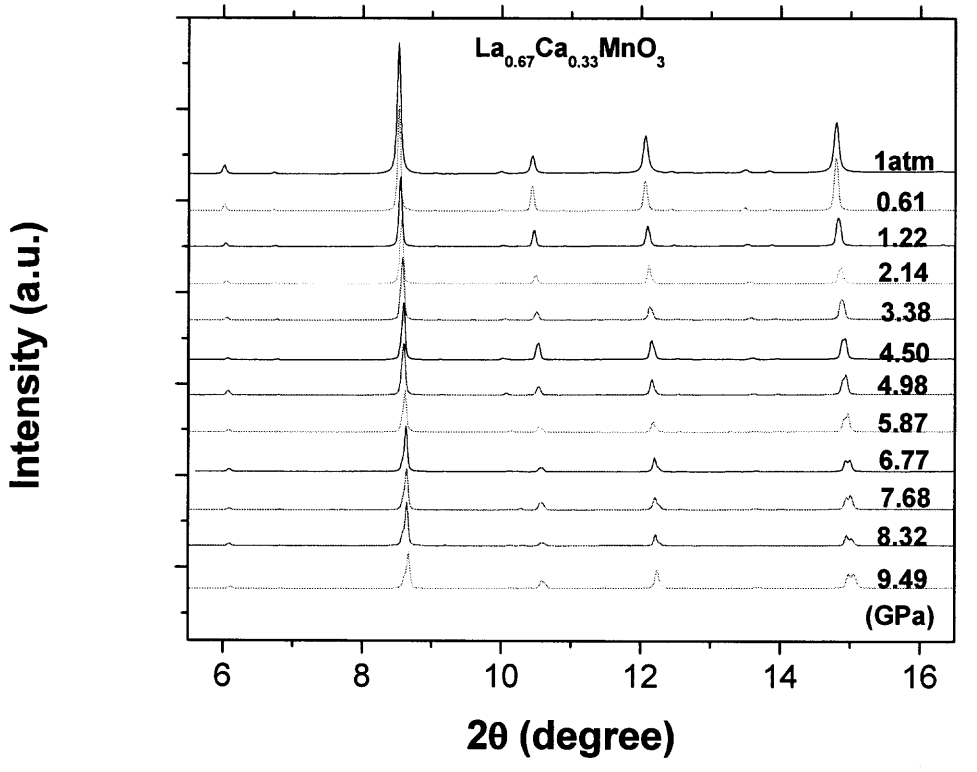

Figure 4.36 Synchrotron x-ray diffraction patterns at various pressures up to ~9.5GPa.

To study the nonlinear pressure effects on this chemically doped CMR manganite, high-pressure synchrotron X-ray diffraction measurements (Figure 4.36) have been conducted under pressures up to ~9.5 GPa at beamline X17c of NSLS. The x-ray wavelength was 0.4066Å corresponding to beam energy of 30 keV. To collect more diffraction rings, off-center CCD measurement was conducted as for the sample $La_{0.75}MnO_3$ shown in Figure 4.20 (a). Then selected wedges were integrated into the diffraction patterns by Fit2D.

Table 4.8 Selected Lattice Parameters and Atomic Coordination of $La_{0.67}Ca_{0.33}MnO_3$ under Pressures: (a) from 1atm to ~4.98GPa, (b) up to ~9.49GPa.

(a)

$La_{0.67}Ca_{0.33}MnO_3$						
Pressure (GPa)	1 atm	1.22	2.14	3.38	4.5	4.98
Space Group	Pnma	Pnma	Pnma	Pnma	Pnma	Pnma
La/Ca						
x	0.018(1)	0.017(1)	0.018(1)	0.021(0)	0.017(1)	0.016(1)
z	0.997(1)	0.997(3)	0.994(3)	1.000(4)	0.994(2)	0.993(1)
Mn						
O(1)						
x	0.480(3)	0.497(1)	0.493(1)	0.505(2)	0.501(2)	0.507(3)
z	0.065(1)	0.065(5)	0.052(1)	0.049(2)	0.052(3)	0.064(2)
O(2)						
x	0.284(1)	0.288(5)	0.267(3)	0.250(2)	0.267(3)	0.255(2)
y	0.044(1)	0.030(1)	0.035(4)	0.042(1)	0.026(2)	0.043(3)
z	0.714(1)	0.715(4)	0.723(5)	0.731(2)	0.714(2)	0.714(1)
$B_{La/Ca}$ (Å^2)	0.43(1)	0.44	0.7	0.38	0.18	0.18
B_{Mn} (Å^2)	0.10(3)	0.51	1.17	0.95	0.37	0.45
B_O (Å^2)	0.6	0.6	0.6	0.6	0.6	0.6
a	5.4610(4)	5.4518(1)	5.4418(2)	5.4348(9)	5.4170(2)	5.4072(10)
b	7.7098(7)	7.6994(3)	7.6945(9)	7.6736(4)	7.6540(5)	7.6403(7)
c	5.4750(4)	5.4686(1)	5.4627(8)	5.4553(6)	5.4442(3)	5.4337(6)
R_p (%)	1.45	2.02	2.38	2.01	1.71	1.91
R_{wp} (%)	2.37	4.23	4.15	4.01	2.97	3.6
χ^2	0.075	0.17	0.207	0.159	0.075	0.139

(b)

Pressure (GPa)	5.87	6.77	7.68	8.32	9.49
Space Group	Pnma	Pnma	Pnma	Pnma	Pnma
La/Ca					
x	0.015(1)	0.017(2)	0.016(1)	0.019(1)	0.016(1)
z	0.998(1)	0.996(1)	0.994(1)	0.994(3)	0.991(1)
Mn					
O(1)					
x	0.495(3)	0.503(1)	0.497(3)	0.503(7)	0.495(5)
z	0.070(1)	0.074(3)	0.073(6)	0.085(2)	0.077(2)
O(2)					
x	0.269(1)	0.252(2)	0.275(1)	0.275(1)	0.282(2)
y	0.041(1)	0.050(3)	0.046(1)	0.047(2)	0.053(1)
z	0.702(6)	0.716(2)	0.695(1)	0.686(4)	0.684(5)
$B_{La/Ca}$ (Å^2)	0.18	0.43	0.43	0.46	0.47
B_{Mn} (Å^2)	0.45	0.24	0.45	0.44	0.45
B_O (Å^2)	0.6	0.6	0.6	0.6	0.6
a	5.4043(0)	5.3933(3)	5.3931(3)	5.3848(26)	5.3760(3)
b	7.6288(1)	7.6245(4)	7.6153(7)	7.6117(25)	7.5918(3)
c	5.4324(1)	5.4298(2)	5.4282(2)	5.4274(23)	5.4193(3)
R_p (%)	2.3	1.97	2.01	3.442	1.97
R_{wp} (%)	4.89	3.16	3.7	5.63	3.59
χ^2	0.208	0.083	0.11	0.241	0.105

Table 4.9 Selected Interatomic Bond Distances (Å) and Bond Angles (degree) of $La_{0.67}Ca_{0.33}MnO_3$ under Pressures: (a) from 1atm to ~4.98GPa, (b) up to ~9.49GPa.

(a)

Pressure (GPa)	1 atm	1.22	2.14	3.38	4.5	4.98
Mn-O(1) ×2	1.963(1)	1.958(5)	1.945(1)	1.937(1)	1.934(2)	1.9415(2)
Mn-O(2) ×2	1.978(6)	1.953(6)	1.916(1)	1.879(18)	1.872(5)	1.835(3)
O(2)-Mn ×2	1.983(1)	1.980(4)	1.993(15)	2.024(17)	2.010(4)	2.066(7)
Mn-O(1)-Mn ×2	158.1(2)	158.9(17)	163.1(3)	164.0(1)	163.3(10)	159.4(9)
Mn-O(2)-Mn ×4	154.4(2)	158.0(14)	161.1(26)	160.7(1)	163.0(2)	158.5(11)

(b)

Pressure (GPa)	5.87	6.77	7.68	8.32	9.49
Mn-O(1) ×2	1.945(1)	1.948(3)	1.945(7)	1.958(3)	1.944(3)
Mn-O(2) ×2	1.832(1)	1.837(2)	1.855(6)	1.830(14)	1.861(6)
O(2)-Mn ×2	2.090(2)	2.076(5)	2.082(5)	2.118(15)	2.112(15)
Mn-O(1)-Mn ×2	157.4(3)	156.0(9)	156.4(20)	152.6(7)	155.1(8)
Mn-O(2)-Mn ×4	155.3(1)	155.8(9)	152.7(1)	150.9(1)	147.7(10)

Then the detailed structure parameters under pressures were obtained by using Rietveld method (Table 4.8 and Table 4.9). In the entire pressure range, $La_{0.67}Ca_{0.33}MnO_3$ maintains orthorhombic symmetry and space group Pnma without a structural phase transition. However, the Mn-O bond distances and Mn-O-Mn bond angles present a nonlinear pressure effect, which has a critical pressure at ~4 GPa corresponding to P* of the pressure effects on resistivity. The tilting angle Mn-O1-Mn only increases ~6° from the ambient to 4 GPa, which is much less than the increasing for the self-doped La_xMnO_3.

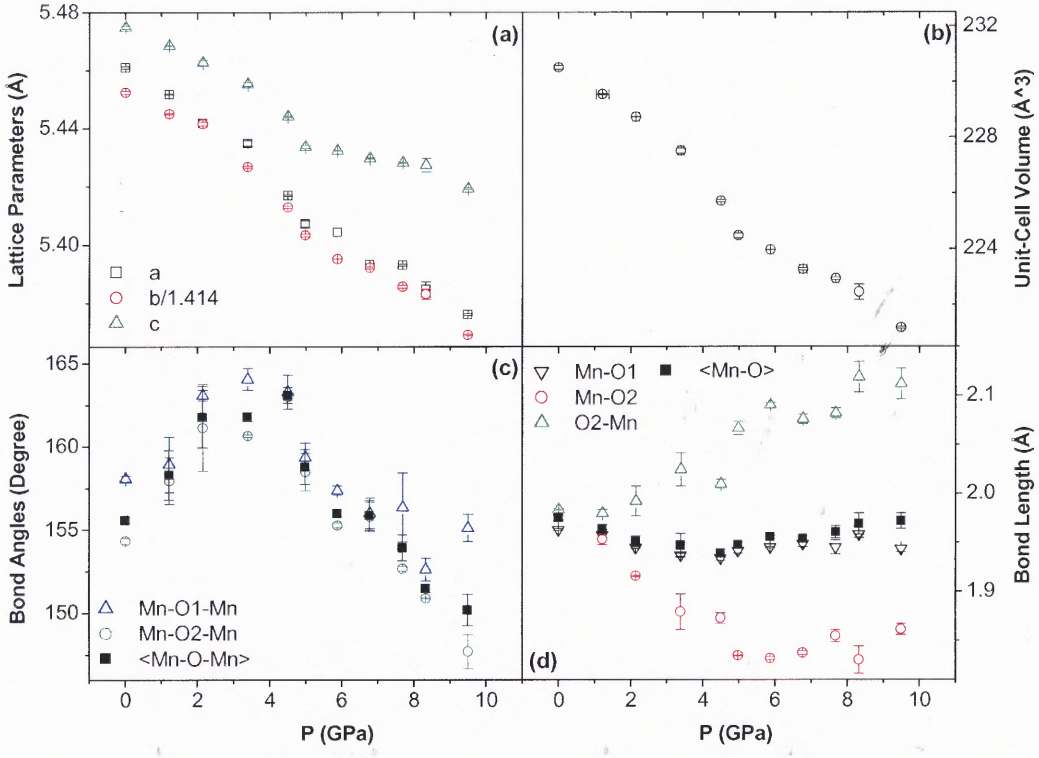

Figure 4.37 Pressure dependence of structural parameters of $La_{0.67}Ca_{0.33}MnO_3$: (a) lattice parameters, (b) unit-cell volume, (c) bond angles, and (d) bond distances.

In Figure 4.37 (a) and (b), the lattice parameters and unit-cell volume approximately have linear pressure effects, but with small kinks around 4GPa. Figure 4.37 (c) shows both in-plane angles (Mn-O1-Mn) and out-of-plane angles (Mn-O2-Mn)

reaching maximum values simultaneously at P*. In Figure 4.37 (d), the splitting of three pairs of bonds (Mn-O1, Mn-O2 and O2-Mn) in MnO_6 octahedral increases with pressures, which means the perovskite structures have been significantly distorted under high pressures.

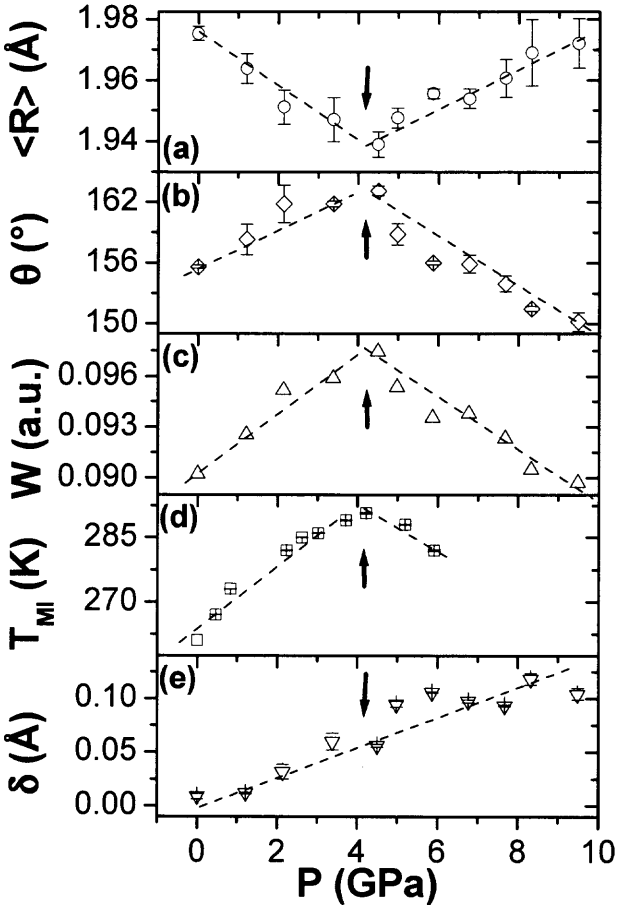

Figure 4.38 Pressure dependence of structural and electronic parameters for $La_{0.67}Ca_{0.33}MnO_3$. The average Mn-O distance (a), average Mn-O-Mn bond angle (b), the electron bandwidth W (c), the metal-insulator transition temperature T_{MI} (d), and the MnO_6 octahedral distortion (e), are plotted as a function of pressure.

To further understand the relationship between electronic properties and atomic structures, all prominent parameters are presented in Figure 4.38. Since 33% of La sites are

occupied by Ca^{2+} cations, there is no vacancy, which induce a much smaller distortion δ~0.009Å than those of La_xMnO_3 (for x=0.85, δ~0.055Å and for x=0.75, δ~0.071Å) at the ambient pressure. In Figure 4.38 (e), the octahedral distortion almost linearly increases to ~0.110Å at 9.5 GPa.

In Figure 4.38 (a) and (b), below P* the distance between the neighboring Mn sites decrease with the compressed Mn-O bond distances; however, above P* the increasing buckling angles become the main factors to reduce the unit-cell volume. By the empirical expression for carrier bandwidth $W \propto \cos(1/2(\pi - < \theta_{Mn-O-Mn} >)) / d_{Mn-O}^{3.5}$, the pressure dependence of W has been plot in Figure 4.38 (c). Similar as the self-doped manganites La_xMnO_3, below P* the increase in T_{MI} with pressure is due to the increase in the electron bandwidth, which reaches its maximum at P*. Further increases in pressure enhance local distortions, which trap the e_g conduction electrons and produce an insulating phase. This can be further seen from the enhancement of the resistivity for pressures above P*.

4.3.3 Magnetization Measurement

For $La_{0.67}Ca_{0.33}MnO_3$, Curie temperature T_C=264.9(4) K coincide with T_{MI} ~ 262.0±1.0 K at ambient pressure, which reveals its phase transition from PM insulator to FM metal during the cooling process. This polycrystalline sample $La_{0.67}Ca_{0.33}MnO_3$ has a high magnetization around 3.6 μ_B/Mn and the resistivity about 15.0 mΩ*cm at T_{MI}, which consist with the values by Huang *et al*[113].

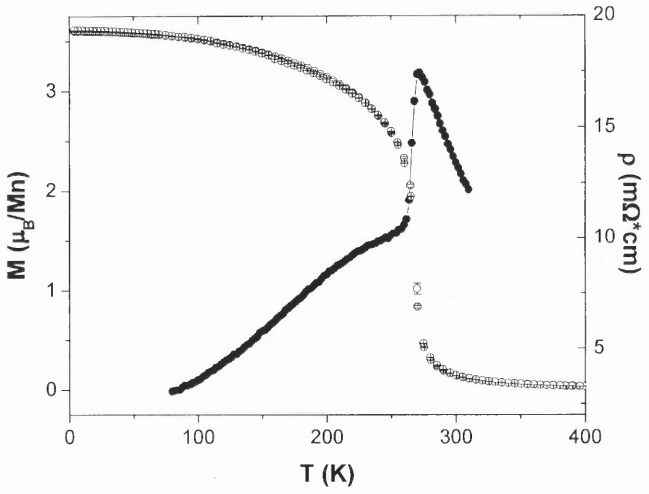

Figure 4.39 Magnetization and resistivity versus temperature at ambient pressure for $La_{0.67}Ca_{0.33}MnO_3$.

4.3.4 Summary

Figure 4.40 shows the pressure dependence of T_{MI} for $La_{0.67}Ca_{0.33}MnO_3$ measured by our group, by Neumeier *at el.*, and by Laukhin *at el.*. Due to different definitions for T_{MI}, the values of T_{MI} have an offset, but at low pressure range all data show very similar pressure effects. By extending these previous high-pressure resistivity measurements up to ~6.0 GPa and synchrotron X-ray diffraction up to ~9.5 GPa, the nonlinear pressure effect has been found with a critical P* ~4.0 GPa.

Depending on structural and electronic transport analysis for this typical CMR manganite $La_{0.67}Ca_{0.33}MnO_3$, the pressure effects we observed are universal – common to the broad class of perovskite manganites and not just to the self-doped system La_xMnO_3.

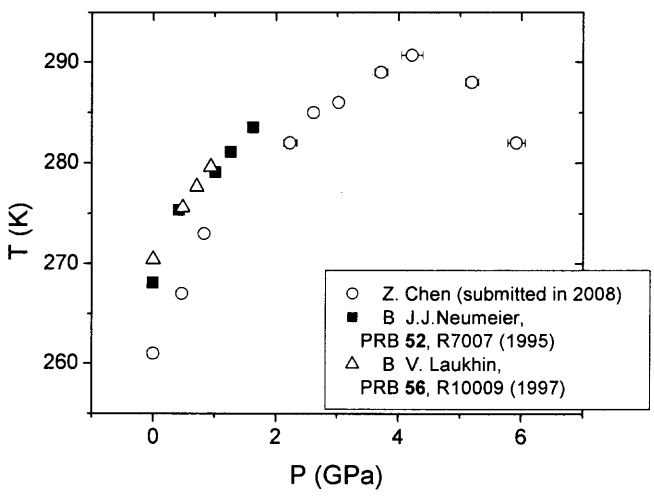

Figure 4.40 Pressure dependence of T_{MI} for $La_{0.67}Ca_{0.33}MnO_3$ measured by different groups.

CHAPTER 5

SUMMARY AND FUTURE WORK

5.1 Summary

In perovskite manganites, understanding the properties requires a detailed knowledge of the spin-charge and lattice coupling. The DE model reveals the qualitative relationship between electron conductivity and external magnetic field at low temperature. However, the spin-lattice coupling responsible for the metal to insulator transition is not contained in this model. Pressure dependent studies are important in this research.

Chemical (chemical pressure) doping and high pressures are two direct methods to modify the crystalline structure for manganites. Chemical doping method alter the atomic structure by selecting different ions of the same valence, which results in the mismatch between $<r_A>$ and Mn-site ion size. This mismatch produces stresses among neighboring atoms, also called "internal pressure", to induce modification of the MnO_6 octahedra or the angles between the polyhedra. Thus chemical doping method affects Mn-O-Mn bond angles without significantly changing Mn-O bond length. However, ion substation creates a system which is not the same as the original under consideration. High pressure offers a way to adjust the bond distance and bond angles in a more controllable way, which can be understood if structural measurements are conducted.

Until recently, most studies for high pressure effects on electron transport and magnetic properties were within a low pressure range (below 2 GPa). In this range, it has been observed that increasing pressures enhance the metallic states for some of CMR

manganites. The metal-insulator transition temperature increases with magnetic fields. This behavior is similar to pressure effects in the low pressure range. The coincidence of T_{MI} and T_C shows these manganites have a transition from ferromagnetic metal to paramagnetic insulator.

However, with the improvement of high pressure techniques, a higher pressure experimental range can be reached and more physical properties under pressures can be characterized. For all of samples (CMR region) studied in this work, obvious pressure effects on electronic transport and structure have been found, especially a critical pressure appears roughly around 4.0 GPa. Below P*, pressures increase the metal-insulator transition temperature and electrical conductivity while both of them decrease with increasing pressure above P*. It appears that pressures enhance the metallic properties of all samples below the critical pressure, whereas it suppresses metallic phase at higher pressures (Figure 5.1). We find the anharmonic interatomic potential plays an important role for this nonlinear pressure effects on electron transport and atomic structure. Below P*, pressure drives the enhancement of carrier bandwidth W (empirically expressed in Equation 2.6) by compressing Mn-O bonds and increasing Mn-O-Mn bond angles. While above P*, the average bond distance can not be changed significantly due to hard core potential. At high pressures, Jahn-Teller distortions suppress the electron mobility. This results in preference of an insulating state.

In figure 5.1, the pressure dependence of T_{MI} of all samples studied in this work has been plotted. The most significant feature is that the critical pressure P* exist in a small pressure range from ~3.4 to ~4.2 GPa for all of specimens.

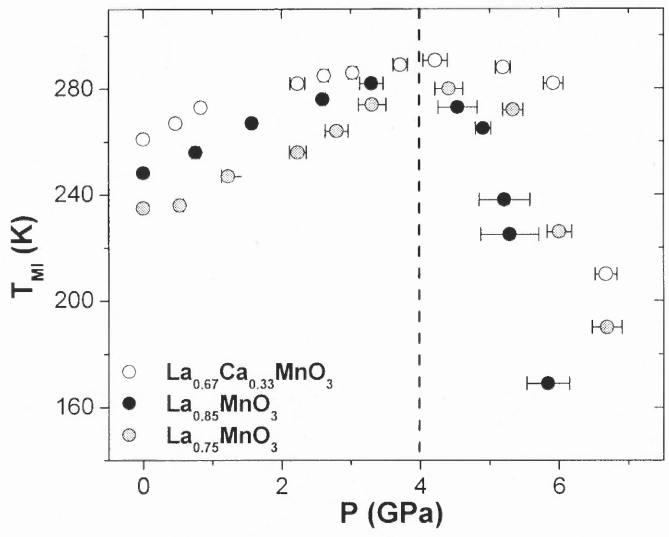

Figure 5.1 Pressure dependence of metal-insulator transition of La_xMnO_3 (x=0.85 and 0.75) and $La_{0.67}Ca_{0.33}MnO_3$.

5.2 Future Work

While below P* the metal insulator transition and magnetic ordering temperature coincide, the behavior at higher pressure is not know. To understand CMR properties under pressure, the interactions among charges, orbital, spins and atomic lattices need to be further studied. Two methods can be conducted in relatively convenient ways: high pressure neutron scattering and high pressure susceptibility measurements.

5.2.1 Neutron Diffraction Measurements

Neutron diffraction is an idea method to measure both lattice structure and magnetic structure simultaneously. Kozlenko[74] *et al.* has studied the crystal and magnetic structure of manganites $La_{0.67}Ca_{0.33}MnO_3$ and $Pr_{0.7}Ca_{0.3}MnO_3$ by powder neutron diffraction under

pressures up to 5 GPa in the temperature range 15-300K and observed an A-type AFM structure at P=3.8GPa and T=16K. By this method, it is reasonable to measure the pressure dependence of Curie temperature T_C. We have started these types of experiments by using the ISIS neutron source. Even though a large amount of samples required limiting the pressure range, the neutron scattering method enables better measurements of oxygen positions than x-rays. For x-ray diffraction method, there is a crucial problem that the scattering cross section of oxygen atom is too small compared with those heavy cations such as La and Mn.

5.2.2 High Pressure Magnetization

As typical CMR manganites, the magnetic properties, such as magnetization and magnetic susceptibility, should be investigated. By using micro-cells in MPMS system, low pressure range magnetization up to ~2GPa can be measured. But it still can not pass through the critical pressure P*~4GPa for our samples.

As another high-pressure magnetic method, susceptibility measurements are becoming more and more popular and convenient by using designer diamond anvil cells, in which micro coils and circuits are covered by artificial diamond layers. The magnetization and curie temperatures can be more directly acquired under pressures.

5.2.3 High Pressure Local Structure Measurements

High-pressure x-ray absorption spectroscopy can be used to observe the local structure of MnO_6 perovskite octahedral. Due to high x-ray absorption of diamond for low energy, the perforated diamond has been utilized. However, this design of diamond anvil is easy to

break even under low pressure. We have done some low pressure XAFS and are still seeking new designs of DAC for higher pressures. We have established collaboration with W. Bassett (Cornell University) and have carried out some high-pressure experiments. New experiments are planned.

5.2.4 Other Possible Measurements

For pressure effects on the Jahn-Teller distortions and vibrations in the octahedral, high pressure Raman scattering and IR measurements can be used. Our group is conducting high-pressure IR experiments for some manganites and thin film sample $La_{0.8}MnO_3/LaAlO_3$. However, most electronic and magnetic applications of CMR materials are focused on thin film. So the study of uniaxial pressure effects for film and single crystal sample becomes necessary and is attracting more attention from scientists and engineers in this area.

We have conducted some high-pressure experiments for our samples, but to understand basic physics of high pressure effects, and will conduct more work in the future. Table 5.1 shows a list of experiments completed and to be performed.

Besides high-pressure experiments, the theoretical studies for high pressure effects on electronic, magnetic and crystalline structure are important. The calculation of bandwidth and density of state under pressures can be utilized to describe the correlation between charge, spin, orbital and lattice structure in CMR perovskite manganites.

In summary, high pressure effects on electron transport and atomic structure have been studied in this work. The discussions and results may reveal the origin of nonlinear pressure effects up to ~7GPa. While at the low pressure range, pressure induces similar

effects on electronic and magnetic properties as chemical doping and external magnetic field; at high pressures these manganites show large Jahn-Teller distortions, which suppress T_{MI}. With the development of high-pressure techniques and instruments, more and more measurements can be performed in future. The deeper and broader research of pressure effects will lead to more detailed models of correlated electron systems such as perovskite manganites and applications of other complex oxides.

Table 5.1 List of Experiments Completed and to be Performed.

		LMO90				
	Future work	Measuring	Data processing	done	Lab	comments
Element Analysis				X	QTI	La/Mn=0.852
M vs. T				X	Rutg	50Oe - 4.5T
MR				X	Rutg	0 - 7.5T
R_HP				X	NJIT	0-5.8G
XRD_HP				X	BNL	0-10.6G
XAFS_HP		X			BNL	0,1.5G
Neutron_HP		X				
Magnetization_HP	X					
		LMO80				
	Future work	Measuring	Data processing	done	Lab	comments
Element Analysis				X	QTI	La/Mn=0.75
M vs. T				X	Rutg	
MR				X	Rutg	0 - 7.5T
R_HP				X	NJIT	0 - 6G
XRD_HP				X	BNL	0 - 9.6GPa
XAFS_HP		X			BNL	
Neutron_HP		X				
Magnetization_HP	X					
		LCMO33				
	Future work	Measuring	Data processing	done	Lab	comments
M vs. T				X	Rutg	
MR				X	Rutg	
R_HP				X	NJIT	0-6GPa
XRD_HP				X	BNL	0-9.6GPa
XAFS_HP		X			BNL	
Neutron_HP		X				
Magnetization_HP	X					

REFERENCES

1. M. N. Baibich, J. M. Broto, and A. Fert *et al.*, Physical Review Letters **61**, 2472 (1988).
2. G. Binasch, P. Gruberg, and F. Saurenbach *et al.*, Physical Review B **39**, 4828 (1989).
3. G. H. Jonker and J. H. Van Santen, Physica **16**, 337 (1950).
4. S. Jin, T. H. Tiefel, and M. McCormack *et al.*, Science **264**, 413 (1994).
5. Y. Nagai, Magnetic Random Access Memory, Patent number: 6445613 (2002).
6. S. Z. Janice Nickel, Colossal Magnetoresistance Sensor, Patent number: 5835003 (1997).
7. M. T. M. Sungho Jin, Apurba Roy, James C. Wadlington, Magnetoresistivity Current Sensor Having High Sensitivity, Patent number: 5461308 (1995).
8. D. D. Awschalom and M. E. Flatte, Nature Physics **3**, 153 (2007).
9. J. M. Daughton, Journal of Magnetism and Magnetic Materials **192**, 334 (1999).
10. M. A. Ruderman and C. Kittel, Physical Review **96**, 99 (1954).
11. K. Yosida, Physical Review **106**, 893 (1957).
12. T. Kasuya, Progress Theory Physics **16**, 45 (1956).
13. J. H. Van Vleck, Reviews of Modern Physics **34**, 681 (1962).
14. D. Wang, M. Tondra, and J. M. Daughton *et al.*, Journal of Applied Physics **85**, 5255 (1999).
15. J. R. Childress and C. L. Chien, Physical Review B **43**, 8089 (1991).
16. J. Q. Xiao, J. S. Jiang, and C. L. Chien, Physical Review Letters **68**, 3749 (1992).
17. A. D. Gavrin, J.Q. Xiao, C.L. Chien, and R.J. Celotta, Applied Physics Letters **66**, 1683 (1995).
18. M. B. Salamon and M. Jaime, Reviews of Modern Physics **73**, 583 (2001).
19. V. Goldschmidt, Geochemistry, Oxford University Press (1958).

20. J. Rodriguez-Carvajal, M. Hennion, and F. Moussa *et al.*, Physical Review B - Condensed Matter and Materials Physics **57** (1998).

21. J. B. Goodenough, Reports on Progress in Physics **67**, 1915 (2004).

22. I. Loa, P. Adler, and A. Grzechnik, *et al.*, Physical Review Letters **87**, 125501 (2001).

23. H. Y. Hwang, S. W. Cheong, and P. G. Radaelli, *et al.*, Physical Review Letters **75**, 914 (1995).

24. R. D. Shannon and C. T. Prewitt, Acta crystallography. A **32**, 785 (1976).

25. C. Zener, Physical Review **82**, 403 (1951).

26. J. H. van Santen and G. H. Jonker, Physica **16**, 599 (1950).

27. S. Satpathy, S. P. Zoran, and R. V. Filip, Journal of Applied Physics **79**, 4555 (1996).

28. S. Satpathy, Z. S. Popović, and F. R. Vukajlović, Physical Review Letters **76**, 960 (1996).

29. P. W. Anderson and H. Hasegawa, Physical Review **100**, 675 (1955).

30. A. J. Millis, P. B. Littlewood, and B. I. Shraiman, Physical Review Letters **74**, 5144 (1995).

31. J. B. Goodenough, Physical Review **100**, 564 (1955).

32. P. G. de Gennes, Physical Review **118**, 141 (1960).

33. M. B. Salamon and M. Jaime, Reviews of Modern Physics **73**, 583 (2001).

34. C. H. Chen and S. W. Cheong, Physical Review Letters **76**, 4042 (1996).

35. J. Fontcuberta, V. Laukhin, and X. Obradors, Physical Review B **60**, 6266 (1999).

36. M. Roy, J. F. Mitchell, and A. P. Ramirez *et al.*, Journal of Physics-Condensed Matter **11**, 4843 (1999).

37. G. Xiao, E. J. McNiff, and G. Q. Gong *et al.*, Physical Review B **54**, 6073 (1996).

38. Y. Tokura and Y. Tomioka, Journal of Magnetism and Magnetic Materials **200**, 1 (1999).

39. Y. Murakami, J. P. Hill, and D. Gibbs *et al.*, Physical Review Letters **81**, 582 (1998).

40. T. Hotta, S. Yunoki, and M. Mayr *et al.*, Physical Review B **60**, 15009 (1999).

41. T. Hotta, A. L. Malvezzi, and E. Dagotto, Physical Review B **62**, 9432 (2000).

42. H. A. Jahn and E. Teller, Physical Review **49**, 874 (1936).

43. Y. Moritomo, A. Asamitsu, and Y. Tokura, Physical Review B **56**, 12190 (1997).

44. D. P. Kozlenko, L. S. Dubrovinsky, and I. N. Goncharenko *et al.*, Physical Review B **75** (2007).

45. C. Meneghini, D. Levy, and S. Mobilio *et al.*, Physical Review B **65**, 012111 (2001).

46. M. Medarde, J. Mesot, and P. Lacorre *et al.*, Physical Review B **52**, 9248 (1995).

47. W. A. Harrison, The Electronic Structure and Properties of Solids (Freeman, San Francisco), Chap. 19, p. 430 (1980).

48. J. J. Neumeier, M. F. Hundley, and J. D. Thompson *et al.*, Physical Review B **52**, R7006 (1995).

49. V. Laukhin, J. Fontcuberta, and J. L. Garcia-Munoz *et al.*, Physical Review B **56**, R10009 (1997).

50. C. Cui, T. A. Tyson, and Z. Chen *et al.*, Physical Review B **68**, 214417 (2003).

51. C. Cui, T. A. Tyson, and Z. Zhong *et al.*, Physical Review B **67**, 104107 (2003).

52. A. M. Haghiri-Gosnet and J. P. Renard, Journal of Physics D: Applied Physics **36** (2003).

53. C. Cui and T. A. Tyson, Physical Review B **70**, 094409 (2004).

54. H. Y. Hwang, T. T. M. Palstra, and S. W. Cheong *et al.*, Physical Review B **52**, 15046 (1995).

55. E. Dagotto, T. Hotta, and A. Moreo, Physics Reports-Review Section of Physics Letters **344**, 1 (2001).

56. D. M. Adams, S. J. Payne, and K. M. Martin, Applied Spectroscopy **27**, 377 (1973).

57. R. H. Wentorf Jr, Modern Very High Pressure Technique (1962).

58. E. F. Skelton, C.-y. Liu, and I. L. Spain, High Temperatures - High Pressures **9**, 19 (1977).

59. E. A. Perez-Albuerne, and H. G. Drickamer, Review Science Instrument **35**, 29 (1964).

60. D. W. Pipkorn, P. Debrunner, G. Depasquali, H. G. Drickamer, and H. Faruenfelder, Physical Review **135**, A1604 (1964).

61. H. G. Drickamer, Review Science Instrument **32**, 212 (1961).

62. C. H. Whitfield, E. M. Brody, and W. A. Bassett, Review of Scientific Instruments **47**, 942 (1976).

63. D. M. Adams, S. K. Sharma, and R. Appleby, Applied Optics **16**, 2572 (1977).

64. C. Patel, T. J. Parker, and H. Jamshidi *et al.*, Physica Status Solidi (B) Basic Research **122**, 461 (1984).

65. H. N. Cheng and G. H. Lee, Journal of Polymer Science, Part B: Polymer Physics **25**, 2355 (1987).

66. Y. K. Vohra, S. J. Duclos, and A. L. Ruoff, Physical Review B **36**, 9790 (1987).

67. I. Loa, P. Adler, A. and Grzechnik *et al.*, Physical Review Letters **87**, 125501 (2001).

68. A. M. Dziewonski, Physical Earth Planetary Interior **25**, 297 (1981).

69. D. J. Dunstan and I. L. Spain, Journal of Physics E: Scientific Instruments **22**, 913 (1989).

70. I. L. Spain and D. J. Dunstan, Journal of Physics E: Scientific Instruments **22**, 923 (1989).

71. R. Miletich, and W. F. Kuhs, Rev. Mineral. Geochem **41**, 445 (2000).

72. A. Ronald Miletich, Werner F. Kuhs, Reviews in Mineralogy and Geochemistry **41**, 445 (2000).

73. E. Colombier and D. Braithwaite, Review of Scientific Instruments **78** (2007).

74. D. P. Kozlenko, V. P. Glazkov, and R. A. Sadykov *et al.*, Journal of Magnetism and Magnetic Materials **258**, 290 (2003).

75. H. E. Lorenzana, M. Bennahmias, and H. Radousky *et al.*, Review of Scientific Instruments **65**, 3540 (1994).

76. G. J. Piermarina, S. Block, and J. D. Barnett, Journal of Applied Physics **44**, 5377 (1973).

77. V. A. Sidorov and O. B. Tsiok, Fizika i Tekhnika Vysokikh Davlenii **34**, 74 (1991).

78. Fujishiro, G. J. Piermarini, and S. Block *et al.*, High pressure in research and Industry, Proc 8th AIRAPT Conference, 608 (1981).

79. H. K. Mao and P. M. Bell, Science **103**, 1004 (1979).

80. P. M. Bell and H. K. Mao, Carnegie Institute of Washington Yearbook **80**, 404 (1981).

81. D. H. Liebenberg, Physics Letters A **73**, 74 (1979).

82. K. Asaumi and A. L. Ruoff, Physics Review B **33**, 5633 (1986).

83. R. Le Sar, S. A. Ekberg, and L. H. Jones *et al.*, Solid State Communications **32**, 131 (1979).

84. J. A. Xu, H. K. Mao, and P. M. Bell, Science **232**, 1404 (1986).

85. Richard, Journal of Applied Physics **37**, 4973 (1966).

86. A. Lacam and C. Chateau, Journal of Applied Physics **66**, 366 (1989).

87. A. Lacam, High Pressure Research **5** (1990).

88. P. Comodi and P. F. Zanazzi, Journal of Applied Crystallography **26**, 843 (1993).

89. V. V. Shchennikov, S. V. Ovsyannikov, and A. Y. Derevskov, Journal of Physics and Chemistry of Solids **67**, 2203 (2006).

90. P. Kozlenko, S. V. Ovsyannikov, and V. V. Shchennikov *et al.*, Physics of the Solid State **48**, 1741 (2006).

91. M. D. Furnish and W. A. Bassett, Journal of Geophysics Research **88**, 10333 (1983).

92. L. C. Ming, M. H. Manghnani, and J. Balogh, High-Presure Research in Mineral Physics, 69 (1987).

93. L. G. Liu and W. A. Basset, Journal of Geophysics Research **80**, 3777 (1975).

94. H. K. Mao, P. M. Bell, and C. Hadidiacos, High-Pressure Research in Mineral Physics, 138 (1987).

95. H. K. Mao, G. Shen, and R. J. Hemley *et al.*, Properties of Earth and Planetary Materials at High Pressure and Temperature, 27 (1998).

96. G. Fiquet, D. Andrault, and A. Dewaele *et al.*, Phys. Earth Planetary Interior **105**, 21 (1998).

97. R. Kleb and J. R. D. Copley, Review of Scientific Instruments **46**, 1190 (1975).

98. J. Paureau and C. Bettier, Review of Scientific Instruments **46**, 1484 (1975).

99. Y. Uwatoko, T. Fujiwara, and M. Hedo *et al.*, Journal of Physics-Condensed Matter **17**, S1011 (2005).

100. P. L. Alireza and S. R. Julian, Review of Scientific Instruments **74**, 4728 (2003).

101. http://www.eurekalert.org/features/doe/2004-12/ddoe-pts122204.php.

102. http://www.llnl.gov/str/December04/Weir.html.

103. S. Matsuzaki, Review of Scientific Instruments **65**, 221 (1994).

104. J. M. D. Coey, M. Viret, and S. von Molnar, Advances in Physics **48**, 167 (1999).

105. D. P. Kozlenko and B. N. Savenko, Physics of Particles and Nuclei **37**, S1 (2006).

106. Y. Moritomo, H. Kuwahara, and Y. Tomioka *et al.*, Physical Review B **55**, 7549 (1997).

107. V. Laukhin, B. Martínez, and J. Fontcuberta *et al.*, Physical Review B **63**, 214417 (2001).

108. A. Maignan, C. Michel, and M. Hervieu *et al.*, Solid State Communications **101**, 277 (1997).

109. F. Rivadulla, M. Otero-Leal, and A. Espinosa *et al.*, Physical Review Letters **96,** (2006).

110. M. Mayr, A. Moreo, and J. A. Vergé *et al.*, Physical Review Letters **86**, 135 (2001).

111. B. K. M. Uehara, and S.-W. Cheong (personal communication).

112. P. Schiffer, A. P. Ramirez, and W. Bao *et al.*, Physical Review Letters **75**, 3336 (1995).

113. Q. Huang, A. Santoro, and J. W. Lynn *et al.*, Physical Review B **58**, 2684 (1998).